Development of cyclotron-produced cobalt-55/58m for theranostic radiopharmaceutical applications

By
Wilson Lin

A dissertation submitted in partial fulfillment of
the requirements for the degree of

Doctor of Philosophy
(Medical Physics)

at the
UNIVERSITY OF WISCONSIN-MADISON
2024

Date of final oral examination: 08/05/2024

The dissertation is approved by the following members of the Final Oral Committee:

Jonathan W. Engle, Associate Professor, Medical Physics and Radiology

Paul A. Ellison, Assistant Professor, Medical Physics

Reinier Hernandez, Assistant Professor, Medical Physics and Radiology

Ali Pirasteh, Assistant Professor, Radiology and Medical Physics

Katherine Gagnon, Global Research Alliance Manager, GEMS PET Systems AB, GE HealthCare

Development of cyclotron-produced cobalt-55/58m for theranostic radiopharmaceutical applications

Wilson Lin

Under the supervision of Dr. Jonathan W. Engle

At the University of Wisconsin-Madison

Abstract

Recent FDA approvals for treating metastatic disease with radiopharmaceutical therapy (RPT) have spurred considerable interest to evaluate the therapeutic potential of novel radionuclides. Radionuclides emitting low-energy electrons (LEE) are promising for treating micro-metastatic disease due to their potential to reduce off-target toxicity at the cellular level. In this paradigm, ^{58m}Co is one of the most favorable candidates because of its low photon-to-electron ratio, optimal emission spectra, accessibility and theranostic matching with the positron-emitting ^{55}Co.

This dissertation aims to improve iron target separation for cyclotron produced $^{55/58m}$Co, elucidate cobalt radiochemistry with clinically relevant chelators and explore theranostic ^{55}Co/^{58m}Co RPT applications. Results demonstrate that cation exchange/extraction chromatography can achieve better radiochemical purity and reduce processing time compared to previously published methods using anion exchange-extraction chromatography. The separated no carrier added (n.c.a.) ^{55}Co could be radiolabeled to Sar derivatives and resulting complexes were suitable for *in vivo* applications with retained tumor-targeting properties, though complex formation was slower than with other clinically relevant chelators. Also, upon complexation with NO2A, NOTA and DO3A, Co and n.c.a. ^{55}Co exhibited redox activity which contrasts with previously published work using ^{55}Co. Cobalt-55 served as a convenient diagnostic congener for ^{58m}Co, and ^{58m}Co was able to demonstrate the desired characteristics of LEE RPT *in vitro* but likely requires probes with higher tumor uptake and less tendency for receptor saturation to induce therapeutically meaningful responses *in vivo*. Nevertheless, the outlook for theranostic ^{55}Co/^{58m}Co RPT remains exciting and further research is warranted.

Acknowledgements

None of the work presented in this thesis would have been possible without the support of friends, family, mentors, and collaborators.

First and foremost, I thank my family for their unwavering support and care. I am extremely fortunate to receive such unconditional love in my life. I thank my friends from Vancouver for their support and amiable nature. I thank my partner for always staying optimistic and supporting me and finding a scholarship for me. I thank my friends from Medical Physics for their support during my degree. For example, I thank Karsten for buying me cashews and pants when I most needed them, I thank Jocelyn for lending me a steamer and ironing board before my defense, I thank Ohyun for enlightening me to the world of steaming eye masks, and I thank Christian for always driving me around. I thank Darek, Abhijit, Zhouran, Morgan, Jennifer, and Owen for their hospitality during my stay at the chemistry building. Likewise, I thank Hailey, Jen, Volkan, Brian, JP, Jennifer, Shelby, and Shefali for showing me UAB and hosting a great HIPPO experience. I thank John, Adam, Anthony, Gunnar, Robert, and August for their help during the cross-section experiments at ND. I also would like to thank Chris, Aeli, Kaelyn, Kendall, and Molly in the UW-Madison Cyclotron Research Group for helping me and for being a great cohort to work with all these years. I am especially indebted to the SAIRF staff (Justin Jeffery, Ashley Weichmann and Dr. Zachary Rosenkrans) for their assistance with animal experiments which ended up being the cornerstone of many of my projects. I would also like to thank U.S. NIH, U.S. DOE, and NSERC for supporting me during my degree.

I thank Dr. Suzanne Lapi for the great collaborative experience and for the exceptional tips on professional development that I still refer to years after our initial discussion. I thank Dr. Eszter Boros for the opportunity to collaborate and perform experiments in her lab, and her time discussing interesting research topics with me. I thank Dr. Zibo Li, Dr. Zhanhong Wu, Dr. German Oscar Fonseca Cabrera, and Xinrui for introducing the sarcophagine construct to me

and for being excellent collaborators. I thank Dr. Graham Peaslee for allowing me to perform cross section experiments with his lab and for helpful discussions during experiments. I thank Dr. Jeanine Batterton for helpful radiochemistry discussions and for providing ^{68}Ga/HPIC support. I thank Dr. Andres Mejia from the Research Animal Resources and Compliance Comparative Pathology laboratory at University of Wisconsin-Madison for interpreting and conducting mouse kidney histology. I thank Dr. Weibo Cai for generously involving me in his lab's exciting and novel research.

I thank the thesis committee for their time and expertise in evaluating my candidacy and for fostering my growth. I thank Dr. Katherine Gagnon for helping me become a better speaker and presenter and for contributing to my professional development. Thank you for always reminding me of professional development opportunities. I thank Dr. Reinier Hernandez for the extended discussions on miscellaneous topics. Thank you for all the helpful comments regarding professional life as well. I thank Dr. Ali Pirasteh for sharing his experiences and clinical expertise, and for creating a memorable defense experience. I immediately applied your wisdom regarding conservatism and withheld jests during a high-stress day for the lab. I thank Dr. Paul Ellison for many helpful suggestions throughout the years. Thank you for always diving deeply into a discussion to ensure the details are correct.

I also would like to give a special mention to each of the UWMCRG staff: I thank Dr. Todd Barnhart for fixing my tie before the defense and for antics that may or may not have resulted in temporary confusion on my end. You will always be the finder and fixer (and maybe prankster!), I may have left some things for you to find in your office… I thank Dr. Eduardo Aluicio-Sarduy for teaching me and helping me get used to the lab work environment and for providing great life advice. You gave me the fundamentals necessary to survive in a wet lab chemistry environment and taught me all the biological assays/techniques that I never would've learned without your encouragement. I thank Dr. Jason Mixdorf for helping with many miscellaneous tasks around the lab and for all the fun . I’m glad that you ultimately joined the lab! Finally, I thank Dr. Jonathan Engle, my advisor, for taking a chance with me even when there was no open position at the time. Your expertise, mentorship and overall cordial attitude serve as an exemplary model that I will attempt to aspire towards. I joked about “professionally developing” during one of our chats, but there truly has been a seismic shift in my professional development due to your willingness to aid me in this area (especially during your sabbatical). Thank you for everything.

Table of Contents

List of Figures

List of Tables

List of Abbreviations

AEF	Absorbed Energy Fraction
AMA	Apparent Molar Activity
BED	Biologically Effective Dose
C.a.	Carrier Added
CAR	Chimeric Antigen Receptors
CT	Computed Tomography
DGA	Diglycolamide
DiAmSar	1,8-Diamino-3,6,10,13,16,19-hexaazabicyclo[6,6,6]-eicosane
DOTA	1,4,7,10-Tetraazacyclododecane-1,4,7,10-tetraacetic acid
DTPA	diethylenetriaminepentaacetic acid
EDTA	Ethylenediaminetetraacetic acid
EOB	End Of Bombardment
EOS	End Of Synthesis
EtOH	Ethanol
FA	Formic Acid
FBS	Fetal Bovine Serum
FDA	U.S. Food and Drug Administration
GA	Sodium gentisate
HEPES	4-(2-Hydroxyethyl)-1-piperazineethanesulfonic Acid
HPGe	High Purity Germanium
HPLC	High-Performance Liquid Chromatography
ICRP	International Commission on Radiological Protection
LC-MS	Liquid Chromatography-Mass Spectrometry
LEE	Low Energy Electrons
LET	Linear Energy Transfer
MeCN	Acetonitrile
MICAP-OES	Microwave Inductively Coupled Atmospheric Plasma Optical Emission Spectrometer
MIP	Maximum Intensity projection
MP-AES	Microwave-Plasma Atomic Emission Spectrometer
MRI	Magnetic Resonance Imaging
N.c.a.	No carrier added
NHE	Normal Hydrogen Electrode
NMR	Nuclear Magnetic Resonance
NO2A	1,4,7-Triazacyclononane-1,4-bis(acetic acid)-7-(acetamide)
NOTA	1,4,7-Triazacyclononane-1,4,7-triacetic acid
NTS	Neurotensin
NTSR1	Neurotensin Receptor 1
OSEM	Ordered Subset Expectation Maximization
PBS	Phosphate Buffered Saline
PET	Positron Emission Tomography
RBE	Relative Biological Effectiveness
RCSDA	Range from Continuous Slowing Down Approximation

ROI	Region of Interest
RPT	Radiopharmaceutical Therapy
Sar	3,6,10,13,16,19-hexaazabicyclo(6,6,6)icosane
TACN	1,4,7-Triazacyclononane
TENDL	TALYS-based evaluated nuclear data library
TFA	Trifluoroacetic Acid
TLC	Thin Layer Chromatography

Chapter 1. Introduction

Improvements in conventional cancer treatments like external beam radiation therapy, hormonal deprivation, surgery and chemotherapy for cancer therapies have led to better patient outcomes for a wide variety of cancers. Additionally, treatments utilizing T-cells genetically modified to express anti-CD19 chimeric antigen receptors (CAR) for refractory B-cell lymphoma have recently led to increased remission and likely curative effects [1,2]. Immune checkpoint inhibitor therapies have also improved clinical outcomes in combination with other treatment modalities such as chemotherapy and antibody drug conjugates, CAR T-Cell therapy, cancer vaccines and radiation therapy [3–7]. Of these, radiation therapy remains a favorable option for treating cancer due to its high efficacy (>40% cure rate) with relatively low induced toxicities and ease of coupling to other treatment modalities [8]. Improved knowledge in cancer biology [9,10] and technological developments have been instrumental in expanding the range of radiation doses without deleterious side effects (known as “therapeutic window”) [11–13].

Current state-of-the-art external beam radiation therapy modalities can include intensity-modulation with image guidance to dynamically match dose gradients to tumor dimensions. Intensity-modulation is typically achieved by physically shaping individual beamlets at each angle then combining multiple beam profiles (~10-100’s) at different angles to result in the desired three-dimensional shape [11,13]. Most external beam radiation therapies utilize photon beams from megavolt electron accelerators, but the relatively high penetration depth places a physical limit on the therapeutic window. Alternatively, heavy ions such as protons and alpha particles deposit most of their energy near the end of their trajectory, known as the Bragg peak, resulting in a characteristic range that is determined by the particle's initial energy and the material it is traversing through [14]. Energy degraders are often used to match the range of the particles to the depth and size of the tumor. However, even with heavy ion beams, the shortest distal dose fall-off is still on the order of millimeters even without considering uncertainties in the range and instrumentation [15,16]. This limits the radiation dose delivered to tumors since surrounding healthy tissues need to be spared, resulting in decreased therapeutic efficacy. Furthermore, residual tumors may also develop radiation resistance throughout the treatment process [17], though this may be less relevant for heavy ion beams.

Another form of radiation therapy often used in the clinic is brachytherapy, where encapsulated radiation sources are physically positioned within the body to deliver localized radiation to tumors [18]. Brachytherapy can attain a smaller distal dose fall-off range compared to external beam radiation therapy, but the technique is invasive and limited by constraints of the human body. Despite this, both techniques have been used to greatly improve the patient's quality of life and have resulted in numerous cases of cancer remission, especially when coupled with other treatment modalities [13,19,20]. Notably, the cancer treated with these modalities are often solid tumors that are well-localized in observable areas.

Metastatic lesions, either originating from single cell/cell clusters spread by primary solid tumors or developed in parallel, are difficult to treat because of their tendency to localize in various different parts of healthy tissues [21,22]. Although most migrating cancer cells are eliminated by stresses during the metastatic cascade, cancer cell clusters demonstrate improved efficiency in establishing metastatic lesions compared to single cells [21–23]. Thus, several drugs targeting circulating tumor cell clusters aim to reduce the metastatic capacity by reducing the cluster size, growth rate or by dissolving clusters into single cells [24]. Most treatment modalities for metastatic cancer remain palliative in nature and are not curative, where metastasis accounts for the majority of all cancer related deaths [22,25,26]. Table 1-1 shows the five-year survival rates for different cancers and stage at the time of diagnosis, where all cancers diagnosed at later stages have worse prognosis.

Table 1-1 Five-year survival rates at the time of diagnosis for different cancers depending on the cancer stage in the United States (based on cancer diagnosed in 2011 and followed until December 31, 2017. Data taken from [27]). The five-year survival rate refers to the percentage of patients that remain alive after five years.

	Female breast	Lung	Prostate	Colorectal
Localized (stage 0&1)	**98%**	**57%**	**100%**	**88%**
Regional (stage 2&3)	**85%**	**31%**	**99%**	**71%**
Distant (stage 4)	**30%**	**7%**	**32%**	**16%**

Recently, several radiopharmaceutical therapy (RPT) agents have either gained U.S. FDA approval for treating metastatic cancer [28,29] or are currently undergoing clinical trials [30,31]. Radiopharmaceutical development (and administration) is similar to non-radioactive pharmaceuticals except with additional considerations for logistics related to sample decay and radiation safety (see Figure 1-1 for the main components involved in a RPT agent). In contrast to chemotherapy, RPT agents are typically administered in the ~10^2 nmol range [29] with diagnostic agents using <10 nmol, whereas non-radioactive pharmaceuticals require ~10-100's μmol [32]. The low amount of tracer used for radiopharmaceuticals is mainly because nuclear decay processes are orders of magnitude more energetic than chemical reactions (typically resulting in higher cytotoxicity per atom) and gamma rays can be detected with higher sensitivity than conventional contrast enhanced imaging agents used in Magnetic Resonance Imaging (MRI) or Computed Tomography (CT) [33]. Maintaining sufficiently low tracer also avoids the risk of deleterious immune response to macroscopic quantities of the tracer, where side-effects from RPT are generally due to radiation induced toxicity.

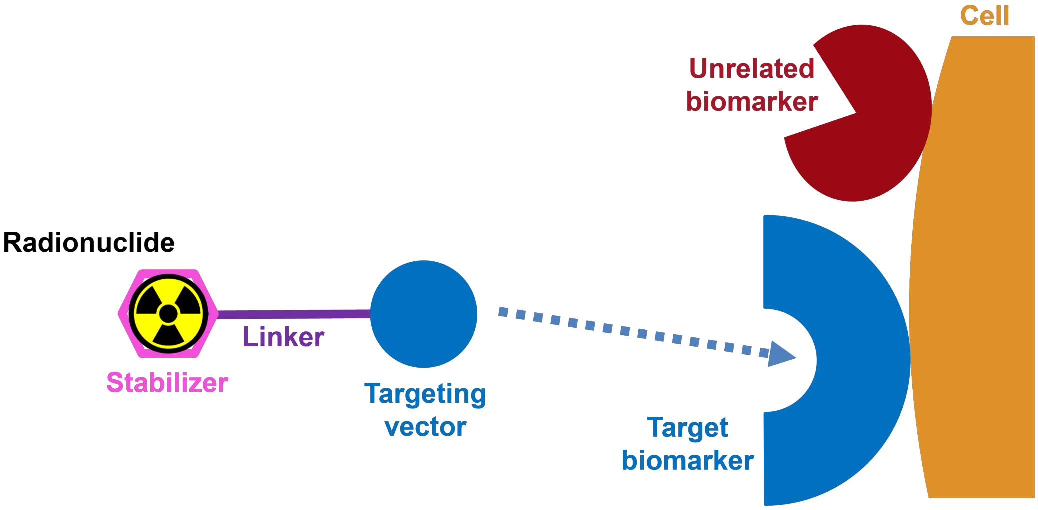

Figure 1-1 Cartoon illustration of the major components involved in RPT. Cells generally express protein receptors involved in cellular signaling processes that can be used as targets for RPT. Targeting vectors used in RPT are often specific to a particular protein receptor and are coupled with a radionuclide via a linker, which could be as small as a single chemical bond, and sometimes a stabilizing molecule to reduce radionuclide dissociation. High binding affinities of the ligand-receptor complex enable targeting vectors to preferentially bind receptors at low concentration. Once bound, the ligand-receptor complex may internalize into the cell for downstream processing and the receptor may be regenerated/recycled.

In comparison with other forms of radiation therapy, RPT is a non-invasive treatment modality that has the potential to seek individual cancer cells in the body. The latter effect is known as ‘targeting’, which is possible due to different biomarkers that are (over)expressed on cancer cells compared to healthy organ tissues. The portion of the radiopharmaceutical that is responsible for seeking these biomarkers is typically referred to as the ‘targeting vector’. RPT may also be used in combination with other treatment modalities such as immunotherapy, chemotherapy, surgery and external beam radiation therapy to improve the overall therapeutic outcome [34,35]. However, RPT agents often accumulate in healthy organs unrelated to the tumor site, such as organs involved in excretion, which adds to undesirable off-target radiation dose that can lead to reduced therapeutic window [36].

One method to lower the off-target radiation dose is to alter the chemical properties of the targeting vector until there is enhanced tumor uptake relative to healthy organs in preclinical models. This is typically quantified by measuring the tumor-to-organ ratio in murine models and then extrapolating to humans. Due to limitations in the availability of radionuclides, targeting vector optimization is often performed using chemically dissimilar radionuclides which can change the biodistribution and pharmacokinetics, leading to inaccurate dosimetry [37]. Fortunately, the radiopharmaceutical agent's chemical identity (i.e., *in vivo* behavior) can be maintained with high fidelity by elementally matching the radionuclides. In such instances, the therapeutic and diagnostic radionuclides are commonly referred to as "theranostic matched-pairs" [38].

On the other hand, another way to reduce the off-target radiation dose is to consider using the same targeting vector but coupled with a radionuclide that emits particles with a shorter range. Recent research has demonstrated enhanced therapeutic windows when using radionuclides that emit particles with shorter range for treating small tumors [39,40]. Particles with different range can also provide synergistic therapeutic effects depending on the size of the tumors [39,41,42]. The emitted particle for RPT is generally charged and its range can be derived from the continuous slowing down approximation (R_{CSDA}), where stopping power is used to determine the rate of kinetic energy loss (n.b., R_{CSDA} is the maximum distance traversed by the charged particle but is nonetheless a good predictor for off-target radiation dose).

Stopping power, or linear stopping power, of a given charged particle at a specified energy refers to the kinetic energy loss per unit distance in a particular material [43]. Thus, R_{CSDA} can be computed by integrating the inverse of stopping power starting from its incident energy until the particle has lost its ability to ionize or excite other particles. Since particles can transfer kinetic energy in the form of collisions with other particles or via bremsstrahlung, stopping power is categorized into collisional and radiative stopping power, respectively. The collisional stopping power can be further classified as electronic, referring to excitations and ionizations of atoms, or nuclear, referring to elastic collisions with the nucleus of the atoms. Inelastic nuclear processes are not generally included due to special considerations for nuclear reactions.

A special variation of electronic stopping power that restricts the kinetic energy of secondary ionized electrons is known as the linear energy transfer (LET). Explicitly, LET refers to the energy imparted to secondary charged particles in the medium *up to a maximum cut-off energy.* For example, if the cut-off energy is set as 10 keV, LET will only include energy transfer events that result in secondary charged particles with ≤10 keV. LET is often used in place of electronic stopping power for radiation dosimetry applications due to its consideration for localized dose transfer [44,45]. For most RPT applications, LET is typically used without specifying the restricted energies and can refer to the unrestricted electronic stopping power [46,47]. Subsequent references to LET in this document will imply unrestricted electronic stopping power to align with nuclear medicine literature. In any case, LET can be considered as the density of ionizations or excitations of atoms in the material along the particle’s track and is dependent on the energy, charge and mass of the particle. Also, LET from α particles are typically orders of magnitude above β particles (see Figure 1-2), due to quantum mechanical and energy conservation principles governing the energy transfer process [48], which leads to enhanced cytotoxic effects at the same radiation dose [47,49–51].

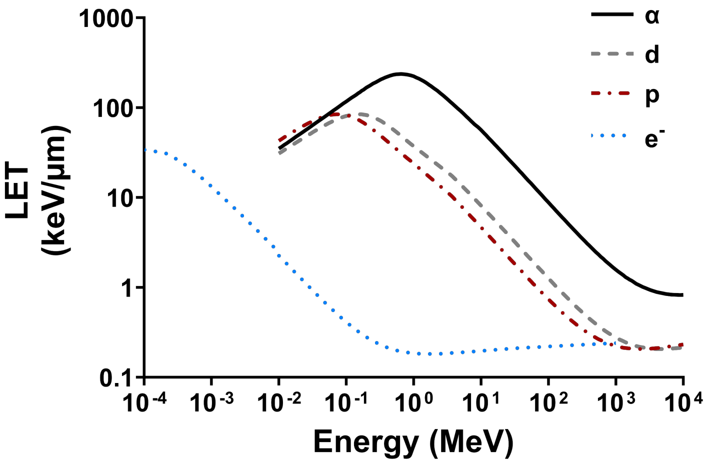

Figure 1-2 Unrestricted electronic collisional stopping power (LET, in the context of nuclear medicine applications) for different particles at different energies in liquid water. The LET for α, d and p were computed from SRIM software [48], and electron LET were taken from [52] and ESTAR program [53]. α-helium nucleus, d-deuteron nucleus, p-proton, e^--electron.

Enhanced biological effects are often described by the relative biological effectiveness (RBE), which refers to the ratio of absorbed doses of two types of radiation (reference and desired) that result in the same biological outcome. However, RBE is dependent on the biological endpoint (e.g., dose to eradicate 37% vs 50% of cells), so RBE calculation methods need to be explicitly stated [54]. RBE determinations have largely been through experimental observations because theoretical calculations require substantial knowledge regarding the biological systems (e.g., DNA repair rate, radiation sensitivity, cell cycle, proliferation rate and/or radionuclide uptake rate) in addition to decay characteristics of the radionuclide(s) [54–57]. Such methods typically model the cell survival according to linear-quadratic exponential models [58] where the linear and quadratic terms are often interpreted as the proportion of “single-hit” lethal events (α) and “multi-hit” sub-lethal events (β), respectively. The α/β ratio has units of dose (Gy), representing the dose at which the proportion of cell-death is equal for “single-hit” and “multi-hit” events, and is different for different tissues and radiation type. Radiation oncologists often exploit this difference to spare tissues with lower α/β compared to cancer cells (see Figure 1-3). Since different dose rates may also lead to different biological outcomes, the total dose for a given fractionation scheme is typically converted into the biologically effective dose (BED). BED assumes each fraction is delivered in an infinitesimal amount, so the total dose from different dosing regimens can be normalized using this reference. In essence, equal BED should result in the same biological outcome. Most applications using BED are related to either external beam radiation therapy and/or brachytherapy, where the dose rates can be calculated and controlled with high precision. Given the large uncertainties and complex models required for RPT dosimetry [54,56], where dosing regimens have simply been prescribed in activity units [28,29], physical dose is often used in preference to BED for RPT applications though this may change with developments in radiobiology and RPT [59]. RPT dosimetry methods at the patient level remain controversial [60].

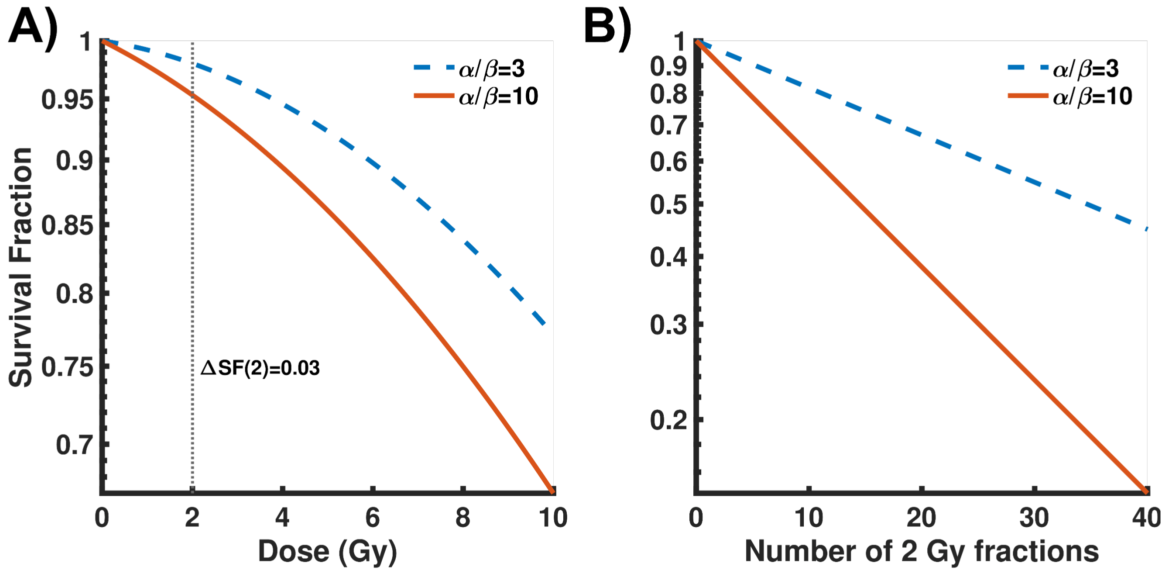

Figure 1-3 A) Example cell survival curves for different α/β values using the standard linear-quadratic model for the survival fraction (SF), where ln(SF) = -(αD+βD^2). α/β=3 Gy and α/β=10 Gy is often assumed for most healthy and cancerous tissues, respectively. β=0.002 Gy^{-2} was constant for both tissues. B) The total dose can be fractionated to compound differences in SF for sparing tissues with lower α/β values. Optimizing fractionation schemes for radiation oncology remains a current area of research.

Although high LET enables α-emitters to eradicate cancer cells at a lower dose and activity as compared with β-emitters, healthy tissues are also non-discriminately damaged, so the therapeutic window may not be significantly better (see Table 1 contained in [61], though differences in pharmacokinetics should be considered). In fact, certain radiosensitive healthy tissues such as bone marrow may be even more susceptible to the enhanced toxicity of α particles when compared with cancer cells [62] which will reduce the therapeutic window. Electrons with low energy (often <25 keV), and subsequently shorter range (R_{CSDA} <20 µm in H_2O), produced from radionuclides undergoing Auger-Meitner [63] and internal conversion processes also have enhanced LET compared to β particles and have been proposed to further enhance the therapeutic window [46,64,65]. Figure 1-4 shows a simplified diagram of the Auger-Meitner effect, where gamma rays compete against internal conversion electrons and x-rays compete against Auger-Meitner electrons. The Auger-Meitner effect could also be induced by electron capture (which results in an electron vacancy).

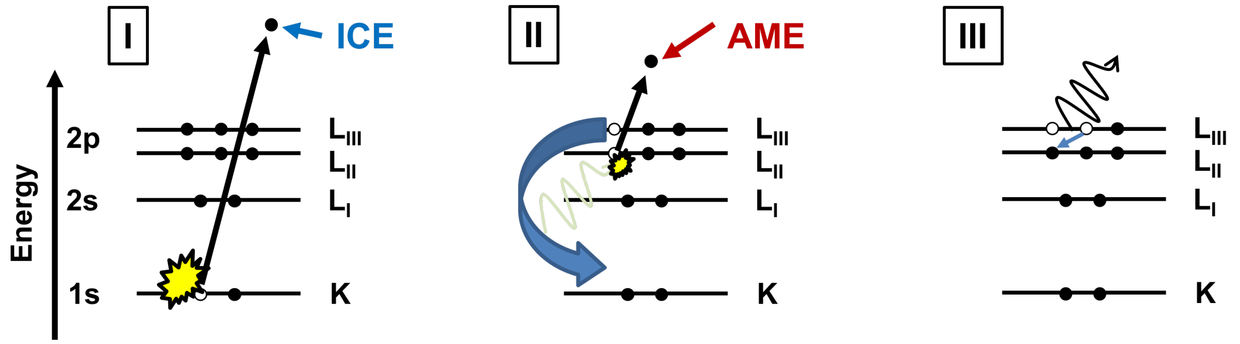

Figure 1-4 A diagram depicting the stages of the Auger-Meitner effect, starting with (I) an electron vacancy in a lower energy level created by the internal conversion process, leading to an internal conversion electron (ICE), or from electron capture. Since internal conversion is a mechanism for the nucleus to relax itself to the ground state, a gamma ray photon can be emitted in lieu of ICE. (II) The vacancy in the lower energy level is populated by an electron with higher potential energy. This difference in energy is either converted into an observable x-ray photon or transferred to an electron. If the imparted energy exceeds the binding energy of the electron, then the electron is ionized and termed an Auger-Meitner electron (AME). (III) The cycle repeats itself until the atom relaxes to its ground state.

Unlike α particles, which can span several cell diameters in range, low energy electrons (LEE) typically do not traverse beyond one cell diameter [61,64]. Thus, LEE-emitters may be more effective than α-emitters for treating micrometastatic disease such as circulating tumor cell clusters (typically <10 cells/cluster [24]). If these radionuclides can be selectively internalized into cancer cells, then the off-target dose can be further reduced due to their short range. Figure 1-5 illustrates the major differences between the three types of radiation considered for RPT, where LEEs are shown to have considerably reduced range compared to β particles and can achieve LET in the same order of magnitude as α particles. Additionally, even if the radiopharmaceutical is accumulated in healthy organs, as in the excretion pathway, this reduction in dose may still apply due to differences in the physiological mechanism of drug uptake for the cell. Interestingly, the cell (plasma) membrane has been hypothesized to be a useful target for radiation induced cytotoxicity from LEEs [42,66,67] but further research is needed to substantiate this effect as it remains somewhat controversial [68]. The cellular internalization process, coupled with increased LET, can also improve the probability that LEE will deliver sufficient dose to sensitive structures of the cell, enhancing cytotoxicity. Unsurprisingly, most successful applications of LEE-emitters for RPT are when the radionuclides are DNA-localized [69–72]. *In vitro* cytotoxicity assays using DNA-localizing targeting vectors coupled with LEE-emitters have shown RBE>45 in comparison to acute radiation from external x-ray sources [70].

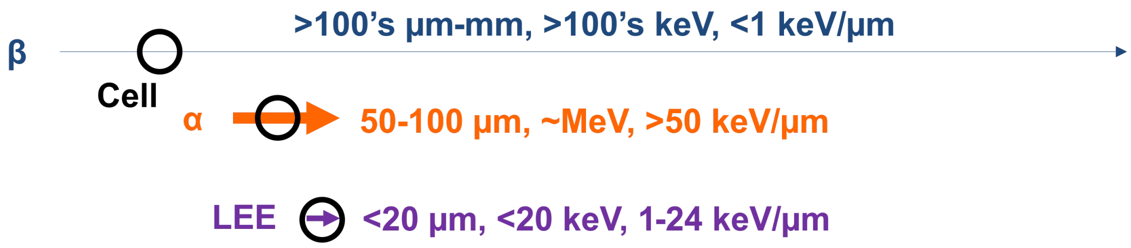

Figure 1-5 The typical range, energy and LET of different types of radiation emitted by radionuclides used in RPT. A black circle roughly matching the diameter of a cell is drawn for reference. β refers to beta particles, α refers to alpha particles and LEE refers to low energy electrons. The listed ranges correspond to R_{CSDA} and are illustrated by the length of each arrow. The LET is illustrated by the thickness of the arrow. Drawings are not to scale but are kept at reasonable proportions to highlight the main differences between each radiation type.

In this paradigm, the therapeutic window from using LEE-emitters may be significantly larger compared to β- and α-emitters. However, the lack of uniform *in vivo* tumor uptake, which is common for pharmaceutic agents in general, can lead to untreated subpopulations of cells [73,74]. Since the main advantage of utilizing LEE-emitting radionuclides is for their short range, crossfire contributions will not meaningfully mitigate tumor heterogeneity effects. Despite this, tumor heterogeneity may not limit the utility of LEEs in RPT as increased multiple-dosing regimen made available from the theoretically better therapeutic window may be enough to target remaining tumor cells. The main challenge for utilizing these low energy electrons is in finding a suitable targeting vector that is capable of both targeting the tumor *in vivo* and be transported near radiosensitive areas (e.g., mitochondria, nucleus, DNA) after associating with the target biomarker.

Furthermore, as depicted in Figure 1-4, the Auger-Meitner effect competes with the production of x-ray photons, which are far more penetrating than electrons. Assuming 5 keV photons are co-produced during decay, ~700 μm of water is needed to attenuate their initial intensity to <5%, whereas the same amount of water is sufficient to shield 270 keV electrons (see Figure 1-6 for different ranges expected for photons and electrons [52,75]). Although dose from photons are generally lower than charged particles due to their large range relative to energy, LEE-emitting radionuclides for RPT should be filtered based on select criteria to maximize the potential for improving the therapeutic window beyond β- and α-emitters [64,65]. Such considerations are discussed in the next paragraph.

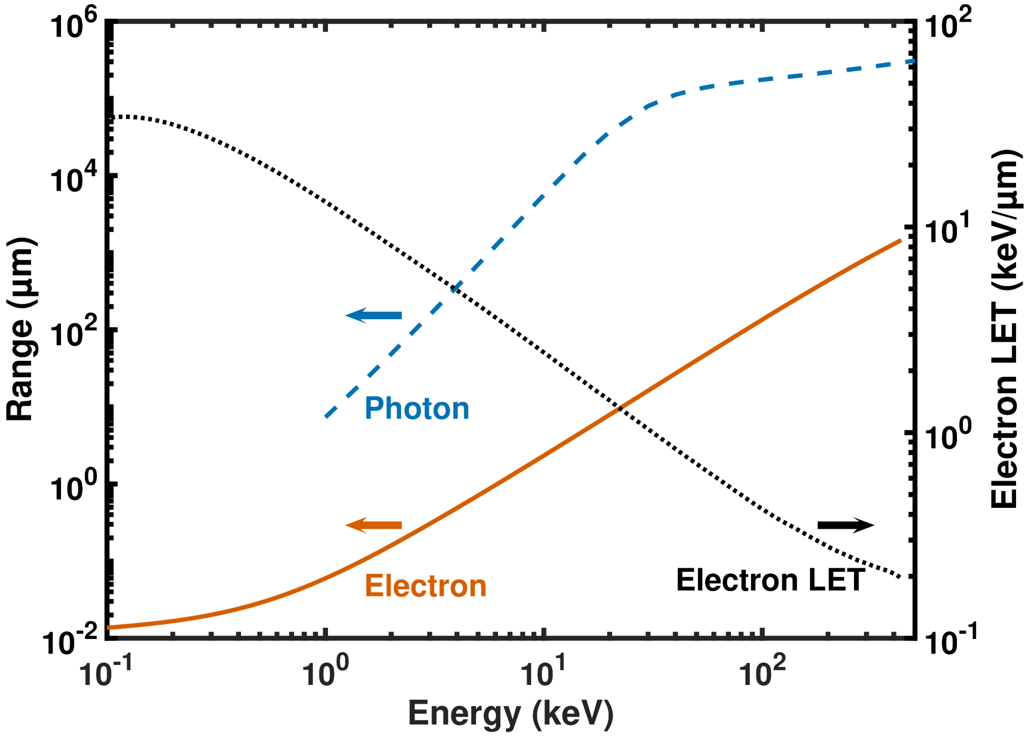

Figure 1-6 Electron (solid) and photon (dashed) range in water as a function of energy. The "range" of photons in water was assumed to be the amount of water needed to attenuate 95% of the incident photon intensity, calculated using the exponential law. The range of electrons in water refers to the R_{CSDA} range. The dotted line corresponds to the unrestricted electronic stopping power of electrons at each respective energy, referred to as Electron LET. Arrows depict the axes that each line references. Photon mass attenuation coefficients and electron R_{CSDA} in water were taken from [75] and [52], respectively. Electronic stopping power for electrons in water was taken from [52].

To reduce the off-target dose, LEE-emitting radionuclides for RPT applications should have high electron-to-photon energy ratios. Also, since LEE-emitters are defined to have less energy compared to the average energy of conventional β particles, 50 keV is often used as a cut-off for the maximum electron energy [64] though other limits related to range and LET may be more suitable based on radiobiological effects. Thus, a good selection criterion could be that the total energy emitted from electrons with <50 keV of kinetic energy outweighs contributions from higher energy electrons and photons. Although a large electron yield may enhance cytotoxicity when coupled to DNA, likely due to increased multiply damaged sites, there is still no evidence of enhanced potency in other scenarios [65]. The remaining criteria for utilizing LEE-emitting radionuclides in RPT are then akin to the selection criteria of other radionuclides. I.e., the half-life should be within hours-days to accommodate transport and handling, chemical processing and *in vivo* pharmacokinetics of the agent. Practically, the radionuclide should be capable of being produced in sufficient quantities, be (radio)chemically pure and stable for *in vitro/in vivo* applications. High radionuclidic and radioisotopic purity are desirable to limit contamination of higher energy electrons and photons. Due to the low physical dose of LEEs at the tissue and organ scale, administered activity may need to be substantially higher than with β- emitters. Consequently, the (apparent) molar activity (AMA), one measure of radiochemical purity, needs to be even higher to avoid administering excess targeting vector that could begin to influence biological processes and/or receptor saturation [37].

Simulations and mathematical models are often used to better predict radiobiological effects from different decay characteristics [76–80]. The dosimetric consequences of a high electron-to-photon energy ratio discussed above can be directly visualized from simulating the absorbed energy fraction (AEF) of different sized tissues. To simplify the model, and to facilitate reproducibility between different researchers, tumor and most organ tissues are often set as water for dosimetry purposes [61,76,81,82]. Thus, the list of promising candidates for LEE RPT can be efficiently filtered by simulating the AEF in tumor of various sizes for different radionuclides. For example, radionuclides that deposit most of their decay energy within shorter distances relative to α-emitters could potentially achieve better therapeutic windows. Based on simulated results from Figure 1-7, radionuclides that achieve AEF>0.5 before ^{225}Ac and ^{211}At (clinically relevant α-emitters) are ^{71}Ge ($t_{1/2}$=11.43 d, LEE 5.01 keV/decay, photon 4.15 keV/decay), ^{58m}Co ($t_{1/2}$=9.04 h, LEE 22.8 keV/decay, photon 2.01 keV/decay), ^{189m}Os ($t_{1/2}$=5.8 h, LEE 28.6

keV/decay, photon 2.24 keV/decay), ^{103m}Rh ($t_{1/2}$=56.114 min, LEE 37.6 keV/decay, photon 1.72 keV/decay) and ^{119}Sb ($t_{1/2}$=38.19 h, LEE 25.8 keV/decay, photon 23.3 keV/decay), in order of lowest size at which AEF reaches 0.5.

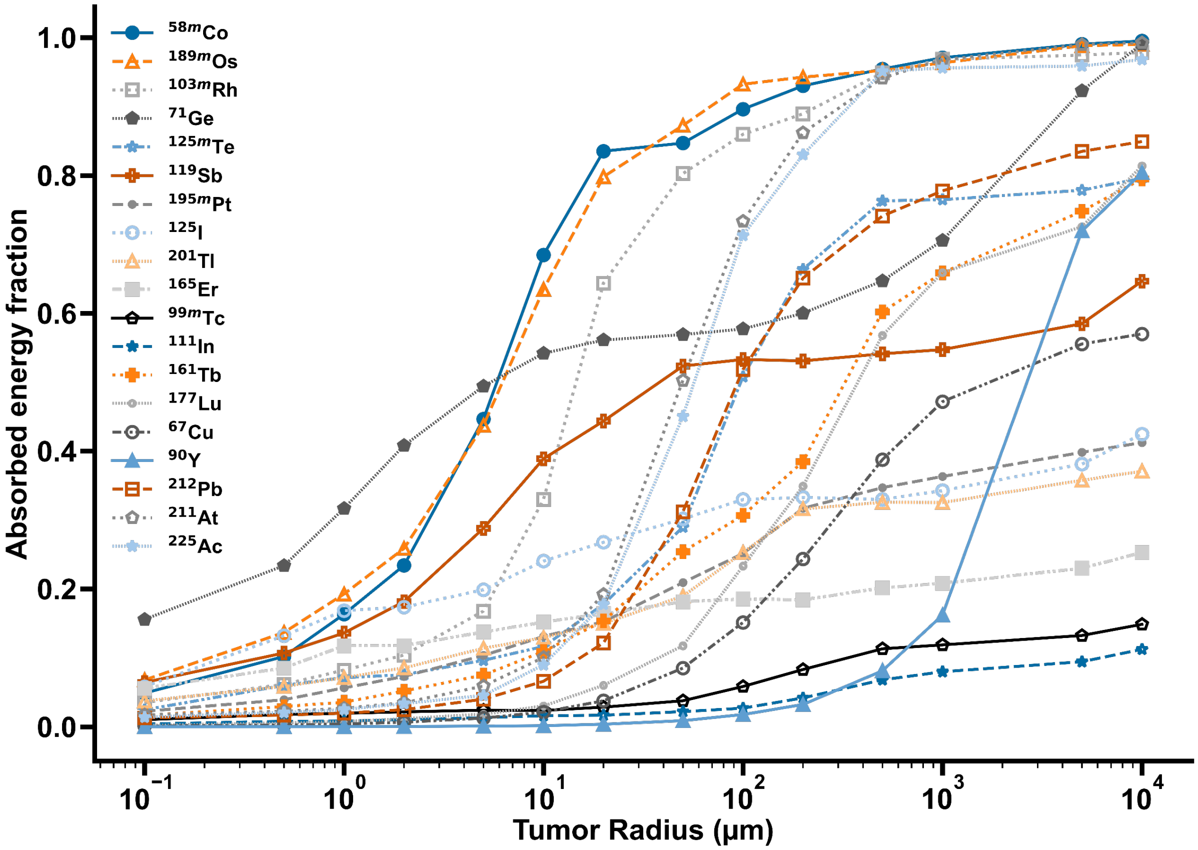

Figure 1-7 The fraction of absorbed radiation dose (absorbed energy fraction, AEF) in various tumor sizes of several radionuclides that may be relevant to RPT. AEF was simulated by uniformly distributing radionuclides within a solid sphere of water with unit density (1 g/cm^3) in Geant4. The variation between runs was less than 10% (>500k trials per run). The low AEF from ^{195m}Pt can be attributed to the different decay characteristics between Geant4 and ICRP107 [83] (see Figure 1-8). The simulation utilized the G4EmLivermorePhysics physics package with the electron cut-off energy at 10 eV, fluo, auger and augerCascade turned on and pixe turned off. These results are in relatively good agreement (within ~15%) between analytical methods from MIRDCell [78] and other published results using Monte Carlo methods [81].

The energetic contribution of each major transformation from these radionuclides is shown in Figure 1-8, where it is apparent that ^{58m}Co, ^{189m}Os and ^{103m}Rh can achieve AEF>0.9 before ^{225}Ac and ^{211}At due to their low photon contribution. Unlike ^{189m}Os and ^{103m}Rh, ^{58m}Co can be produced from low energy cyclotrons, effectively separated from the target material and stabilized by chelators commonly used in radiopharmaceuticals such as NOTA (1,4,7-triazacyclononane-1,4,7-triacetic acid) and DOTA (1,4,7,10-tetraazacyclododecane-1,4,7,10-tetraacetic acid) [84]. Thus, ^{58m}Co has been one of the most suggested candidates for LEE RPT applications [64,65,76] though it has only been sparsely produced for RPT applications within the last decade [84–88].

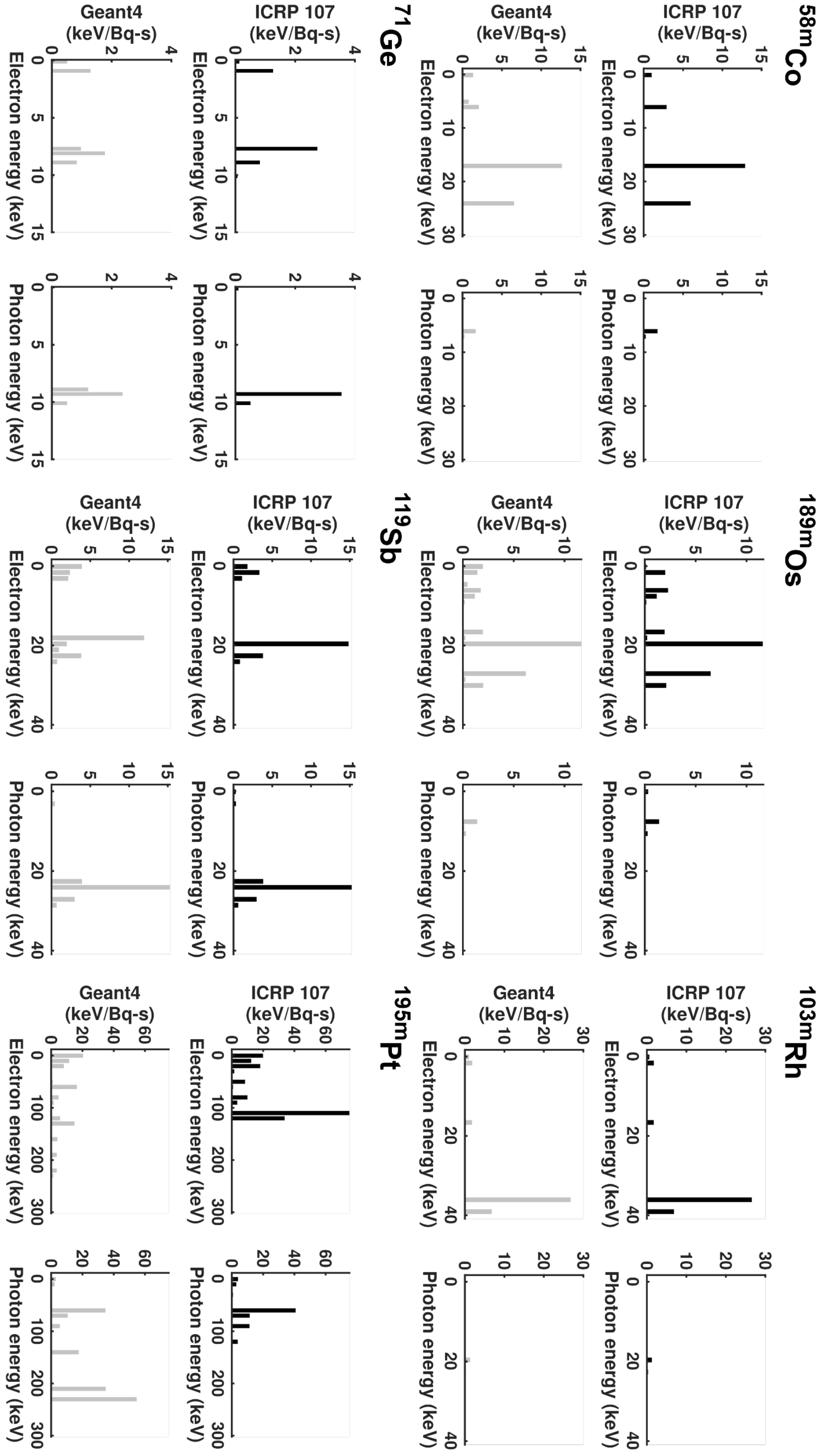

Figure 1-8 Total energy contribution per decay from each transformation of selected LEE-emitting radionuclides. Nuclear decay data taken from ICRP 107 [83] are presented in black bars whereas nuclear data determined from Geant4 simulations are presented in gray bars. The decay characteristics suggest that ^{71}Ge and ^{119}Sb should barely achieve AEF=0.5 for microdosimetry applications, which corroborates results from Geant4 simulations. There is a clear discrepancy between ICRP107 and Geant4 for ^{195m}Pt, whereas the decay characteristics match well for other LEE-emitters. The total decay energy between ICRP107 and Geant4 for all radionuclides was within <4%.

To better elucidate the behavior of ^{58m}Co for RPT applications, Figure 1-9 compares microdosimetry values for various radionuclides relative to ^{58m}Co. The cellular S-value ($S_{X \leftarrow Y}$) refers to the proportionality constant that determines the amount of dose deposited in region X from source region Y per time-integrated activity (thus, $S_{X \leftarrow Y}$ has units of [Gy]/[Bq-s]). The 100 μm sphere reference used for off-target radiation dose matches the maximum range in water for α-particles emitted by clinically relevant radionuclides (4-10 MeV) [51], and can be relevant for assessing radionuclides for treating circulating tumor cell clusters. Although cellular S-values are greater for alpha emitters in general, the relative increase in off-target dose is >35x the improvement in S-values. In addition to the practical benefits of ^{58m}Co discussed previously, these microdosimetry comparisons also indicate that ^{58m}Co is a promising candidate for LEE RPT applications.

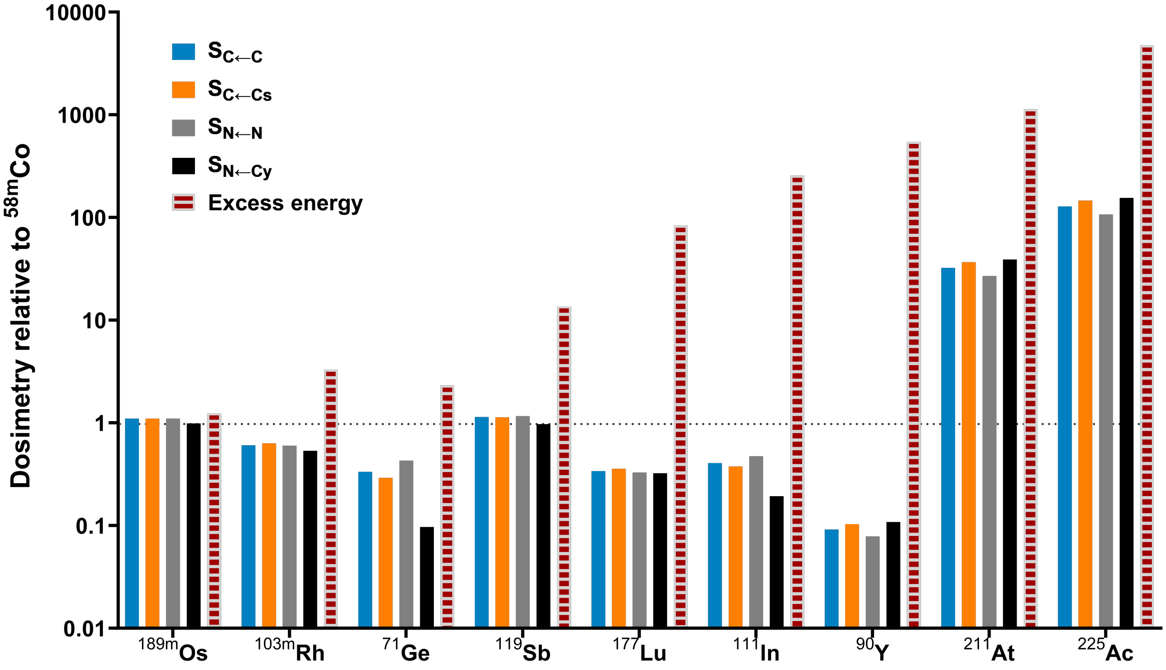

Figure 1-9 (Micro)dosimetry values for several radionuclides relative to ^{58m}Co (>1 implies the radionuclide is better than ^{58m}Co, except for excess energy). All S-values refer to self-dose, where B←A implies A is the source of the radionuclide and B is the target of interest. C: cell, Cs: cell surface, N: cell nucleus and Cy: cytoplasm. Cellular S-values were computed using MIRDCell software [78] (cell radius 8 µm, cell nucleus radius 5 µm), with nuclear decay data from ICRP107 [83] if unavailable in the software. The total alpha decay energy for ^{225}Ac and ^{211}At from MIRDCell was 27.7 MeV and 6.78 MeV (Geant4 simulation used 29.6 MeV and 6.96 MeV), respectively. All daughters for ^{225}Ac and ^{211}At were included. Excess energy refers to the average residual energy per decay not absorbed by a 100 µm radius sphere of water, assuming uniform distribution. Excess energy calculations for ^{225}Ac and ^{211}At were normalized to decay energies used in MIRDCell for consistency.

Despite not being directly associated with the decay characteristics of LEE-emitters, another practical consideration is the possibility for tracking the radiopharmaceutical agent *in vivo*. *In vivo* assessments allow researchers and clinicians to assess the dosimetry of the compound and can also be useful for predicting patient outcomes without compromising patient quality of life. As previously alluded to, theranostic applications using different radioisotopes of the same element enables the most accurate derivation of dosimetry [37]. Fortunately, ^{58m}Co has the diagnostic congener ^{55}Co ($t_{1/2}$=17.5 h, $I_{\beta+}$=77 %, <$E_{\beta+}$>=569 keV; I_{γ}=75 %, E_{γ}=931.1 keV), a positron emitter useful for non-invasive positron emission tomography (PET) imaging, which can also be produced from low energy cyclotrons. Independent of ^{58m}Co applications, ^{55}Co has also piqued the community's interest in Co radiopharmaceuticals owing to their unique chemistry [89] and improved tumor uptake compared to other radionuclides [90,91]. Furthermore, the production pathways for ^{55}Co can avert long-lived radionuclides to simplify radioactive waste management. Figure 1-10 illustrates the major production pathways for ^{55}Co and ^{58m}Co using low energy accelerators (<30 MeV), where target isotopes may be ^{58}Ni/^{54}Fe and ^{55}Mn/^{57}Fe/^{58}Fe/^{61}Ni, respectively, depending on the type of particles being accelerated. Explicitly, p, d, n and α refer to proton (^{1}H), deuteron (^{2}H), neutron (^{1}n) and alpha particle (^{4}He), respectively. Although ^{60}Ni(d,α)^{58m}Co is not practical at <30 MeV in comparison to the other reaction pathways (less yield than ^{61}Ni(p,α)^{58m}Co), this route becomes viable for deuteron energies >35 MeV. Aside from ^{55}Mn, the only stable isotope of manganese, each of these target isotopes should be enriched to achieve high radionuclidic and radioisotopic purity and increase radionuclide yield. The cost of most enriched isotopes has increased due to recent political circumstances that limit their availability, but all enriched target isotopes for ^{55}Co and ^{58m}Co production can be recycled with high recovery [87,92–94]. Additionally, the energy of the bombarding particle may modulate radionuclidic purity and yield. Although the radionuclidic purity can increase from radioactive decay if the desired radionuclide has a longer half-life than co-produced radio-contaminants, most radio-Co contaminants are long lived.

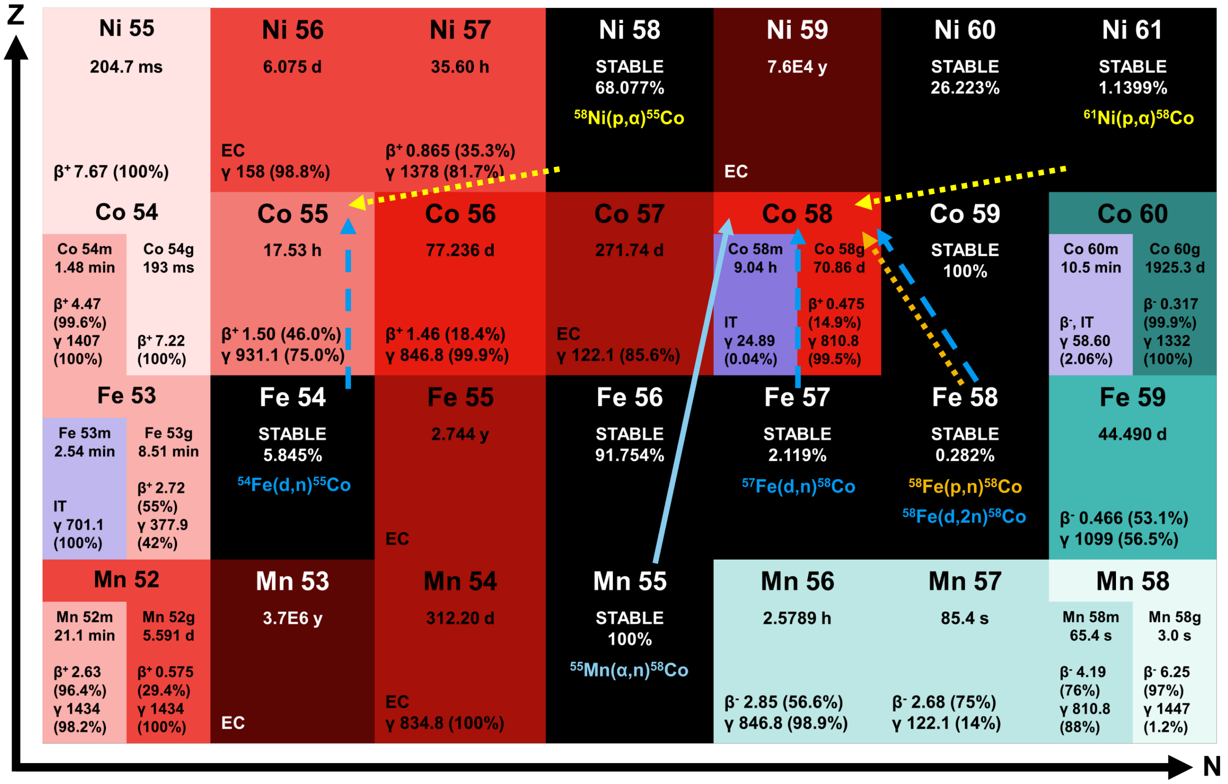

Ni 55 204.7 ms β^+ 7.67 (100%)	**Ni 56** 6.075 d EC γ 158 (98.8%)	**Ni 57** 35.60 h β^+ 0.865 (35.3%) γ 1378 (81.7%)	**Ni 58** STABLE 68.077% ^{58}Ni(p,α)^{55}Co	**Ni 59** 7.6E4 y EC	**Ni 60** STABLE 26.223%	**Ni 61** STABLE 1.1399% ^{61}Ni(p,α)^{58}Co
Co 54 Co 54m 1.48 min β^+ 4.47 (99.6%) γ 1407 (100%) Co 54g 193 ms β^+ 7.22 (100%)	**Co 55** 17.53 h β^+ 1.50 (46.0%) γ 931.1 (75.0%)	**Co 56** 77.236 d β^+ 1.46 (18.4%) γ 846.8 (99.9%)	**Co 57** 271.74 d EC γ 122.1 (85.6%)	**Co 58** Co 58m 9.04 h IT γ 24.89 (0.04%) Co 58g 70.86 d β^+ 0.475 (14.9%) γ 810.8 (99.5%)	**Co 59** STABLE 100%	**Co 60** Co 60m 10.5 min β^-, IT γ 58.60 (2.06%) Co 60g 1925.3 d β^- 0.317 (99.9%) γ 1332 (100%)
Fe 53 Fe 53m 2.54 min IT γ 701.1 (100%) Fe 53g 8.51 min β^+ 2.72 (55%) γ 377.9 (42%)	**Fe 54** STABLE 5.845% ^{54}Fe(d,n)^{55}Co	**Fe 55** 2.744 y EC	**Fe 56** STABLE 91.754%	**Fe 57** STABLE 2.119% ^{57}Fe(d,n)^{58}Co	**Fe 58** STABLE 0.282% ^{58}Fe(p,n)^{58}Co ^{58}Fe(d,2n)^{58}Co	**Fe 59** 44.490 d β^- 0.466 (53.1%) γ 1099 (56.5%)
Mn 52 Mn 52m 21.1 min β^+ 2.63 (96.4%) γ 1434 (98.2%) Mn 52g 5.591 d β^+ 0.575 (29.4%) γ 1434 (100%)	**Mn 53** 3.7E6 y EC	**Mn 54** 312.20 d EC γ 834.8 (100%)	**Mn 55** STABLE 100% ^{55}Mn(α,n)^{58}Co	**Mn 56** 2.5789 h β^- 2.85 (56.6%) γ 846.8 (98.9%)	**Mn 57** 85.4 s β^- 2.68 (75%) γ 122.1 (14%)	**Mn 58** Mn 58m 65.4 s β^- 4.19 (76%) γ 810.8 (88%) Mn 58g 3.0 s β^- 6.25 (97%) γ 1447 (1.2%)

Figure 1-10 Relevant target isotopes for producing ^{55}Co and ^{58m}Co demonstrated on a chart of the nuclide format. N refers to the neutron number and Z refers to the proton number. The reaction pathway is listed under the stable isotope of interest, where arrows point from the target to the product. Different incident particles are denoted by different line styles (proton: dotted, deuteron: dashed, alpha: solid). Only the most intense transitions are listed, and β^+ decay implies electron capture (EC) may be possible as well. β^- and β^+ energies are in MeV, whereas γ energies are in keV. Decay data were retrieved from NuDat 3.0 [95].

Each nuclear reaction pathway has its own associated threshold energy, with most having a sharp increase in nuclear cross section after exceeding this limit. The nuclear cross section is a measure of the probability that a nuclear reaction will proceed (typically measured as barn or mbarn, where 1 barn=10^{-24} cm^2 and would be considered highly probable), and the nuclear cross section as a function of energy is known as the excitation function (see Appendix A for a brief discussion on calculating nuclear cross sections). Consequently, the number of available nuclear reactions inevitably increases with increase in energy, and additional pathways will compete against reactions with lower threshold energy. The radionuclide yield [96] can be calculated by integrating the excitation function, where the target thickness will determine the end point of the integration limit. Figure 1-11 through Figure 1-13 show semi-empirical excitation functions from TENDL-2023 [97] that are relevant for ^{55}Co and ^{58m}Co production. The 30 MeV upper limit for Figure 1-11 through Figure 1-13 was chosen to be inclusive for most accelerators used in clinical radionuclide production facilities. Since TENDL-2023 excitation functions for these reactions are in fair agreement with experimentally determined cross sections, experimental cross sections were not included to aid visualization. Although the most optimal case would be to only produce the desired radionuclide, it is often not possible to preclude the formation of other radionuclides due to overlapping excitation functions. Other co-produced radionuclides should be separated from the desired radionuclide(s) to prevent confounding results in evaluating experimental data. Also, producing radionuclides with longer half-lives often requires additional regulatory oversight (e.g., half-lives <65-100 days may be considered “very short-lived waste” and do not require additional licensing [98]). Fortunately, Mn, Fe and Ni may be chemically separated from Co to achieve high radionuclidic purity so radioisotopic purity is generally the limiting factor [92,99–101]. The ^{58}Ni(p,x) pathway (Figure 1-11, left) shows that ^{55}Co can only be produced with high radioisotopic purity at <12 MeV, whereas ^{55}Co can be produced with high radioisotopic purity via ^{54}Fe(d,x) (Figure 1-11, right) for the entire energy range (excluding ^{54}Co and ^{53}Co since their half-lives are <0.3 ms and ^{56}Co since the cross sections only span 10^{-4}-10^{-1} mbarn in this energy range). Moreover, the cross sections for ^{54}Fe(d,n)^{55}Co is about an order of magnitude larger than ^{58}Ni(p,α)^{55}Co which will result in more ^{55}Co being produced in addition to the wider energy range available. With regards to availability, both ^{54}Fe and ^{58}Ni can be purified to >99% [92,93] and can be acquired for ~$5/mg and ~$1/mg, respectively, in their metallic form. The price of ^{54}Fe relative to ^{58}Ni may seem large but recycling efficiencies are typically >95% which makes the effective operational cost <$0.25/mg. For example, a 1 cm diameter target with 600 mg of ^{54}Fe can fully degrade 30 MeV deuterons (Figure 1-14A) and would only lose $150 of target material per production which pales in comparison with the operating costs of personnel and particle accelerator. Thus, if deuteron accelerators are available, ^{54}Fe is an optimal target isotope for ^{55}Co production since ^{54}Fe(d,n)^{55}Co can achieve high radioisotopic purity and substantially greater yield without being economically limited.

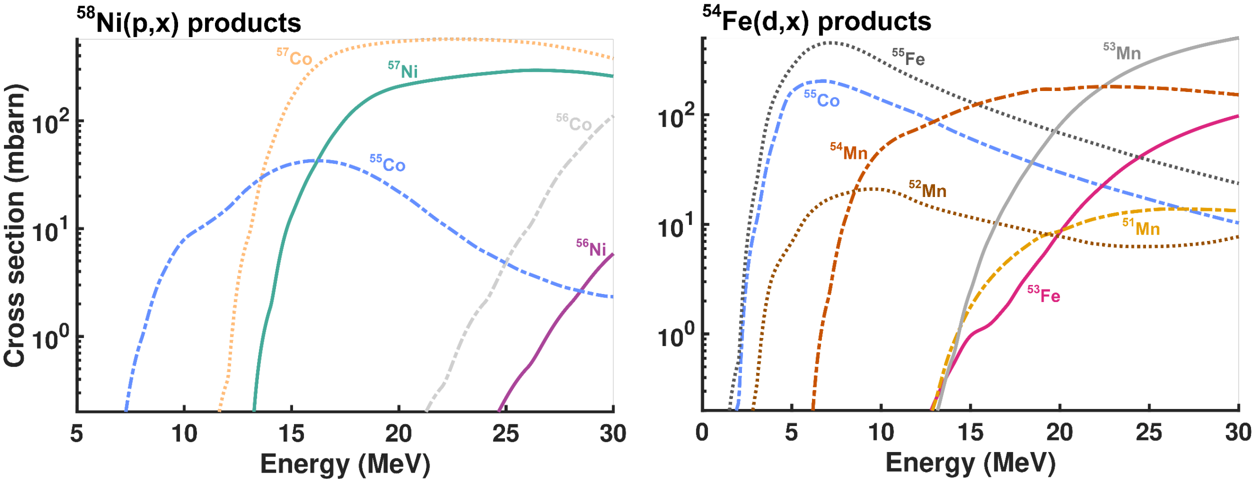

^{58}Ni(p,x) products

^{54}Fe(d,x) products

Figure 1-11 Excitation functions of several nuclear reactions relevant for ^{55}Co production using data from TENDL-2023 [97].

On the other hand, all ^{58m}Co production pathways (Figure 1-12) will co-produce ^{58g}Co ($t_{1/2}$=70.86 d, $I_{\beta+}$=14.9 %, $E_{ave,\ \beta+}$=201.1 keV; I_γ=99.45 %, E_γ=810.76 keV) in addition to ^{58m}Co decay. The daughter and co-produced ^{58g}Co was ignored for (micro)dosimetry applications because the impact of ^{58g}Co can be significantly reduced by modulating the biological half-life. Since ^{58g}Co is a positron emitter, ^{58g}Co can also be used to corroborate dosimetry derived from ^{55}Co and to potentially track *in vivo* ^{58m}Co decay daughters. Practically, due to PET imaging counting statistics, this would require targeting vectors with high uptake in tissues. Unless otherwise noted, samples with higher ^{58m}Co activity compared to ^{58g}Co are referred to as ^{58m}Co for simplicity. From Figure 1-12, ^{61}Ni(p,α)^{58m}Co, ^{57}Fe(d,n)^{58m}Co and ^{55}Mn(α,n)^{58m}Co can attain higher radioisotopic purity relative to ^{58}Fe(p,n)^{58m}Co due to lower angular momentum transfer of (p,n) reactions. Each of the ^{58m}Co production pathways is further limited by either the availability of the target isotope (^{58}Fe, ^{61}Ni), availability of accelerator (α-beam), or radioisotopic purity (^{57}Fe(d,2n)^{57}Co). Interestingly, despite experimental cross section data for ^{58m}Co and ^{58g}Co [102] agreeing well with calculated results presented in Figure 1-12, a significantly different ^{58g}Co/$^{58m+g}$Co was reported for ^{58}Fe(p,n)^{58m}Co at 10.1 MeV after 1 h of irradiation (expected >1.1% ^{58g}Co/$^{58m+g}$Co, reported 0.85±0.04% ^{58g}Co) [94].

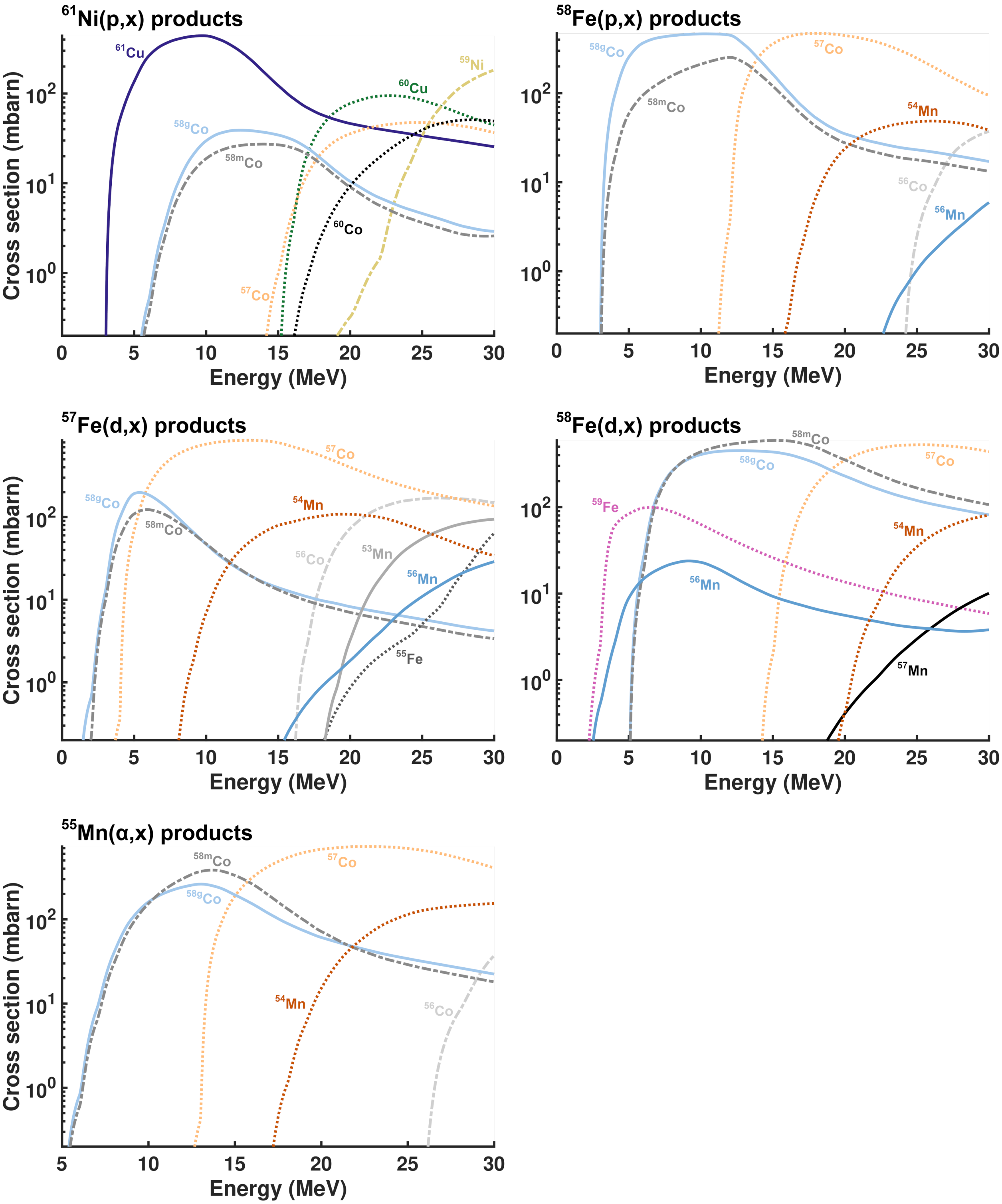
^{61}Ni(p,x) products

^{58}Fe(p,x) products

^{57}Fe(d,x) products

^{58}Fe(d,x) products

^{55}Mn(α,x) products

Figure 1-12 Excitation functions of several nuclear reactions relevant for ^{58m}Co production using data from TENDL-2023 [97].

Although ^{61}Ni(p,x), ^{58}Fe(p,x) and ^{58}Fe(d,x) can potentially avoid ^{57}Co (^{57}Co, $t_{1/2}$=271.74 d, I_γ=85.60%, E_γ=122.06 keV), isotopically pure ^{58}Fe and ^{61}Ni are difficult to acquire, and will cost >\$100/mg even if they are available for purchase. Similarly, despite the low cost of ^{55}Mn and the possibility for ^{55}Mn(α,x) precluding ^{57}Co formation, there are currently few α-particle accelerators across the world for isotope production and beam time is often occupied by (pre)clinical production of ^{211}At or other radionuclides.

For preclinical evaluations, this leaves ^{57}Fe as the most practical target material for ^{58m}Co, though ^{58}Fe will eventually be necessary to produce clinically relevant quantities. Compared to the other options, ^{57}Fe is ~\$10/mg, and deuteron accelerators are much more prevalent than α-particle accelerators. However, ^{57}Fe(d,x) produces the contaminant ^{57}Co via ^{57}Fe(d,2n)^{57}Co above 4 MeV, which will require additional coordination for shielding long-lived radioactive biohazard waste. The amount of co-produced ^{57}Co should not alter the dosimetry of ^{58m}Co RPT agents unless the targeting vector remains in the body for extended periods of time (>months). The University of Wisconsin-Madison Cyclotron Research Group has historically adopted ^{57}Fe(d,n)^{58m}Co for preclinical evaluations of ^{58m}Co given the lack of ^{61}Ni and ^{58}Fe.

Cobalt-55 production using isotopically enriched ^{54}Fe targets will need to consider ^{56}Fe contamination due to large ^{56}Fe(d,n)^{57}Co cross sections even at low energies. Fortunately, ^{54}Fe and ^{56}Fe differ by two mass units which enables separations with higher resolution. Since producing ^{58m}Co via ^{57}Fe(d,n)^{58m}Co will lead to ^{57}Fe(d,2n)^{57}Co in much greater quantities compared to ^{56}Fe(d,n)^{57}Co (assuming >90% ^{57}Fe enrichment), ^{56}Fe impurity only reduces ^{58m}Co yield. As shown in Figure 1-12 (center left and right), ^{58}Fe(d,2n)^{58m}Co is more favorable than ^{57}Fe(d,n)^{58m}Co so ^{58}Fe ‘contamination’ will increase yield and improve the radioisotopic purity of ^{58m}Co. Table

1-2 summarizes the information regarding nuclear reaction pathways for producing ^{55}Co and/or ^{58m}Co.

Table 1-2 Summary of the nuclear reactions relevant for producing ^{55}Co and ^{58m}Co. Feasibility and availability were classified according to the availability of target material and the bombarding particle type. Except for ^{61}Ni(p,α)^{58m}Co, which assumed 14 MeV protons, radionuclide yield determination assumed incident energies of 11, 8.2 and 13 MeV for protons, deuterons, and alphas, respectively, and thick targets. Calculated physical thick target yield values are shown in Figure 1-14B. The colon notation refers to the proportion of ^{58m}Co:^{58g}Co produced. For example, “1:2” refers to 1 and 2 nuclei of ^{58m}Co and ^{58g}Co produced, respectively (not activity). The bolded and underlined nuclear reactions are deemed the most practical for preclinical research based on the discussions in the text.

Nuclear reaction	Target price ($USD)	Radionuclide yield	Likely contaminants
^{58}Ni(p,α)^{55}Co	~$1/mg	Very low	None <11 MeV
^{54}Fe(d,n)^{55}Co	**~$5/mg**	**Moderate**	**^{52,54}Mn, ^{55}Fe**
^{61}Ni(p,α)^{58m}Co	~$100/mg	Low	^{61}Cu, *no ^{57}Co <14 MeV*, 1:1 ^{58g}Co
^{58}Fe(p,n)^{58m}Co	>$100/mg	Very high	None <11 MeV, 1:2 ^{58g}Co
^{57}Fe(d,n)^{58m}Co	**~$10/mg**	**Moderate**	**^{54}Mn, ^{57}Co, 1:1 ^{58g}Co**
^{58}Fe(d,2n)^{58m}Co	>$100/mg	Moderate, very high >10 MeV	^{56}Mn, ^{59}Fe, *no ^{57}Co <14 MeV*, 3:2 ^{58g}Co
^{55}Mn(α,n)^{58m}Co	<1$/mg (*RARE α*)	Low	None <13 MeV, 3:2 ^{58g}Co

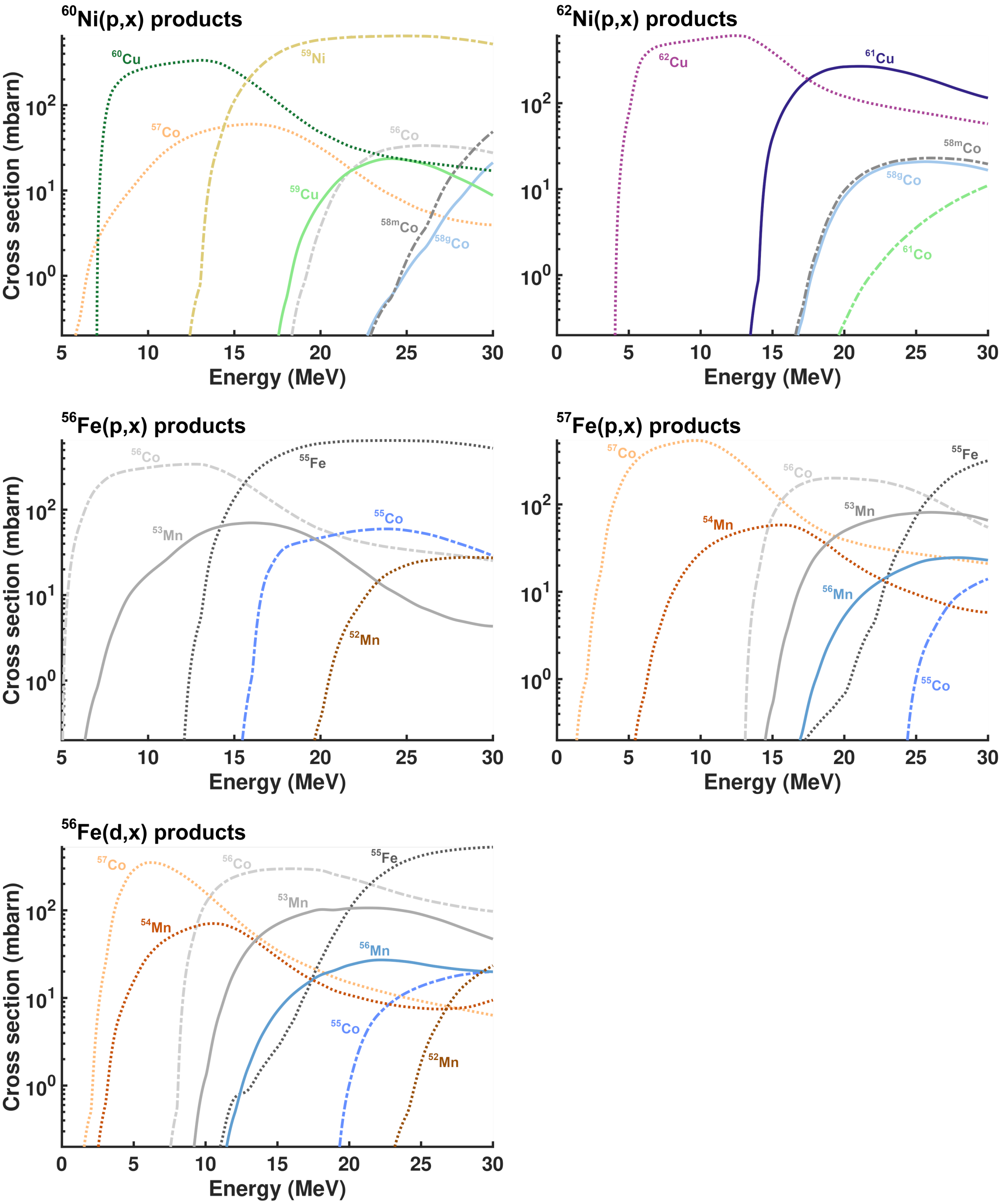

Figure 1-13 Excitation functions of several nuclear reactions from the most likely contaminating isotopes for ^{55}Co and/or ^{58m}Co production using data from TENDL-2023 [97].

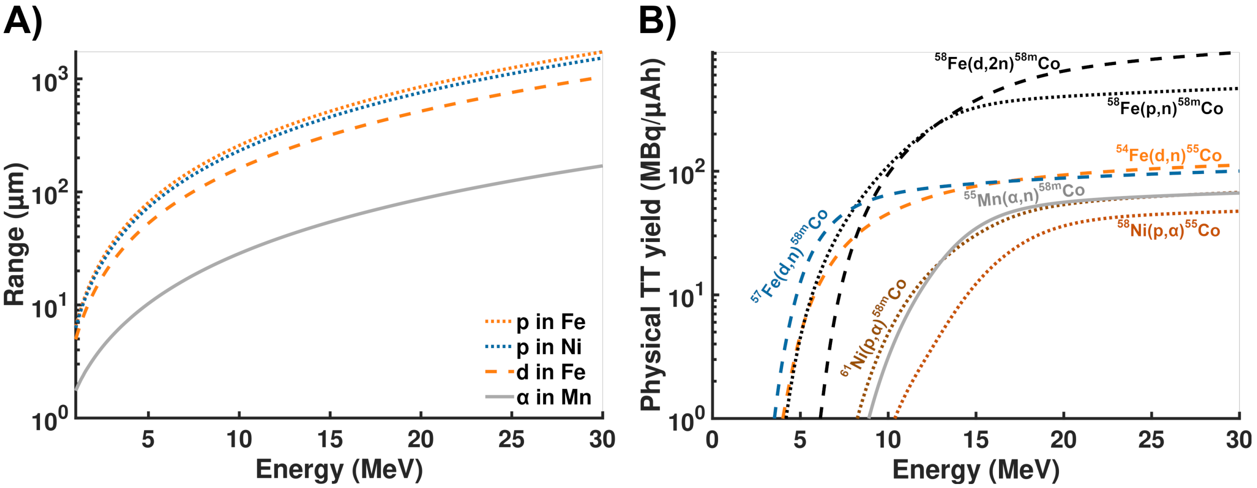

Figure 1-14 A) Range of different particles in target isotopes for ^{55}Co and/or ^{58m}Co production. Incident protons (p) are displayed in dotted lines, deuterons (d) in dashed lines and alphas (α) in solid lines. The range of particles in matter was calculated using SRIM software [48]. B) The physical thick target (TT) yield of ^{55}Co and ^{58m}Co in MBq/µAh from several nuclear reaction pathways using cross section data from TENDL-2023 and stopping power and range from SRIM.

Despite the promising characteristics of ^{58m}Co for LEE RPT, there has been scant literature available regarding *in vitro* and *in vivo* biological applications of ^{58m}Co [86,88,103]. One of the first studies utilizing ^{58m}Co with an internalizing probe targeting the type 2 somatostatin receptor ([^{58m}Co]Co-DOTA-TATE) demonstrated improved *in vitro* cytotoxicity per cumulative decay compared to ^{111}In and ^{177}Lu using the same targeting vector [86]. Cellular dosimetry calculations from Figure 1-9 and [77,94] have predicted improved dose deposition from ^{58m}Co to the target cell compared to radionuclides that emit higher energy electrons, but such dosimetric considerations have not been validated until published results from [86]. Despite the promising results from [86], there have been no published results of *in vivo* applications of [^{58m}Co]Co-DOTA-TATE. From another study evaluating the feasibility of producing sufficient ^{58m}Co for immuno-RPT applications, ^{58m}Co was conjugated to an anti-CD105 antibody ([^{58m}Co]Co-NOTA-TRC105), targeting vasculature associated with the tumor microenvironment, and administered *in vivo* using a murine xenograft model [103].

Although the authors demonstrated that it is feasible to produce ^{58m}Co in sufficient quantities for preclinical evaluations, the high circulation time of [^{58m}Co]Co-NOTA-TRC105 and lack of internalization likely led to the lack of therapeutic response observed in the study even after administering a total of 300 MBq (8 mCi) [^{58m}Co]Co-NOTA-TRC105 per mouse. More recently, the group from [86] published an *in vivo* therapy study that treated murine xenograft models with ^{58m}Co [88]. The ^{58m}Co radiopharmaceutical targeting prostate cancer ([^{58m}Co]Co-DO3A-PSMA-617) was not as highly internalizing as in [86] and did not have as high tumor uptake but had increased intracellular uptake in the nucleus. The results from [88] demonstrated a dose-dependent *in vitro* cytotoxic effect from [^{58m}Co]Co-DO3A-PSMA-617 and had low *in vitro* toxicity to control cells with low target expression. Furthermore, *in vivo* therapy results demonstrated increased median survival with one mouse having complete response following two doses of 144 MBq (3.9 mCi) [^{58m}Co]Co-DO3A-PSMA-617 (7 days apart). These nascent results, though preliminary, suggest ^{58m}Co may be viable as a therapeutic radionuclide, and more research is warranted. Thus, this dissertation aims to elucidate various radiochemical and radiopharmaceutical applications of $^{55/58m}$Co given the sparse literature available.

Developing novel radionuclides into useful RPT agents requires high chemical, radiochemical and radionuclidic purity to enable adoption and application. In addition to avoiding adverse biological effects, cancer cell receptor saturation can also be mitigated by improving AMA of the radiolabeled compounds. The maximum dose to tumor from a single administration of activity is proportional to the energy released per unit activity, AMA, receptor density and cell density of the tumor, and is independent of the mass of the tumor if the receptor density and cell density do not change with tumor growth or death. For example, assuming a cell density of 10^9 cells/cm^3 (upper bound [104]) and 10^5 receptors/cell, this results in 10^{14} receptors/cm^3. Using Avogadro's number and assuming the tumor has a density of 1 g/cm^3, the maximum tumor uptake would be 0.17 nmol/g. Assuming an acceptable AMA of 37 MBq/nmol, this implies a maximum of 6.3 MBq/g can be delivered to the tumor in a single dose. For ^{58m}Co (decay energy of 0.19 mJ/MBq), this would deliver at most 1.2 Gy to the tumor in a single dose, which is far less than the typical 15-20 Gy prescription doses. Consequently, it is imperative to achieve the largest AMA to maximize the therapeutic potential for low-energy, short half-life LEE emitters like ^{58m}Co. Existing methods [92,94] to separate cyclotron produced $^{55/58m}$Co from iron targets require lengthy processes and/or long irradiation times, which lead to decreased activities and radioisotopic purities due to the short half-life of ^{58m}Co. Also, because of the retention of iron target material on anion exchange resin during the separation procedure, the current methods require large solution volumes and more resin material to maintain similar separation factors when scaling up the mass of the iron targets. Chapter 2 exploits the differences in chloride speciation between Co and Fe to expediate the Fe recovery process by using cation exchange chromatography and couples it to extraction chromatography to further improve the sample purity. The cation exchange-extraction chromatography procedure can reduce the overall separation time, maintain high Fe and Co recovery, and improve AMA for NOTA and DOTA compared to previously published methods, thereby facilitating $^{55/58m}$Co development for RPT applications.

Although Co can form stable complexes *in vivo* with several clinically relevant chelators, there is little to no literature for complexing nanomolar Co with the sarcophagine (Sar) construct. This is unfortunate as macroscopic Co-sarcophagine complexes exhibit high kinetic inertness under various stringent conditions [105,106] and have interesting biological behavior [107]. To fill this gap, Chapter 3 explores n.c.a. ^{55}Co radiolabeling to DiAmSar (DSar) and evaluates the stability of the radiolabeled compound by incubating against human serum and ethylenediaminetetraacetic acid (EDTA) solution. Following this, ^{55}Co-radiolabeled Sar compounds are administered *in vivo* in mice to assess the tumor-targeting potential of Co-Sar radiopharmaceuticals. The results of these preliminary studies demonstrate that Co-Sar radiopharmaceuticals are promising and may hold pharmacokinetic advantages over Cu-Sar radiopharmaceuticals, though systematic studies are needed to ascertain these findings.

Since Co may exist as Co(II) or Co(III) in aqueous media with appropriate stabilizing agents, resulting cobalt-chelate complexes may be prone to oxidation. The oxidation state of the radionuclide can considerably alter the biodistribution [108,109], though this behavior has not been explored with radio-Co. In contrast to Co-Sar complexes that spontaneously oxidize upon exposure to air due to their low reduction potential [110], Co-NO2A and -NOTA have higher reduction potential [111,112] which may lead to multiple chemical species after complexation. Chapter 4 explores the oxidation state of various Co-NOxA complexes at nanomolar concentration by using ^{55}Co. The impact of pH, temperature, time, Co concentration and reducing/oxidizing agents on oxidation kinetics are also investigated. NO2A-PSMA-617, NOTA-PSMA-617 and DO3A-PSMA-617 were then radiolabeled with ^{55}Co and administered in mice to evaluate potential differences in the biodistribution profile. Despite previous studies comparing different chelators with ^{55}Co, [^{55}Co]Co-NO2A and -NOTA were assumed to stabilize Co(II) even after complexation [113,114]; results from Chapter 4 suggests otherwise.

With examples in the preceding chapters on production, separation, chelation and oxidation chemistry, Chapter 5 applies $^{55/58m}$Co for theranostic RPT targeting the type 1 neurotensin receptor (NTSR1). The type 1 neurotensin receptor (NTSR1) is expressed by a variety of cancers including breast, pancreatic, prostate, colon and non-small cell lung cancers [115], and the ligand-receptor complex has been shown to internalize close to the cell nucleus [116,117]. Endogenous neurotensin (NTS) has sub-nanomolar affinity for NTSR1 [118] which enables NTS to be used in trace quantities commonly employed in nuclear medicine applications. Due to the rapid degradation of endogenous neurotensin *in vivo*, several modifications have been investigated to enhance the metabolic stability [115,119–122]. For example, NO2A-NT-20.3 is an agonistic ligand for NTSR1, where NT-20.3 refers to neurotensin (6-13) with N-methylation at Arg(8), Tle substitution for Ile(12) and conjugation to NO2A chelator at Lys (6), which has improved *in vivo* metabolic stability [115]. Although there exists better targeting vectors than NT-20.3 for NTSR1, other NTSR1 agonists potentially require specialized techniques to synthesize [122]. Alternatively, NTSR1 antagonists have improved metabolic stability over currently available NTSR1 agonists [123]. The enhanced pharmacokinetics have led to better treatment outcomes in mice [124] with some success in treating metastatic pancreatic adenocarcinoma [125]. NTSR1 antagonists, such as SR142948A, have greater tumor uptake *in vivo* but internalization rates and subcellular localization of internalized NTSR1 antagonists remain unclear. If NTSR1 antagonists do not accumulate in radiation-sensitive compartments of the cell and/or if the internalization rate is too low, then they may not lead to enhanced therapeutic efficacy for LEE-emitting radionuclides. Nevertheless, improvements in tumor uptake due to increased metabolic stability *in vivo* may enhance anti-tumoral effects. Thus, both NTSR1 agonist and antagonist are investigated for $^{55/58m}$Co RPT to provide additional information for the nuclear medicine community. *In vitro* results suggest that the better internalizing NTSR1 agonist radiolabeled with ^{58m}Co is more cytotoxic than its NTSR1 antagonist counterpart, but neither compound demonstrated meaningful therapeutic outcomes *in vivo* likely due to low tumor uptake.

Chapter 2. Separation of cyclotron-produced cobalt-55/58m from iron targets using cation exchange chromatography with non-aqueous solvents and extraction chromatography

Disclaimer: this chapter was published in Applied Radiation and Isotopes in collaboration with the Cyclotron research group at the University of Wisconsin-Madison. All collaborators participated in editing the manuscript in some way, shape or form.

Existing methods to separate cyclotron-produced $^{55/58m}$Co from isotopically enriched Fe targets use anion exchange chromatography to retain the bulk Fe [87,92,94] but because resin mass must be scaled proportionally with Fe to prevent overcapacity, these methods require larger elution volumes due to increased resin volume. Although Thisgaard et al. [87] completed the anion exchange separation process in 35 min, they only irradiated 7.0 mg/cm^2 Fe (about 5.5 mg for a 1 cm diameter target) and did not consider Mn contaminants since they did not observe Mn radionuclides. In contrast, Valdovinos et al. [92] completed the anion exchange separation process in 2 h using larger targets (>20 mg). For both methods, the large elution volume (~8-10 mL) significantly increased the total separation time due to evaporation and further processing.

Separating Co–Fe through anion exchange is possible due to the differences in anionic Fe (III) chloride speciation over Co (II) under different chemical environments [126,127]. Cation exchange systems can also exploit this difference in chloride speciation, where non-aqueous media, especially acetone, can further separate Co and Fe species [99,100,128]. In contrast to anion exchange methods, Co is retained on the cation exchange resin and Fe remains in the solution. The trace quantities of $^{55/58m}$Co produced for most applications (37 GBq of ^{55}Co and ^{58m}Co is equivalent to 308 and 168 ng, respectively, assuming no prior contamination of Co) avoids resin overcapacity, which can significantly reduce resin mass and elution volume. Reducing the elution volume will facilitate further processing to improve radiochemical and radionuclidic purities. Thus, the purpose of this chapter is to present an alternative separation procedure using cation exchange chromatography and extraction chromatography that can achieve high radionuclidic and radiochemical purities, low product volume, and reduce processing time for cyclotron-produced $^{55/58m}$Co from $^{54/57}$Fe targets.

2.1 Materials and methods

2.1.1 AG® 50W-X8 and branched-DGA resin K_d measurements

Aqueous solutions were made from >18 MΩ-cm DI H_2O (Milli-Q® Ultrapure Water) and concentrated HCl (Fisher Chemical, Optima grade). All subsequent references to DI H_2O are >18 MΩ-cm H_2O. AG® 50W-X8 (100-200 mesh, Bio-Rad Laboratories) and N,N,N’,N’-tetra-2-ethylhexyldiglycolamide (branched-DGA, Eichrom Technologies) resin were purchased from commercial vendors and used without further modification and purification. Batch resin experiments were performed in triplicate using sealed 1.5 mL micro centrifuge tubes (VWR International, LLC). AG® 50W-X8 (204±4 mg) and branched-DGA (85±10 mg) were equilibrated with 3 mL of each respective HCl/HCl-acetone concentration prior to sample contact.

For example, if the sample was in a matrix of 8 M HCl for the batch resin experiment, the equilibration procedure consisted of first wetting the dry resin (weighed in the 1.5 mL vial) with 1 mL of 8 M HCl. Then, the vial was vortexed for 5 seconds to agitate the resin and allowed to sit for ~5 min to let the resin settle and equilibrate. This process was repeated once more prior to removing the supernatant. The entire process of wetting, agitating, and removing the solution from the resin was repeated twice. Care should be taken to ensure that minimal resin material is removed, and the resin should be as dry as possible (<50 µL) to reduce errors in computing K_d (depends on resin mass and volume). This can be achieved by using a pipette with a small tip diameter or filter. Tilting the vial horizontally and/or centrifuging the vial can also help remove excess liquid.

HCl-acetone solutions are reported as total concentration of HCl in the solution and %v/v of acetone (Spectrum Chemical, 99.98%). For reference, 0.25 M HCl/85% acetone refers to 2.5 mmol HCl and 8.5 mL acetone in 10 mL total volume. Samples were agitated at room temperature (~25°C) using an Eppendorf ThermoMixer®. Different timepoints verified equilibrium for AG® 50W-X8 (2, 18, 47 h) and branched-DGA (0.5, 1 h). Samples for AG® 50W-X8 batch resin experiments were prepared using 350 ppm $CoCl_2$, 100 ppm $CuCl_2$, 100 ppm $FeCl_3$ and 350 ppm $MnCl_2$ (Sigma-Aldrich for all salts, >99.99%) in 1 mL of solution. To simplify the dilution process, the resulting metal concentrations were obtained by first combining stocks of each metal in dilute HCl at much higher concentration (~50 g/L) then aliquoting into each respective solution matrix (<1 % added volume). Samples for branched-DGA batch resin experiments were prepared using 100 ppm $FeCl_3$ and various activities of $[^{64}Cu]CuCl_2$, $[^{55}Co]CoCl_2$ and $[^{52}Mn]MnCl_2$ in 1 mL of solution. $[^{64}Cu]CuCl_2$ [129] and $[^{52}Mn]MnCl_2$ [130] were produced and separated using previously published methods (trace metals from each aliquot of radioactive samples were <1 ppm). The chosen concentration of stable metals for these experiments were based on a compromise between increasing the detected signal and remaining below ~10% resin capacity.

2.1.2 AG® 50W-X8 dynamic elution experiment

The same resin masses (200 mg AG® 50W-X8 and 85 mg branched-DGA) used in batch resin experiments were packed into empty fritted 1 mL SPE cartridges (TrisKem International) and conditioned with 3 mL of loading solution (e.g., 0.3 M HCl/80% acetone) for dynamic elution experiments. All elution experiments used nominal flows of 1 mL/min (based on time taken to pump ~25 mL water). Prior to using isotopically enriched Fe targets, an AG® 50W-X8 column was vertically loaded from the top with 10 mL of 5 g/L $FeCl_3$ and various activities of $[^{64}Cu]CuCl_2$, $[^{55}Co]CoCl_2$ and $[^{52}Mn]MnCl_2$ at 0.3 M HCl/80% acetone and rinsed with 15 mL 0.3 M HCl/80% acetone then eluted with 1.5 mL 8 M HCl. Although K_d values can predict the elution profile during separation, it is considered good practice to perform dynamic elution experiments using natural material so that unexpected occurrences can be addressed without losing costly isotopically enriched material.

2.1.3 Iron-54/57 target preparation

Iron-54 (99.7% ^{54}Fe, 0.28% ^{56}Fe, 0.01% ^{57}Fe, 0.01% ^{58}Fe, ISOFLEX) and ^{57}Fe (0.6% ^{56}Fe, 96.1% ^{57}Fe, 3.3% ^{58}Fe, ISOFLEX) targets (9 mm diameter) were prepared by electrodeposition using saturated ammonium oxalate (Thermo Scientific) electrolyte (platinized titanium mesh anode, silver cathode). The electrolyte was buffered using saturated oxalic acid (Sigma-Aldrich)/HCl and/or ammonium hydroxide (Alfa Aesar) to pH 2-7 (adapted from [131,132]). Targets were electrodeposited by applying 3.8-4.3 V across the cell with initial current density 160 mA/cm^2 (see Appendix Figure D-3). The pH was adjusted periodically as the electrolyte depletes (checked ~1-2 h, more important in the latter parts of plating). Figure 2-1 shows a sample electroplated Fe target. Iron-54/57 targets were dissolved using 8 M HCl and 30% H_2O_2 (Sigma-Aldrich, Optima grade) at ~80°C. Since the amount of HCl and H_2O_2 used for dissolution varies depending on the amount of Fe, the exact quantities are elaborated in the discussion.

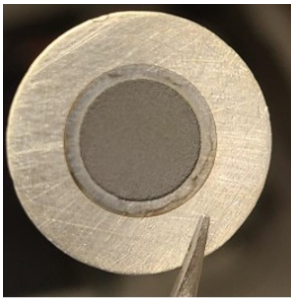

Figure 2-1 Electrodeposited ^{54}Fe target (9 mm diameter) on silver backing (19 mm diameter).

2.1.4 Cobalt-55/58m production from iron-54/57 and radiosynthesis

Deuteron irradiated (~35 µA, 8.2 MeV) ^{54}Fe (21-50 mg) and ^{57}Fe (60 mg) targets were processed using the same procedure (see Figure 2-3A. The radiochemistry module is shown in Appendix Figure D-4). Namely, after dissolution, loading and rinsing, the 8 M HCl eluate from AG® 50W-X8 was then vertically loaded from the top onto branched-DGA resin and rinsed with 5 mL 8 M HCl. Co was eluted using 4 M HCl, and 1 mL of the most activity concentrated fractions were dried down under light argon flow at 95°C (20-30 min, see Appendix Figure D-5) then reconstituted in 0.1 M HCl for radiolabeling with NOTA and DOTA. AMA for NOTA (1 h, 20°C) and DOTA (1 h, 85°C) were determined by titrating 3.7 MBq of ^{55}Co with each respective chelator (150 µL final volume), buffered with 0.5 M sodium acetate (Sigma-Aldrich) to pH 4.5. Samples were analyzed using radio-thin layer chromatography (silica gel 60 F_{254}; 50 mM EDTA mobile phase, Appendix Figure D-6). The ligand concentration in each sample for AMA measurements ranged from ~20 nM to ~20 µM (10 ng/mL to 10 µg/mL) for both NOTA and DOTA. Radio-sensitive phosphor screens were exposed to developed plates which were then read out with Cyclone Plus (PerkinElmer, see Appendix Figure D-7) and digitally processed using OptiQuant software. AMAs reported in this work correspond to unweighted arithmetic means and uncertainties correspond to one standard deviation about the mean (mean±SD). Cobalt-58m was directly radiolabeled to functionalized NOTA (NO2A-NT-20.3) at pH4.5 using sodium acetate buffer and 2 mg/mL sodium gentisate (Sigma-Aldrich, >99%) for 1 h at 95°C. Radiochemical purity was evaluated by radio-high-performance liquid chromatography (HPLC). Cobalt-58m was not titrated with NOTA/DOTA for AMA evaluations because irradiation parameters focused on providing activity for separate experiments. The load and first 3 mL rinse from AG® 50W-X8 were evaporated to less than 0.5 mL and then reconstituted in ammonium oxalate electrolyte for electrodeposition.

2.1.5 Sample analysis

Microwave-Plasma Atomic Emission Spectrometer (4200 MP-AES, Agilent Technologies) and Microwave Inductively Coupled Atmospheric Plasma Optical Emission Spectrometer (MICAP-OES 1000, Radom Corp. [133]) used certified standards to construct calibration curves. MP-AES/MICAP-OES analyzed the following metals: Cu (λ: 324.754 and 327.396 nm), Co (λ: 340.512, 345.350, and 350.228 nm), Fe (λ: 259.940 and 371.993 nm) and Mn (λ: 257.610 and 259.372 nm). Samples with acetone were evaporated fully under light Ar flow and reconstituted in 0.1 M HCl for MP-AES/MICAP-OES. High-purity germanium detector (HPGe, Canberra GC1519, FWHM at 1173 keV = 1.8 keV) quantified radioactive samples by gamma spectrometry.

K_d for each element was calculated according to:

$$K_d = \left(\frac{C_0}{C_A} - 1\right)\frac{V}{M} \tag{2.1}$$

Where C_0 is the initial concentration of the element in the sample, C_A is the concentration of the element in the aqueous phase, V is the volume of sample in milliliter (mL) and M is the dry resin mass in grams (g) [100,134,135]. K_d reported in this work was weighted by the inverse of the variance of each replicate and uncertainties correspond to standard error of the mean. The separation factor of Co-X is calculated as the fraction of Co in the sample divided by the fraction of X in the sample (i.e., %Co/%X), and radionuclidic and radiochemical purities are given as a percentage of activity. Unless otherwise stated, uncertainties correspond to one standard deviation about the mean. Residual $^{58m+g}$Co samples were assayed overnight and the 811 keV gamma emission was fit via the Bateman equation to quantify ^{58m}Co activities (see Figure 2-2) [94].

Alternatively, a real-time estimate of the ^{58m}Co activity may also be acquired from measuring the ^{58g}Co activity. In this method, the initial activity of ^{58g}Co at EOB is estimated by assaying the sample within 10 min of EOB (note: 1 h of decay would initially increase ^{58g}Co activity by ~3% assuming initial ^{58g}Co/^{58m}Co activity ratio is ~1%). Based on experience, the activity ratio of ^{58g}Co to ^{58m}Co is within 0.8-1.2% for irradiation times of 0.5-2 h for a ^{57}Fe target thick to 8 MeV deuterons. Thus, the initial ^{58m}Co activity can be estimated from this first assay, and all subsequent parameters of the Bateman equation can then be determined as a function of time. In this way, the radiochemical yield from separation, labeling, and/or purification can be determined by assaying ^{58g}Co in the sample and comparing to the theoretically expected value from the Bateman equation (i.e., the expected ^{58g}Co activity if the sample is allowed to decay without manipulation). An example spreadsheet is shown in Appendix Figure D-8. Since the major source of uncertainty (and error) derives from the initial estimate of the ratio of ^{58g}Co to ^{58m}Co, this method is reliable to estimate the ^{58m}Co activity in the sample to <20% deviation from the fit (much less if the saturation factor is taken into consideration to estimate the initial ^{58g}Co/^{58m}Co activity ratio rather than estimating a constant 1%. To be conservative in the estimated ^{58m}Co activity, one can also estimate a slightly higher initial ^{58g}Co/^{58m}Co activity ratio). Finally, the ^{58m}Co activity estimate can be corrected by performing the Bateman fit as previously discussed.

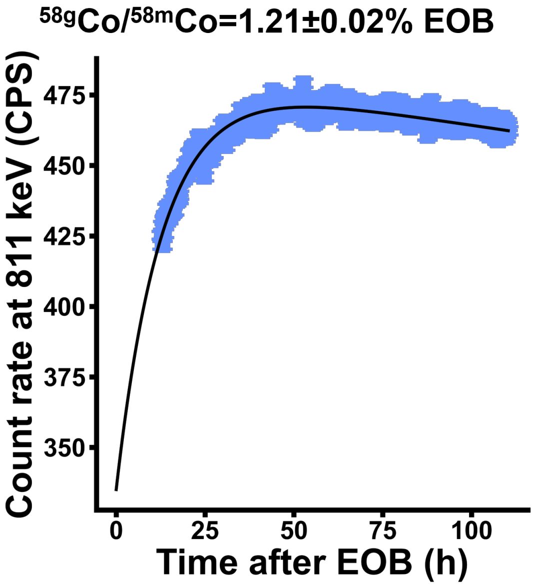

Figure 2-2 Residual $^{58m+g}$Co sample assayed by HPGe over time at a fixed position with fit corresponding to the Bateman equation (the half-lives of ^{58m}Co and ^{58g}Co were set as 9.1 h and 70.86 d, respectively). This sample was irradiated for 2 h at 35 µA but over a total period of about 3 h due to interruptions from clinical productions. The activity ratio of ^{58g}Co/^{58m}Co was about 1.2% for this sample. Only every second data point is plotted.

2.2 Results

2.2.1 Batch resin derived K_d

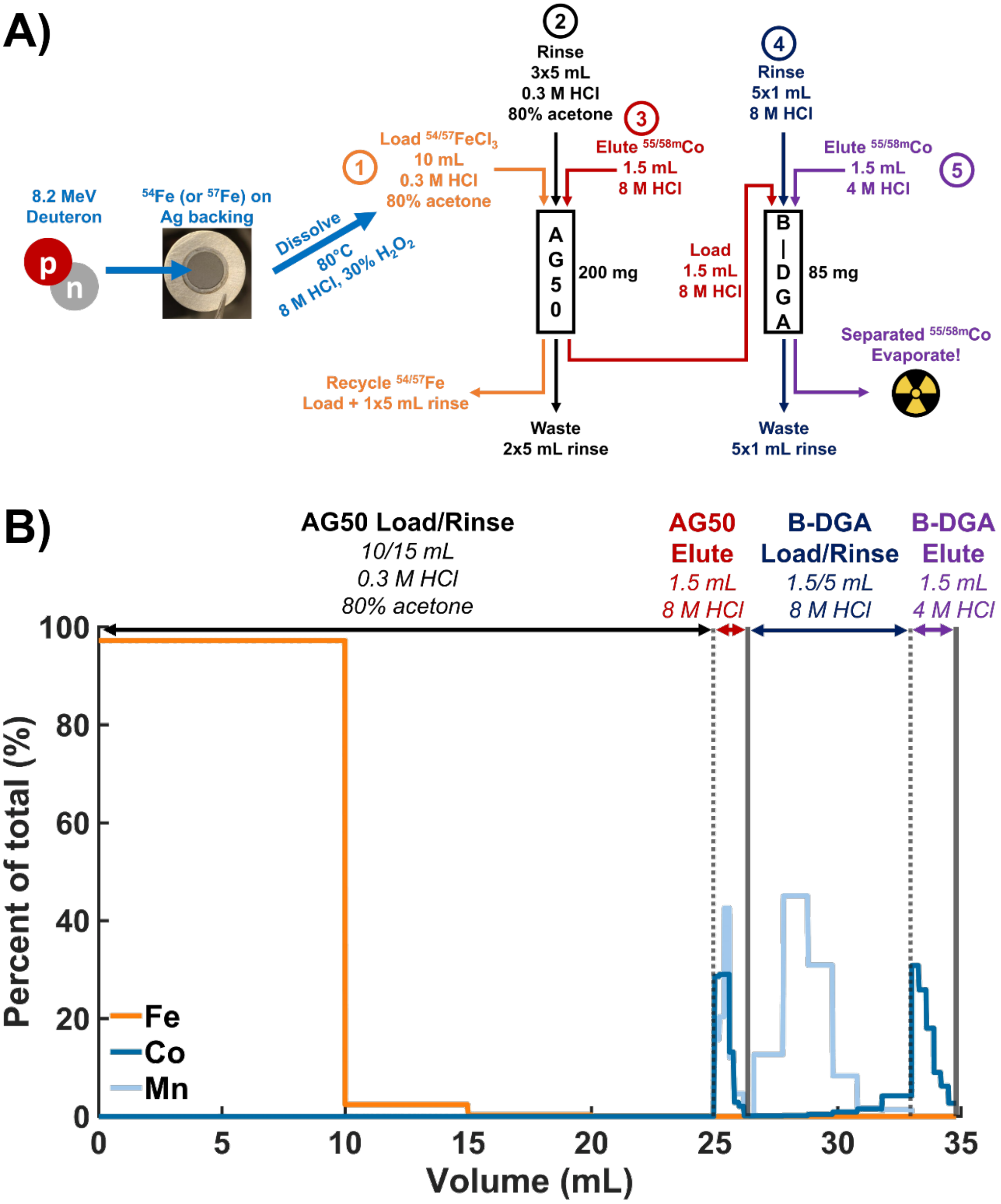

Figure 2-3 A) General separation procedure and (B) elution profile for an irradiated 46 mg ^{54}Fe target using AG® 50W-X8 (200 mg) and branched-DGA (85 mg). Fe was quantified by MICAP-OES and Co and Mn were quantified using ^{55}Co and ^{52}Mn tracers and HPGe spectrometry. The target was dissolved using 700 µL 8 M HCl and 300 µL 30% H_2O_2.

Measured K_d values from batch resin experiments are comparable with previously published (interpolated) results using similar resin (Figure 2-4A [100] and Figure 2-4B [134] for AG® 50W-X8 and branched-DGA, respectively). Although Cu should not be present, it was investigated because trace quantities will significantly reduce [$^{55/58m}$Co]Co-NOTA and -DOTA AMA. The K_d upper limit of quantification (3500 mL/g and 4300 mL/g for AG® 50W-X8 and branched-DGA, respectively) was determined by assessing the linearity and reproducibility of standards at 10-100 ppb for MP-AES/MICAP-OES. The K_d lower limit of quantification (1.2 mL/g) was determined from the standard deviation of identical sample measurements on each instrument (MP-AES/MICAP-OES/HPGe, <10% relative standard deviation). Tabulated values are presented in Table 2-1 and Table 2-2. Equilibrium for AG® 50W-X8 and branched-DGA was reached in 2 h and 1 h, respectively. K_d for AG® 50W-X8 at 7 and 8 M HCl for Mn, Cu, Co, and Fe were <1.2 mL/g.

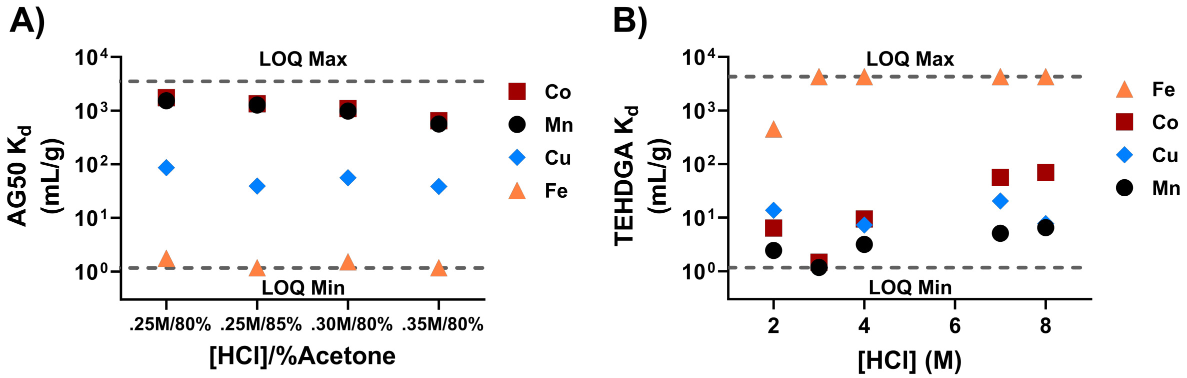

Figure 2-4 Measured K_d for A) AG® 50W-X8 and B) TEHDGA resin. The K_d upper and lower limit of quantification are denoted as LOQ Max and LOQ Min, respectively.

Table 2-1 AG® 50W-X8 K_d for selected elements in various mixtures of HCl-acetone.

	0.25 M 85% (mL/g)	**0.25 M 80% (mL/g)**	**0.30 M 80% (mL/g)**	**0.35 M 80% (mL/g)**	**7 M (mL/g)**	**8 M (mL/g)**
Cobalt	1.34±0.14 x10^3	1.73±0.10 x10^3	1.09±0.05 x10^3	646±19	<1.2	<1.2
Copper	39.1±2.9	86.1±6.5	55.9±4.1	38.4±0.2	<1.2	<1.2
Iron	<1.2	1.8±0.3	1.5±0.2	<1.2	<1.2	<1.2
Manganese	1.27±0.11 x10^3	1.53±0.09 x10^3	982±37	563±7	<1.2	<1.2

Table 2-2 Branched-DGA K_d for selected elements in various HCl concentration.

	2 M (mL/g)	**3 M (mL/g)**	**4 M (mL/g)**	**7 M (mL/g)**	**8 M (mL/g)**
Cobalt	6.4±0.4	1.5±0.1	9.5±0.5	56.5±2.1	69.5±3.6
Copper	13.7±1.3	<1.2	7.3±0.5	20.5±0.9	7.7±0.4
Iron	455±32	>4300	>4300	>4300	>4300
Manganese	2.4±0.2	<1.2	<1.2	5.1±0.2	6.5±0.3

2.2.2 Separation of $^{55/58m}$Co from $^{54/57}$Fe using AG® 50W-X8 and branched-DGA

The dissolution and AG® 50W-X8 separation process took 30-40 minutes with 97±3% (N=14) decay-corrected Co yield and Co-Fe separation factor >10^5. The branched-DGA separation process took 15-20 minutes with 93±3% (N=14) decay-corrected Co yield and Co-Mn separation factor >10^3. The final ^{55}Co samples (N=6) had radionuclidic purities of 99.9970±0.0016% ^{55}Co, 0.0015±0.0002% ^{57}Co and 0.0015±0.0012% ^{52}Mn decay-corrected to end of bombardment (EOB). The ^{58m}Co sample had radioisotopic purities of 98.8% ^{58m}Co, 0.8% ^{58g}Co and 0.4% ^{57}Co decay-corrected to EOB. Including the time needed for evaporation, radiolabeling can be started in 1-1.5 h. A sample elution profile using a 46 mg ^{54}Fe target is given in Figure 2-3B, and the physical load and rinse fractions are shown in Figure 2-5. Fe recovery was >98% and $^{54/57}$Fe target recycling efficiency (N=15) was 94±3% after 6-7 h of electrodeposition. Residual Fe in the electrolyte can be recovered.

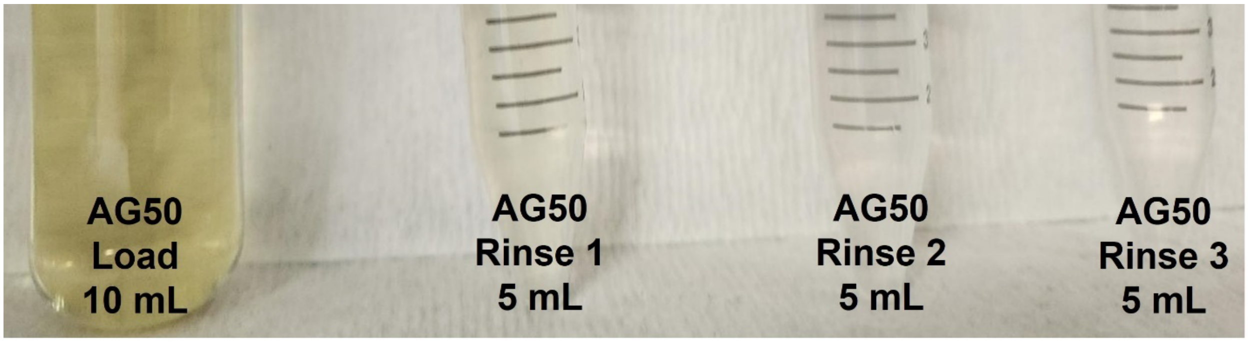

Figure 2-5 Collected load and rinse fractions from the AG® 50W-X8 separation process. 2, 20, 500 and 500 µL were taken from the load, rinse 1, 2 and 3, respectively, for analysis. The yellow-ish hue from $FeCl_3$ is not visible by eye in the second and third rinse fraction.

[^{55}Co]Co-NOTA and -DOTA AMA (N=6) were 89±48 MBq/nmol and 35±7 MBq/nmol, respectively, decay-corrected to EOB. ^{55}Co (Figure 2-6A) and ^{58m}Co (Figure 2-6B) physical yields from ^{54}Fe and ^{57}Fe targets, respectively, agree well with theoretically calculated yields after correcting for target beam intercept (correction factor 0.42). ^{58m}Co was quantitatively labeled at 50 MBq/nmol to NO2A-NT-20.3 (decay-corrected to EOB; >99% radiochemical purity, see Figure 2-7). ^{55}Co and ^{58m}Co activities used in this work were 160-290 MBq and 690 MBq at EOB, respectively.

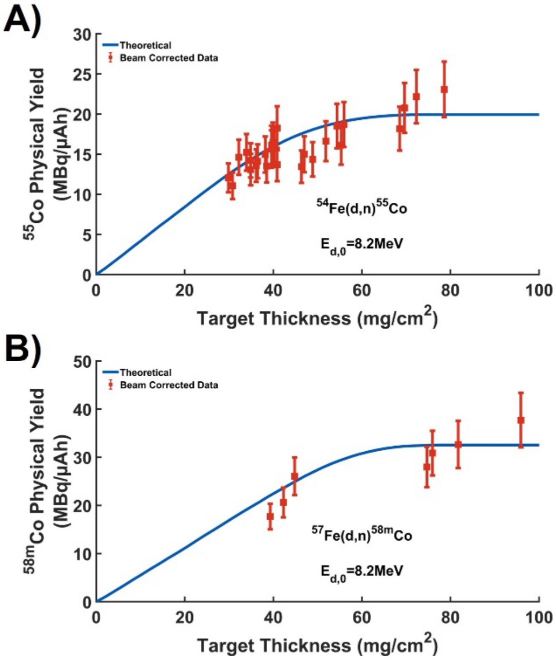

Figure 2-6 Measured and calculated physical yields for A) ^{55}Co (A) and B) ^{58m}Co. Cross sections were taken from [97] and stopping power was calculated using SRIM [48]. Not all targets presented in this figure were separated using the method proposed in this work.

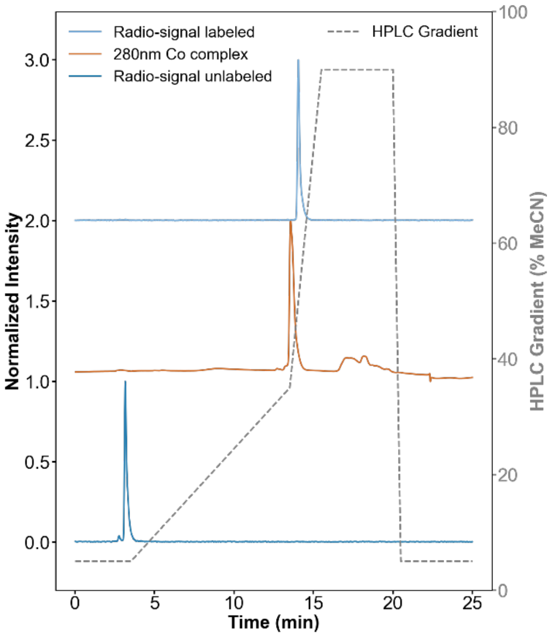

Figure 2-7 Sample radio-HPLC spectra of [^{55}Co]CoCl$_2$ (bottom) and ^{58m}Co labeled to NO2A-NT-20.3 (top). A reference HPLC spectrum for Co complexed with NO2A-NT-20.3 is also presented (middle). There is an approximate 0.3 min delay from the UV-Vis detector to the radiation detector.

2.3 Discussion

In comparison to previously published methods, the proposed cation exchange-extraction chromatography employed in this work can be 0.5-2 h faster and achieves one of the highest reported [^{55}Co]Co-NOTA and -DOTA AMA in literature with just 30 μAh of irradiation (see Table 2-3). NO2A-NT-20.3 was quantitatively labeled with ^{55}Co at 74 MBq/nmol at end of synthesis (0.5 h, 55°C, pH 4.5; 106 MBq/nmol decay-corrected to EOB) and used for separate experiments, corroborating measured [^{55}Co]Co-NOTA AMA. The sample loading condition (approximately 10 mL 0.3 M HCl/80%acetone, see further discussion in the proceeding paragraphs) was chosen based on evaluated K_d and low Co breakthrough from dynamic elution experiments. Although the ratio of K_d seems slightly more favorable at 0.25 M HCl/85% acetone, lower acetone concentration enables more flexible dissolution conditions for a fixed loading volume. If the eluted Mn and Co product from AG® 50W-X8 does not need further processing, the acidity can be reduced with 7 M ammonium chloride solution instead of 8 M HCl [136]. Eluting Co off the branched-DGA column with 4 M HCl resulted in better AMA, but more concentrated fractions may be obtained by eluting at lower HCl concentration. Recent experiments show that 400 μL 3.5 M HCl could elute >90% Co from the branched-DGA column without compromising AMA, which substantially reduces the evaporation time.

Table 2-3 Relevant parameters from different separation methods of cyclotron-produced-$^{55/58m}$Co from Fe targets. Unless otherwise stated, AMA is decay-corrected to EOB.

Method	Iron mass (mg)	Dissolution, separation, and evaporation time	Q (µAh)	AMA (MBq/nmol)
AG® 1-X8 and branched-DGA **(Valdovinos)**	24-79	3.7 h	^{55}Co: 44-120, ^{58m}Co: 90-124	NOTA: 27±18 [92] DOTA: 9±5 [92]
Dowex® 1X8 **(Thisgaard)**	3.2-5.5	1.3 to 2 h	18-108	DOTA-X*: 18-84 (EOS) [86,87,94,137] DOTA-X: >4 (EOS) [87]
AG® 50W-X8 and branched-DGA **(This work)**	21-60	1 to 1.5 h	^{55}Co: 28-32, ^{58m}Co: 50	NOTA: 89±48 DOTA: 35±7

*The authors used an additional Chromafix 30-PS-HCO3 cartridge. EOS refers to the end of synthesis.

From analyzing the K_d values reported by Strelow et al. [100] and this work, it is evident that an accurate mixture of HCl and acetone is critical for this proposed method. With 0.05 M HCl variation (from 0.25 to 0.30 M HCl at 80% acetone), the K_d for Co differed by almost a factor of 2, and a 10% difference in acetone (0.2 M HCl at 80% to 90%) changes the K_d by almost a factor of 20 [100]. Thus, the target dissolution process cannot remain the same for Fe targets with significantly different masses. As a simplified example, Fe is likely dissolved via oxidation by H$^+$ ions after adding HCl:

$$Fe(s)\ + 2H^{+} \rightarrow Fe^{2+} + (aq) + H_2(g) \tag{2.2}$$

Fe^{2+} can be further oxidized into Fe^{3+} from a variety of different mechanisms such as autooxidation and through the addition of oxidizing agents like H_2O_2 and/or O_2 [138]. Based on equation (2.2), there is a 2:1 consumption of H^+:Fe. Since K_d measurements used $FeCl_3$ in HCl-acetone mixtures, there is then a 3:1 consumption of Cl^-:Fe for solid iron targets, potentially resulting in an imbalance of [H^+] and [Cl^-] in the dissolved volume and loading fraction that diverges with larger Fe targets. Both [H^+] and [Cl^-] are important in the cation exchange process due to cationic competition and chemical speciation, respectively. However, since the oxidation of Fe^{2+} to Fe^{3+} primarily consumes excess H^+, this divergence may be negligible.

In this work, 500 µL 8 M HCl was adequate for 20-25 mg targets but 45-50 mg Fe targets required 700 µL 8 M HCl to achieve good separation under the same conditions (300 µL 30% H_2O_2, 8 mL acetone, total volume 10 mL in load. This can be unchanged for 20-60 mg Fe based on experience). Using the simplified model above and assuming consumption of H^+ for oxidizing Fe^{2+} to Fe^{3+}, the two loading conditions would correspond to 0.26 M HCl and 0.28 M HCl for 25 mg and 50 mg targets, respectively. Interestingly, no significant breakthrough was observed up to 0.35 M HCl for 60 mg Fe. However, more work is needed to ascertain the utility of this proposed method at >150 mg Fe for scaling up production. With careful consideration of the above, the proposed method is a promising alternative for separating cyclotron-produced $^{55/58m}Co$ from $^{54/57}Fe$ targets for preclinical research.

2.4 Conclusion

The proposed separation process for cyclotron-produced $^{55/58m}Co$ from $^{54/57}Fe$ targets can be completed in <1.5 h and recovers >88% Co with [^{55}Co]Co-NOTA and -DOTA

AMA 89±48 MBq/nmol and 35±7 MBq/nmol, respectively, decay-corrected to EOB. Cobalt-55 NOTA AMA reported in this work are >2x higher than previously published results after 30 µAh irradiations. Both ^{55}Co and ^{58m}Co were quantitatively labeled to functionalized NOTA for *in vivo* animal studies at 74 MBq/nmol and 37 MBq/nmol end of synthesis, respectively, validating measured AMA. Given similar Fe target masses and higher activities during synthesis, ^{58m}Co AMA should be even better than ^{55}Co, enabling a wide variety of *in vitro* and *in vivo* applications. Future work will transfer the proposed method to commercial radiochemistry synthesizers and automate the separation and radiolabeling processes.

Chapter 3. Radiolabeling diaminosarcophagine with cyclotron-produced cobalt-55 and [^{55}Co]Co-NT-Sarcage as a proof of concept in a murine xenograft model

Disclaimer: this chapter was published in Bioconjugate Chemistry in collaboration with Dr. German Oscar Fonseca Cabrera, Dr. Zibo Li and Dr. Zhanhong Wu from the University of North Carolina at Chapel Hill (UNC) and the Cyclotron research group at the University of Wisconsin-Madison. UNC synthesized the NT-Sarcage molecule. All collaborators participated in editing and contributing to the manuscript. Dr. Eszter Boros kindly provided the LC-MS instrument. Dr. Paul S. Donnelly provided great discussions regarding cobalt sarcophagine complexes. Justin Jeffery, Ashley Weichmann and Dr. Zachary Rosenkrans at the University of Wisconsin-Madison Carbone Cancer center assisted with animal experiments.

Although NOTA and DOTA conjugated radiopharmaceuticals are common, functionalized sarcophagine (Sar) compounds labeled with ^{64}Cu ($t_{1/2}$ = 12.70 h, $I_{\beta+}$ = 17%) have demonstrated improved *in vivo* pharmacokinetics, likely due to their high *in vivo* stability [108,109,139–144]. These promising results preclinical studies have led to several clinical trials, most of which employ ^{67}Cu ($t_{1/2}$ = 2.58 d, $E_{ave,\beta-}$ = 141 keV) for elementally matched theranostic radiopharmaceuticals (NCT04023331, NCT05633160, NCT04868604). Interestingly, despite Sar synthesis procedures typically beginning with cobalt-ethylenediamine complexation [89,105,107,145–148], there is no literature available for radiolabeling n.c.a. Co to uncoordinated Sar complexes. In comparison to NOTA and DOTA, Co-Sar stability (formation) constants have not been measured due to their high kinetic inertness [148], which makes Sar and Sar-derivatives interesting as stabilizers for Co. In fact, Co-Sar complexes even demonstrate stability against concentrated hydrochloric acid such that additional agents are required to fully degrade the complexes [105,106]. In addition to studies demonstrating the high *in vitro* and *in vivo* stability of Co-Sar derivatives [89,149] (albeit in large quantities), recent studies have also highlighted unique biological applications of Co-Sar derivatives *in vitro* [107] that suggest functionalized Sar compounds could potentially be developed into promising Co radiopharmaceuticals.

This chapter begins with an exploration of the labeling conditions for cyclotron-produced ^{55}Co with DiAmSar (DSar, a derivative of Sar), followed by *in vitro*/*in vivo* stability evaluation. Cobalt-55 is then radiolabeled to DSar functionalized with SR142948A [150] (NT-Sarcage, see Figure 3-1, which is a NTSR1 antagonist) to evaluate the stability and tumor targeting properties *in vivo* using a mouse xenograft tumor model. The biodistribution profile of [^{64}Cu]Cu-NT-Sarcage is also compared to [^{55}Co]Co-NT-Sarcage using the same tumor model to assess differences between the two elements given the current interest in ^{64}Cu-labeled Sar derivatives.

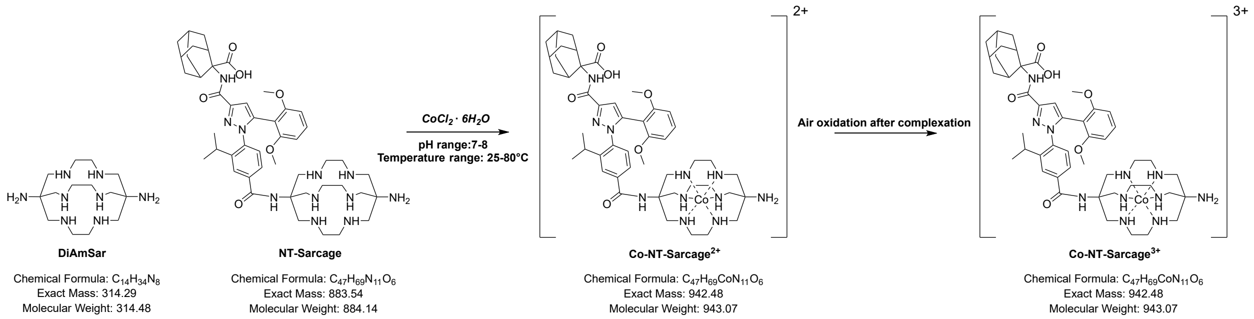

Figure 3-1 The chemical structures and relevant information for DiAmSar and NT-Sarcage used in this work. The pathway to Co-NT-Sarcage^{3+} likely begins with Co-NT-Sarcage^{2+} formation that then interacts with the oxygen content in the solution to oxidize Co.

3.1 Materials and methods

3.1.1 Cyclotron production and separation of ^{55}Co and ^{64}Cu

Cobalt-55 was produced and separated following methods from Chapter 2. The purified product was evaporated to dryness and reconstituted in 0.01 M HCl for radiolabeling. Copper-64 was acquired from weekly productions of ^{64}Cu by the UW-Madison cyclotron research group [129].

3.1.2 Radiolabeling

DiAmSar (DSar)

1,8-Diamino-3,6,10,13,16,19-hexaazabicyclo[6,6,6]-eicosane, or DiAmSar (DSar), was purchased from Macrocyclics and used without further purification to make stock solutions ranging from 10 µg/mL to 10^{-2} µg/mL in DI H_2O (same as Chapter 2 for future reference). Samples for [^{55}Co]Co-DSar AMA studies were incubated using 1.85 MBq ^{55}Co and analyzed using radio-thin layer chromatography (Supelco silica gel 60 F_{254}; 50 mM EDTA mobile phase) by fitting a sigmoidal curve to determine the 50% binding point. The AMA is defined as the activity divided by twice the 50% binding point (MBq/nmol) and values are decay corrected to end of synthesis (EOS). Radiosensitive phosphor screens were exposed to the radio-TLC plates as described in Chapter 2. An example developed radio-TLC plate can be seen in Figure 3-2A, where the sigmoidal fitting is presented in Figure 3-2B. These methods are akin to how [^{55}Co]Co-NOTA and -DOTA AMA were determined in Chapter 2. Reactions at pH=4.5 and 5.5 were set using 0.1 M sodium acetate buffer (Mallinckrodt Pharmaceuticals) and reactions at pH=7 and 8 were set using 0.1 M HEPES buffer (DOT Scientific Inc.). Radiolabeling experiments were performed in duplicate and results are computed by averaging and propagating uncertainties (1σ).

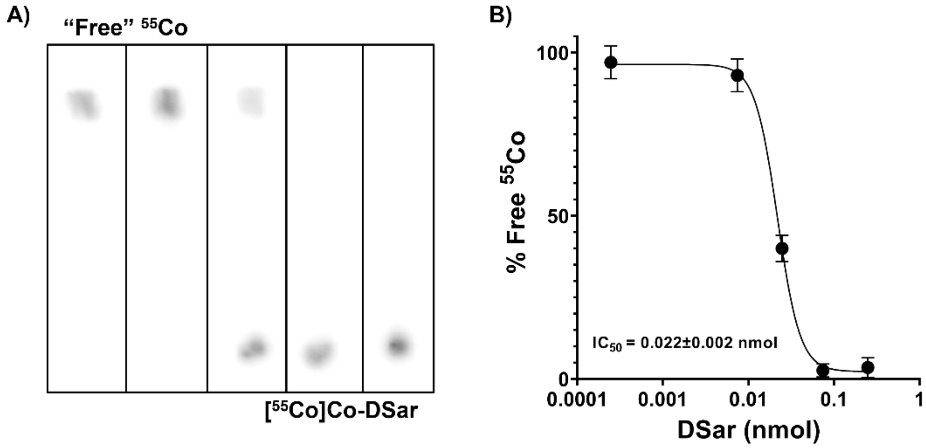

Figure 3-2 A) Sample radio-TLC plate developed with 50 mM EDTA mobile phase that was used to determine [^{55}Co]Co-DSar AMA. Each separate reaction had an increasing concentration of DSar ligand from left to right, where the leftmost reaction had no DSar addition to serve as the control. [^{55}Co]Co-DSar is positioned near the baseline whereas unbound ^{55}Co moves with the solvent front. Radio-TLC plates used for stability analyses are like the above. B) Sigmoid fit used to determine the 50% binding of [^{55}Co]Co-DSar. The concentration of the control was set at 0.2 pmol to aid visualization.

NT-Sarcage

NT-Sarcage was synthesized at the University of North Carolina at Chapel Hill according to methods by Cabrera et al. [144]. Co-NT-Sarcage was synthesized by adding 1.5x molar excess $CoCl_2$ to NT-Sarcage (pH=8, 0.5 h, 25°C, 100 nmol) and used for HPLC/liquid chromatography-mass spectrometry (LC-MS) analysis. NT-Sarcage was radiolabeled with ^{55}Co (pH=8, 2.5 h, 85°C, 2 mg/mL sodium gentisate) at 37 MBq/nmol and ^{64}Cu (pH=4.5, 0.5 h, 25°C) at 18.5 MBq/nmol. The reason for radiolabeling ^{55}Co at these conditions was to maximize the AMA since the compound starts to degrade at 80°C regardless of ligand concentration. Radiolabeled compounds were purified by HLB (30 mg. Briefly, direct loading via 1 mL syringe, then rinsed with 1 mL 10% ethanol in DI H_2O and eluted using 1 mL ethanol with ~0.1% trifluoroacetic acid, TFA), then dried under argon before reconstitution in PBS to <10% ethanol. Radioanalytical-HPLC determined radiochemical purity of labeled compounds by peak area (C18 reverse-phase 250 x 4.60 mm 5μm 100Å DIONEX column and the following gradient: 0-2 min

95% A, 5% B; 2-22 min 95-5% A, 5-95% B; 22-25 min 5% A, 95% B; 25-25.5 min 5-95% A, 95-5% B; and 95% A, 5% B until 30 min. A=0.1% TFA in H_2O, B=acetonitrile).

3.1.3 *In vitro* stability analysis

DSar quantitatively radiolabeled with ^{55}Co at pH=7 and 80°C for 1 h (75 pmol DSar, 1.85 MBq ^{55}Co) was aliquoted into pH=7.4 phosphate buffered saline (PBS, Fisher Scientific), human serum (Jackson ImmunoResearch), and 50 mM EDTA for *in vitro* stability analysis. Radiolabeled [^{55}Co]Co-DSar was diluted 5x using PBS before adding to human serum in the concentration recommended by the manufacturer. The 50 mM EDTA reaction was adjusted to pH=7 by adding 0.5 M pH=7 HEPES buffer (final concentration was 50 mM EDTA. Used ~100 mM EDTA stock at pH ~7 then added ^{55}Co and more HEPES buffer). Samples with human serum were incubated at 37°C then mixed 1:1 with acetonitrile (MeCN, Sigma-Aldrich) and centrifuged to remove excess protein prior to spotting on TLC plates. An empirical background threshold determined the 100% baseline for stability studies (e.g., >93% raw signal may be considered as 100% given previous experience). Unless otherwise noted, results are reported as mean$\pm\sigma$, where the uncertainty comes from reading the radio-TLC plates.

3.1.4 Animal models

All animal studies were conducted under a protocol approved by the University of Wisconsin Institutional Animal Care and Use Committee. Female athymic nude mice (5-6 weeks old) were purchased from Jackson Laboratory. HT29 human colorectal adenocarcinoma cells (American Type Culture Collection, ATCC) were cultured in McCoy's 5A medium and Eagle's Minimum Essential Medium, with 10% fetal bovine serum (FBS) and 1% penicillin-streptomycin (Pen-Strep, Gibco) at 37°C in a 5% CO_2

atmosphere using T75 flasks. Cells were resuspended using 0.25 % TrypsinEDTA (Gibco) and counted using a hemocytometer (Fisher Scientific) via an optical microscope (Nikon Diaphot 300). HT29 tumors were established by subcutaneous injection of approximately 10^6 cells suspended in 100µL of 1:1 PBS and Matrigel (Corning) into the right axillary. The xenograft location was chosen to distinguish tumor uptake from kidneys and bladder. *In vivo* pharmacokinetics was determined with PET imaging (Inveon µPET/CT, Siemens), and PET Images were reconstructed using 3D ordered subset expectation maximization (OSEM) [151], with 80M counts for timepoints before 4 h and 40M counts thereafter. Mice were anesthetized with 2.5% isoflurane in oxygen during each scan. Regions of interest (ROI) were created from both CT contours and thresholding PET uptake values. *In vivo* experiments were performed once tumor diameters reached ~5 mm (1 week). Uptake is expressed as the average percent of decay-corrected injected activity per gram of tissue and abbreviated as %ID/g. The choice for using %ID/g rather than %IA/g is to correspond better with literature nomenclature, though %IA/g may be more fitting. Each mouse received either 3.7 MBq of [^{55}Co]CoCl$_2$ (N=4, in PBS with dilute HEPES buffer to pH~7), 3.7 MBq of [^{55}Co]Co-DSar (1 nmol Sar each, N=4), 1.85 MBq of [^{55}Co]Co-NT-Sarcage (N=2) or 1.85 MBq of [^{64}Cu]Cu-NT-Sarcage (N=2) via tail vein injection. PET imaging acquired pharmacokinetic profiles at 1 and 4 h for [^{55}Co]Co-DSar and 1, 4, 9, 24 h p.i. for radiolabeled NT-Sarcage molecules. The mice receiving [^{55}Co]CoCl$_2$ were imaged at 1 and 4 h to compare with [^{55}Co]Co-DSar and later timepoints to corroborate previously published results [93]. *Ex vivo* biodistribution studies were performed immediately after the last PET imaging timepoint to validate *in vivo* PET imaging results with recovery coefficients (Appendix Figure D-9). Blood, HT29 tumor and all major organs were collected and weighed. The stomach, small intestines and large intestines were emptied prior to assaying. Unless otherwise noted, uptake values are reported as mean±SD.

3.2 Results

3.2.1 Radiolabeling and stability of [^{55}Co]Co-DSar

The radiolabeling pH range investigated in this work considered the protonation constants of DSar [106,152] and was chosen to avoid hydrolysis of ^{55}Co. The 50 mM EDTA mobile phase used in radio-TLC analysis was able to discriminate [^{55}Co]CoCl$_2$ from [^{55}Co]Co-DSar with high resolution (Figure 3-2A). A general trend demonstrating improved [^{55}Co]Co-DSar AMA with increased pH, temperature and time is shown in Figure 3-3A. The optimal radiolabeling pH was pH8, where [^{55}Co]Co-DSar AMA at 37°C and 80°C were 8±2 and 45±9 MBq/nmol after 4 h of reaction, respectively.

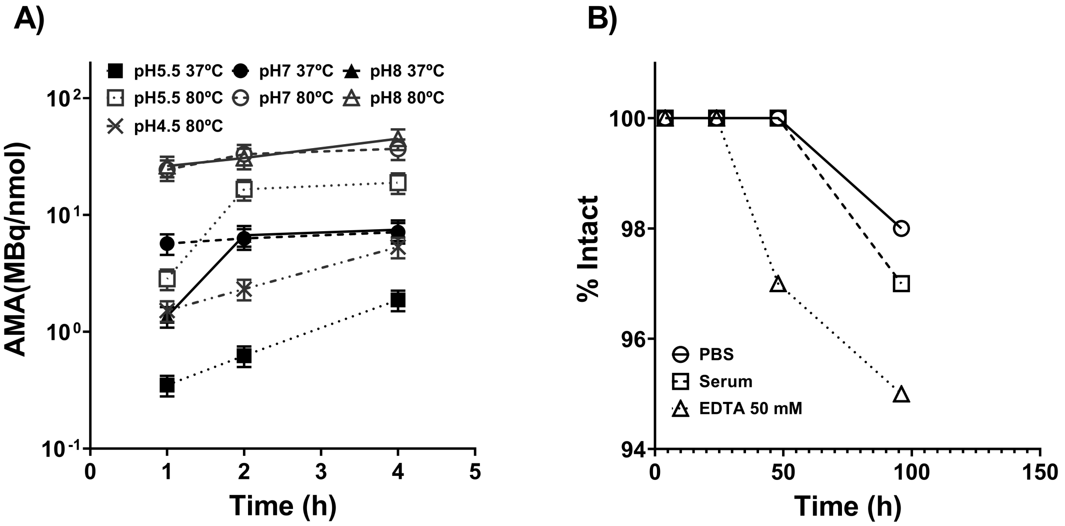

Figure 3-3 A) The impact of pH, temperature, and time on [^{55}Co]Co-DSar AMA. The AMA improves at higher temperature and pH in the range investigated. Radiolabeling at pH=4.5 and 37°C had an AMA below 0.3 MBq/nmol even after 4 h, so it is not included. B) Stability of radiolabeled [^{55}Co]Co-DSar in PBS, human serum, and 50 mM EDTA was ≥95% up to 96 h. Error bars of ±5% were removed to enhance readability.

After determining radiolabeling conditions, [^{55}Co]Co-DSar was incubated with human serum at 37°C and 50 mM EDTA to assess its stability *in vitro* at pH7. The [^{55}Co]Co-DSar complex was stable (≥95% intact) up to 96 h even with >5x10^{4} excess of EDTA to DSar, which corroborates the kinetic inertness and stability of Co-DSar complexes (Figure 3-3B). The relative uncertainty in the method used to determine stability is about 5%, so the slight deviation from the baseline may be due to random fluctuations, though there appears to be a systematic trend. Nevertheless, these results demonstrate the inertness of [^{55}Co]Co-DSar at nanomolar concentrations. Cobalt-55 was radiolabeled to NT-Sarcage in sodium gentisate solution with radiochemical purities of 62% and 87% after labeling and purification, respectively, based on peak areas from analytical radio-HPLC (Figure 3-4). LC-MS analysis of Co-NT-Sarcage suggests that the complex likely stabilizes Co^{3+} (Figure 3-5). [^{64}Cu]Cu-NT-Sarcage was quantitatively radiolabeled at half the AMA of [^{55}Co]Co-NT-Sarcage and with >95% radiochemical purity after purification. The residual contaminant at the solvent front after purification is likely due to degradation during the evaporation process.

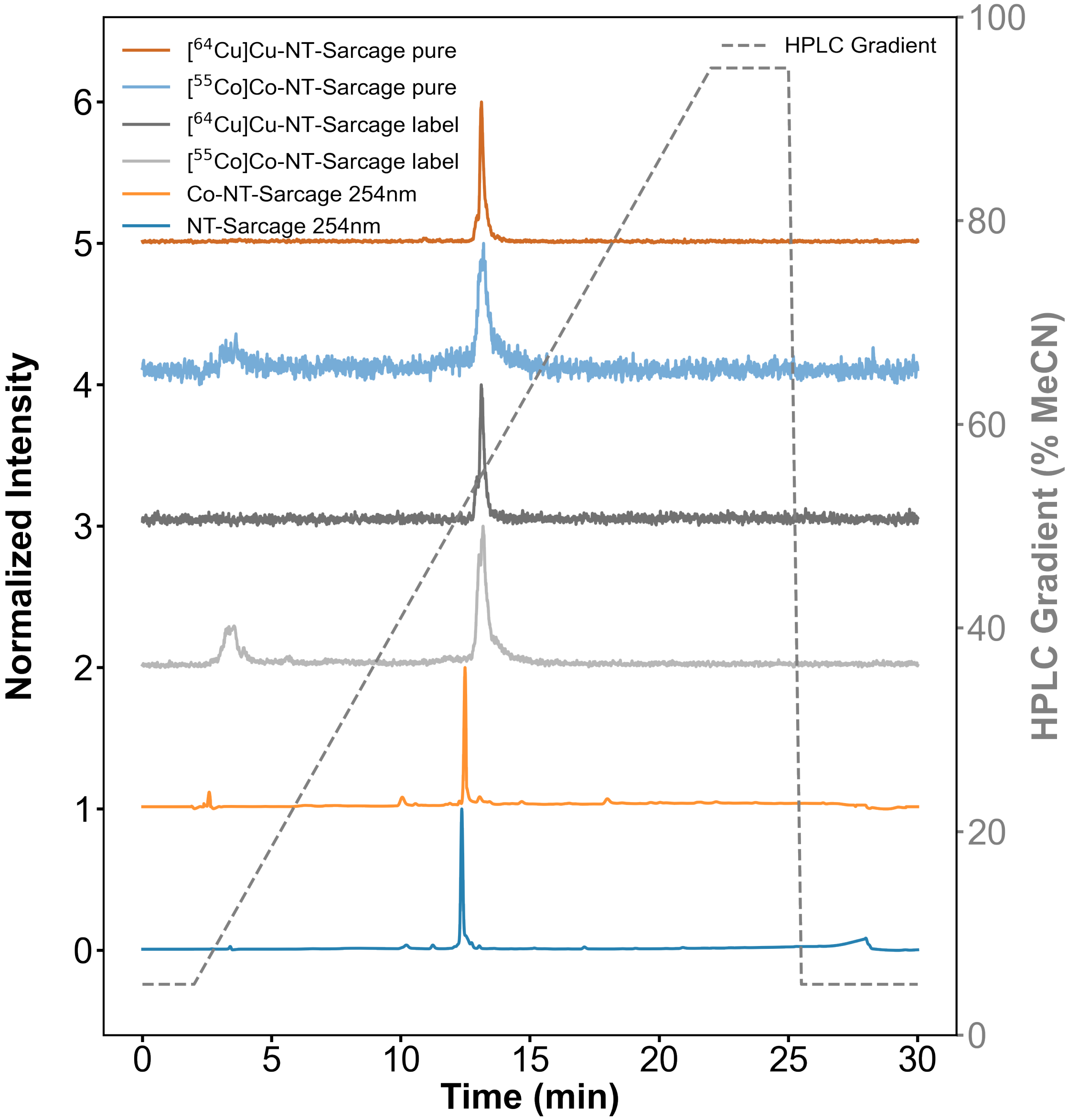

Figure 3-4 HPLC chromatograms of the stock NT-Sarcage ligand and Co-NT-Sarcage analyzed at 254nm. The Co-NT-Sarcage peak was enhanced for visibility to better assess the retention time. Radio-HPLC chromatograms of [^{55}Co]Co-NT-Sarcage and [^{64}Cu]Cu-NT-Sarcage before and after purification are also presented in this figure. There is a 0.3-0.4 min delay between the UV signal and the radio-signal. The HPLC gradient used 0.1% TFA DI H_2O as the aqueous phase.

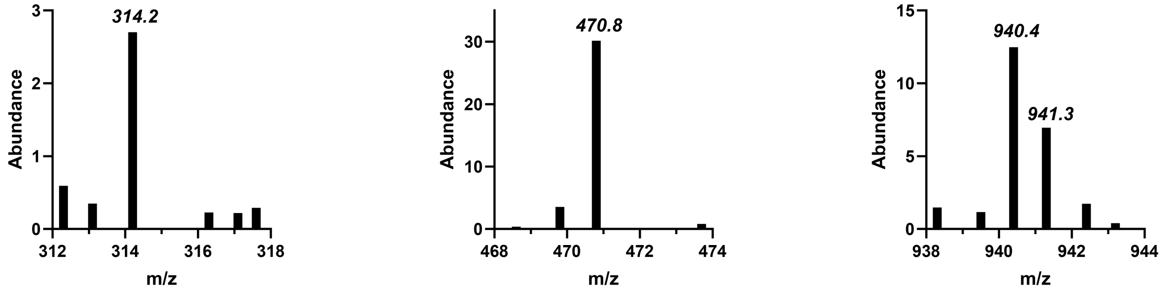

Figure 3-5 MS from LC-MS analysis of the Co-NT-Sarcage complex. The exact mass for Co-NT-Sarcage is 942.54, resulting in m/z of 314.18 for Co(III) (detected 314.2). The expected m/z for $[M - H]^{2+}$ and $[M - 2H]^{+}$ are 470.77 and 940.54, respectively (detected 470.8 and 940.4). LC-MS was performed by using an Agilent 1100 Series apparatus with an LC/MSD trap and Daly conversion dynode detector with UV detection at 220 and 254 nm (column: Phenomenex Luna, C18(2) 150x3 mm). Gradient of A (0.01 % formic acid in water) to 95 % B (0.01 % formic acid in MeCN), flow rate 0.8 mL min 0–3 min: 5 % B, 3–10 min: 5–95 % B, 10–13 min: 95 % B, 13–13.5 min: 95–5 % B, 13.5–16 min: 5 % B.

3.2.2 In vivo pharmacokinetics of [^{55}Co]Co-DSar and [^{55}Co]CoCl$_2$

Mice were administered [^{55}Co]Co-DSar and imaged at 1 and 4 h post injection (p.i.) to evaluate the pharmacokinetics of the compound. Another set of mice was administered [^{55}Co]CoCl$_2$ for comparison. Maximum intensity projection (MIP) PET/CT images at 1 and 4 h p.i. are in Figure 3-6A and Figure 3-6B for [^{55}Co]Co-DSar and [^{55}Co]CoCl$_2$, respectively. Organ uptake values derived from PET ROI quantification are shown in Figure 3-7 for both [^{55}Co]Co-DSar and [^{55}Co]CoCl$_2$. Based on the images and the organ uptake values, the pharmacokinetics of [^{55}Co]Co-DSar differ from [^{55}Co]CoCl$_2$, where [^{55}Co]Co-DSar appears to target a broad range of cartilaginous tissue and is removed from the blood pool at a faster rate compared to [^{55}Co]CoCl$_2$. The biodistribution of [^{55}Co]CoCl$_2$ from this work corroborates previously published results [93]. Tabulated organ uptake values are provided in Table 3-1 and Table 3-2.

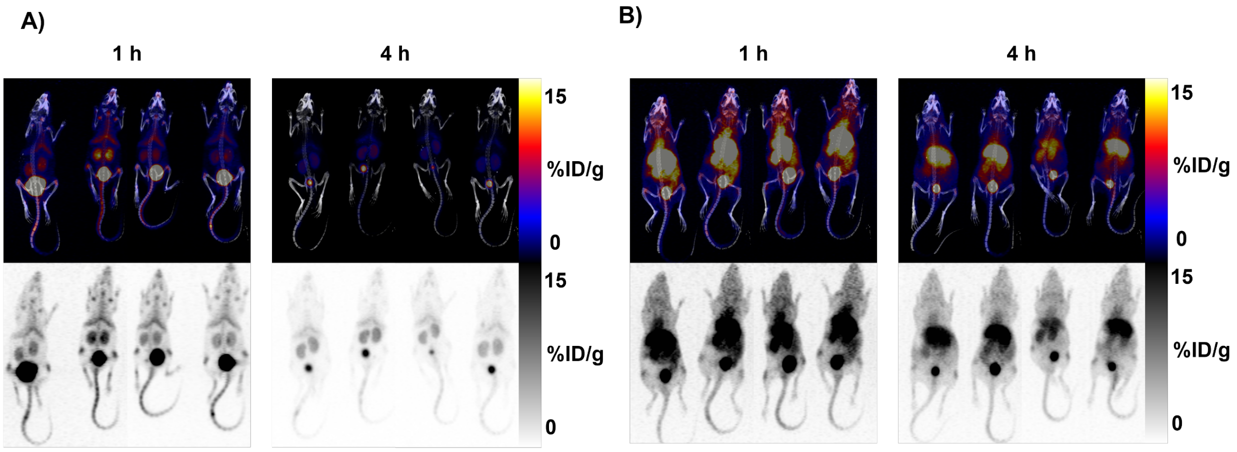

Figure 3-6 MIP PET/CT images at 1 and 4 h p.i. of (A) [^{55}Co]Co-DSar and (B) [^{55}Co]CoCl$_2$. Greyscale PET MIP images are also presented below the PET/CT images.

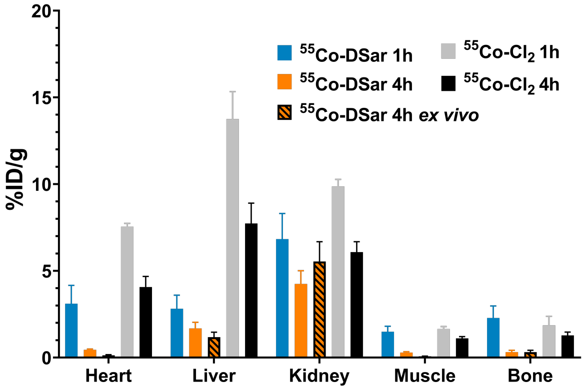

Figure 3-7 Organ uptake values in %ID/g at 1 and 4 h p.i. derived from in vivo PET ROI quantification for [^{55}Co]Co-DSar and [^{55}Co]CoCl$_2$. Ex vivo biodistribution at 4 h for [^{55}Co]Co-DSar is also presented for completeness.

Table 3-1 Tabulated organ uptake values in %ID/g derived from in vivo PET imaging for [^{55}Co]Co-DSar and [^{55}Co]CoCl$_2$.

	[^{55}Co]Co-DSar		[^{55}Co]CoCl$_2$			
Organ	1h	4h	1h	4h	24h	48h
Heart	3.1±1.1	0.4±0.1	7.6±0.2	4.1±0.6	1.5±0.3	1.1±0.2
Liver	2.8±0.8	1.7±0.4	13.8±1.6	7.7±1.2	4.7±0.9	3.3±0.5
Kidney	6.8±1.5	4.2±0.8	9.9±0.4	6.1±0.6	5.0±0.7	2.2±0.3
Muscle	1.5±0.3	0.3±0.1	1.7±0.1	1.1±0.1	0.6±0.3	0.3±0.1
Bone	2.3±0.7	0.3±0.1	1.9±0.5	1.3±0.2	0.9±0.2	0.5±0.1

Table 3-2 Tabulated organ uptake values in %ID/g derived from ex vivo biodistribution for [^{55}Co]Co-DSar and [^{55}Co]CoCl$_2$.

	[^{55}Co]Co-DSar	[^{55}Co]CoCl$_2$
Organ	4h	48h
Blood	0.07±0.01	0.39±0.06
Skin	0.43±0.09	1.1±0.1
Muscle	0.07±0.01	0.19±0.10
Bone	0.31±0.11	0.52±0.25
Heart	0.13±0.04	1.8±0.2
Lung	0.83±0.72	1.2±0.1
Liver	1.2±0.3	3.1±0.5
Kidney	5.5±1.1	2.4±0.3
Spleen	0.30±0.06	0.43±0.10
Pancreas	0.08±0.04	0.87±0.09
Stomach	0.13±0.03	0.49±0.07
Intestine	0.14±0.02	0.42±0.07
Tail	0.69±0.07	0.36±0.09
Brain	0.03±0.01	0.18±0.10

3.2.3 In vivo pharmacokinetics of [^{55}Co]Co-NT-Sarcage and [^{64}Cu]Cu-NT-Sarcage

Since [^{55}Co]Co-DSar demonstrated different pharmacokinetics compared to [^{55}Co]CoCl$_2$, radiolabeled [^{55}Co]Co-NT-Sarcage was administered in mice as a proof of concept for targeting cancer cells *in vivo*. MIP PET/CT images of [^{55}Co]Co-NT-Sarcage were obtained at 1, 4, 9 and 24 h p.i. (Figure 3-8A). [^{55}Co]Co-NT-Sarcage shows uptake mainly in the HT29 tumor with a mixed clearance route between hepatobiliary and renal. The lack of prominent [^{55}Co]Co-NT-Sarcage uptake in cartilaginous tissues and longer blood circulation compared to [^{55}Co]Co-DSar suggests [^{55}Co]Co-NT-Sarcage retained the targeting properties of SR142948A. [^{64}Cu]Cu-NT-Sarcage was administered in mice with the same type of tumor model to assess potential differences between ^{55}Co- and ^{64}Cu-Sarcage (radio)pharmaceuticals (Figure 3-8B). Interestingly, [^{55}Co]Co-NT-Sarcage exhibited faster initial clearance from the blood and ~2x better tumor-to-liver ratio at 24 h p.i. compared to [^{64}Cu]Cu-NT-Sarcage. The overall biodistribution profile is similar for both radionuclides in this work and from another study using a different tumor model [144]. The corresponding PET ROI quantified organ uptake values for [^{55}Co]Co-NT-Sarcage and [^{64}Cu]Cu-NT-Sarcage are given in Figure 3-9 and Figure 3-10, respectively. Tabulated organ uptake values in %ID/g derived from *ex vivo* biodistribution for [^{55}Co]Co-NT-Sarcage and [^{64}Cu]Cu-NT-Sarcage are presented in Table 3-3 and Table 3-4, respectively.

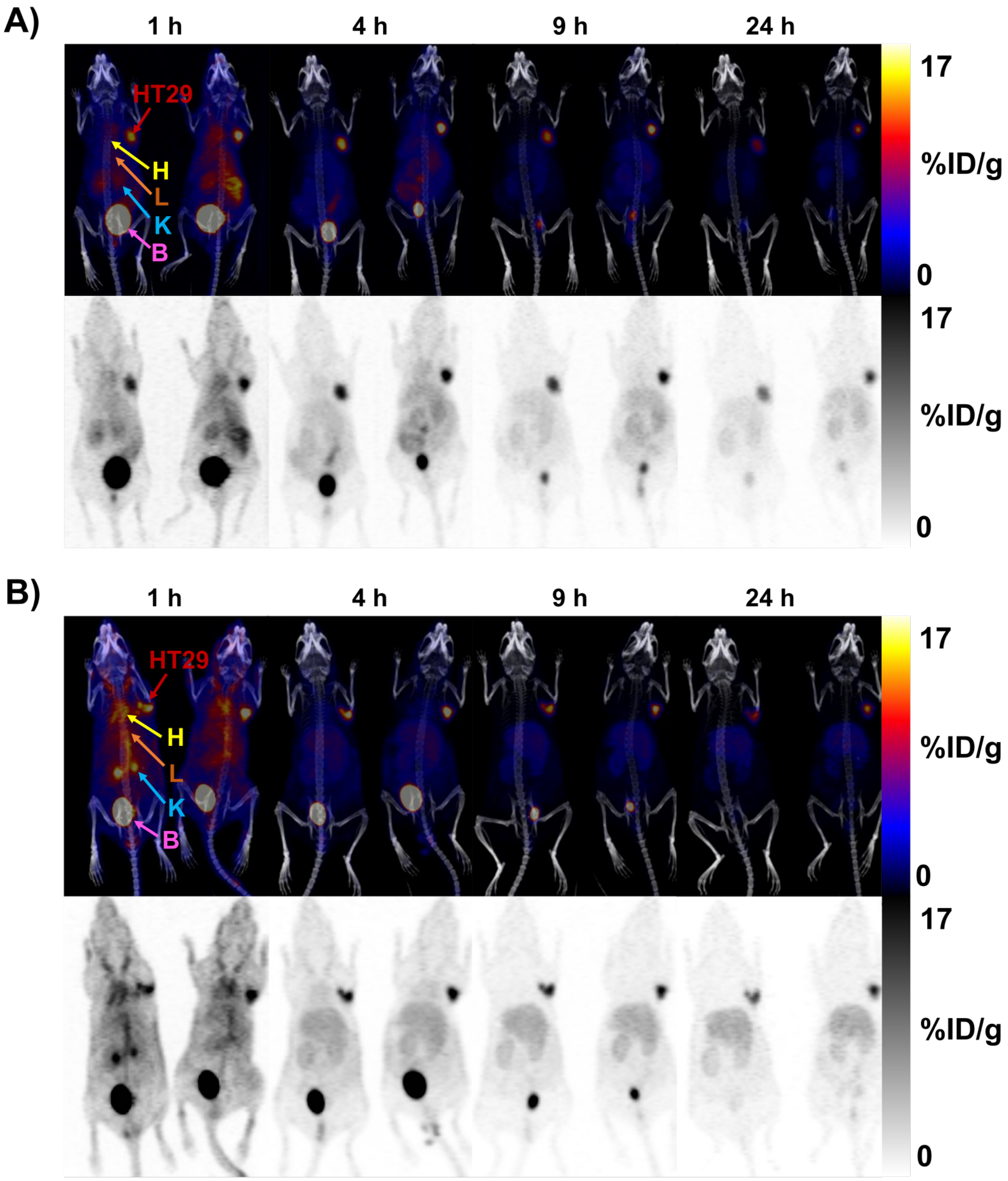

Figure 3-8 MIP PET/CT images at 1, 4, 9 and 24 h p.i. of A) [^{55}Co]Co-NT-Sarcage and B) [^{64}Cu]Cu-NT-Sarcage (HT29: HT29 tumor, H: heart, L: liver, K: kidney, B: bladder). Greyscale PET MIP images are also presented below the PET/CT images.

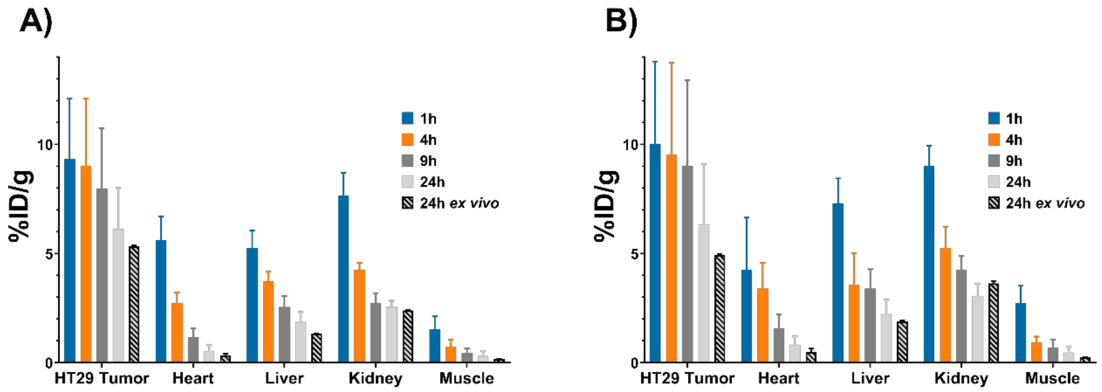

Figure 3-9 [^{55}Co]Co-NT-Sarcage organ uptake values in %ID/g at 1, 4, 9 and 24 h p.i. derived from in vivo PET ROI quantification and ex vivo biodistribution at 24 h p.i. for (A) mouse 1 and (B) mouse 2. Error bars correspond to uncertainty in counting statistics propagated by the OSEM3D image reconstruction software.

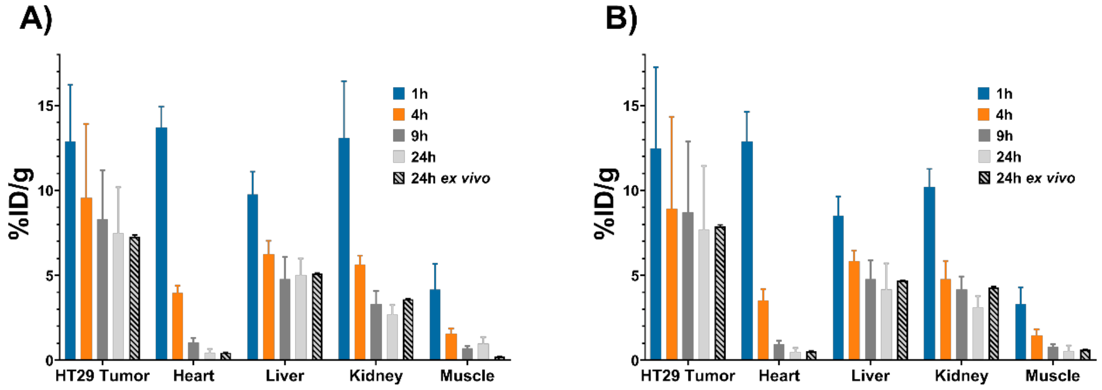

Figure 3-10 [^{64}Cu]Cu-NT-Sarcage organ uptake values in %ID/g at 1, 4, 9 and 24 h p.i. derived from in vivo PET ROI quantification and ex vivo biodistribution at 24 h p.i. for (A) mouse 1 and (B) mouse 2. Error bars correspond to uncertainty in counting statistics propagated by the OSEM3D image reconstruction software.

Table 3-3 Tabulated organ uptake values in %ID/g derived from ex vivo biodistribution for [^{55}Co]Co-NT-Sarcage. Reported uncertainty values correspond to uncertainties in counting statistics and the scale.

	[^{55}Co]Co-NT-Sarcage	
Organ	Mouse 1	Mouse 2
Blood	0.25±0.01	0.41±0.01
Skin	0.44±0.01	0.72±0.02
Muscle	0.18±0.01	0.25±0.01
Bone	0.17±0.01	0.36±0.02
Heart	0.32±0.01	0.50±0.01
Lung	0.56±0.01	0.58±0.01
Liver	1.33±0.01	1.89±0.01
Kidney	2.39±0.01	3.64±0.02
Spleen	0.47±0.01	0.60±0.01
Pancreas	0.25±0.01	0.33±0.01
Stomach	0.29±0.01	0.37±0.01
Intestine	0.82±0.01	0.98±0.01
Tail	0.19±0.01	0.33±0.01
Brain	0.024±0.003	0.038±0.002
HT29 Tumor	5.33±0.03	4.94±0.03

Table 3-4 Tabulated organ uptake values in %ID/g derived from ex vivo biodistribution for [^{64}Cu]Cu-NT-Sarcage. Reported uncertainty values correspond to uncertainties in counting statistics and the scale.

	[^{64}Cu]Cu-NT-Sarcage	
Organ	Mouse 1	Mouse 2
Blood	0.14±0.01	0.14±0.01
Skin	0.84±0.04	1.04±0.06
Muscle	0.20±0.01	0.62±0.02
Bone	0.44±0.02	0.42±0.01
Heart	0.44±0.02	0.54±0.02
Lung	1.48±0.04	1.41±0.03
Liver	5.11±0.03	4.68±0.02
Kidney	3.59±0.04	4.30±0.04
Spleen	1.44±0.04	1.42±0.04
Pancreas	0.40±0.01	0.45±0.02
Stomach	0.50±0.01	1.32±0.02
Intestine	1.34±0.01	1.29±0.01
Tail	0.25±0.01	0.21±0.01
Brain	0.046±0.003	0.025±0.002
HT29 Tumor	7.29±0.08	7.88±0.09

3.3 Discussion

The array of conditions for radiolabeling revealed that [^{55}Co]Co-DSar is best radiolabeled at pH=8 with increased temperature (45±9 MBq/nmol after 4 h at 80°C). The de-protonation of the two ammonium groups from DSar (pK_1~6.4 and pK_2~5.3 [106,152]) at higher pH will reduce electrostatic repulsion for positively charged hexaaquacobalt(II) in solution, which potentially explains higher AMA for increasing pH beyond pH=5.5. Since radiolabeling at pH=7 gave comparable results (37±7 MBq/nmol after 4 h at 80°C) to pH=8, Co hydrolysis (pK~9.8 at 25°C) may begin to compete against the de-protonation of DSar at higher pH. Improved AMA from increasing temperature (and time) is likely a general phenomenon of the complex being more thermodynamically favorable. In comparison to $^{64/67}$Cu, where radiolabeling to Sar derivatives is often performed at room temperature [108,140,141,147], the [^{55}Co]Co-DSar complexation rate(s) observed in this work is slower, corroborating previous studies at higher ligand concentration [148]. The reaction kinetics for Cu is generally expected to be faster than Co because the inner sphere H_2O exchange rate for Cu is approximately 3 orders of magnitude greater than Co [153]. Despite this, since [^{55}Co]Co-DSar can be radiolabeled at pH=7 and 37°C to yield 6±2 MBq/nmol after 2 h, future development with Co-DSar radiopharmaceuticals can employ pH- and temperature-sensitive targeting vectors as the AMA is suitable for a wide variety of pre-clinical applications *in vivo*.

After establishing an appropriate radio-TLC protocol for distinguishing [^{55}Co]Co-DSar from [^{55}Co]$CoCl_2$ and resolving the optimal radiolabeling procedure, *in vitro* [^{55}Co]Co-DSar stability experiments were performed to verify the kinetic inertness with n.c.a. The high [^{55}Co]Co-DSar *in vitro* stability observed in this work corroborates the kinetic inertness of several Co-Sar complexes, including Co-DSar, that have been synthesized in macro-scale quantities [89,105,106,149]. Also, the range of incubation times investigated for the stability studies are >5x and >10x the half-life of ^{55}Co and ^{58m}Co, respectively, which is suitable for most radiopharmaceutical applications. Since n.c.a. [^{55}Co]Co-DSar demonstrated stability *in vitro* for >96 h against 50 mM EDTA at pH=7 and human serum, the compound was then evaluated in mice to assess the *in vivo* stability and pharmacokinetics. [^{55}Co]Co-DSar exhibited a different pharmacokinetic profile compared to [^{55}Co]CoCl$_2$, where [^{55}Co]Co-DSar was cleared from the blood pool faster than [^{55}Co]CoCl$_2$ and had less liver uptake. [^{55}Co]Co-DSar cartilage uptake may be due to its small size and electrostatic interactions between highly positively charged [^{55}Co]Co-DSar and the negatively charged glycosaminoglycans in synovial fluid [154,155]. Although [^{55}Co]Co-DSar had short blood circulation times, making *in vivo* stability evaluations difficult, these results validate the radio-TLC method for discriminating [^{55}Co]Co-DSar from [^{55}Co]CoCl$_2$ and indicate that n.c.a. [^{55}Co]Co-DSar does not immediately degrade *in vivo*.

Given the *in vivo* pharmacokinetics of [^{55}Co]Co-DSar, [^{55}Co]Co-NT-Sarcage was subsequently synthesized using optimized radiolabeling conditions and intravenously injected into a murine xenograft model to explore the potential of [^{55}Co]Co-DSar based radiopharmaceuticals for pre-clinical research. The comparable biodistribution profiles of [^{55}Co]Co-NT-Sarcage and [^{64}Cu]Cu-NT-Sarcage suggest that the compound retained the tumor targeting properties of SR142948A after radiolabeling. The high [^{55}Co]Co-NT-Sarcage uptake in the tumor and relatively low uptake in healthy organs may enable therapeutic applications using [^{58m}Co]Co-NT-Sarcage [88,125]. Previous work [90] showed that ^{55}Co achieved better tumor-to-heart and tumor-to-liver ratios over ^{64}Cu radiolabeled with the same NO2A-conjugated molecule at 24 h p.i. The tumor-to-liver ratio of [^{55}Co]Co-NT-Sarcage observed in this work is ~2x that of [^{64}Cu]Cu-NT-Sarcage at 24 h p.i., but with comparable tumor-to-heart and tumor-to-kidney ratios. The similar mouse age/size/strain, tumor sizes and total ligand masses administered in mice for both radiopharmaceuticals suggest that the difference in tumor-to-liver ratio is likely a (radio)chemical effect as opposed to differences in biological processes. This difference could potentially be attributed to the different oxidation states between Cu and Co after complexation with DiAmSar derivatives [146], where Cu and Co exist in the 2+ and 3+ oxidation state, respectively. Additional comparative studies between ^{64}Cu- and ^{55}Co-DSar radiopharmaceuticals are needed to elucidate systematic differences in tumor-to-organ ratios and pharmacokinetics. Radiolabeling ^{55}Co to different chelators functionalized with the same long-circulating targeting vector, as in Cooper et al. [108], might resolve tradeoffs between *in vivo* stability and radiolabeling kinetics/environment.

3.4 Conclusion

This chapter established the optimal radiolabeling conditions for [^{55}Co]Co-DSar and produced [^{55}Co]Co-DSar and [^{55}Co]Co-NT-Sarcage suitable for *in vivo* applications. The highest [^{55}Co]Co-DSar AMA achieved in this work was 45 MBq/nmol EOS after reacting for 4 h at 80°C and pH=8. The stability of [^{55}Co]Co-DSar was investigated *in vitro,* and results suggest that the complex is kinetically inert. The pharmacokinetic profile of [^{55}Co]Co-DSar was distinct from [^{55}Co]$CoCl_2$ and showed brief accumulation in cartilage tissues with predominantly renal clearance. [^{55}Co]Co-NT-Sarcage exhibited a similar overall biodistribution profile to [^{64}Cu]Cu-NT-Sarcage with better tumor-to-liver ratio. The observed high tumor uptake and contrast may enable future applications as a targeted radionuclide therapy once ^{55}Co is substituted with ^{58m}Co. As this is the first report of ^{55}Co radiolabeled to DSar and DSar-conjugated derivatives, future work using [^{55}Co]Co-DSar with other targeting paradigms is warranted.

Chapter 4. Redox activity of Co-NOTA complexes

Disclaimer: the work in this chapter was submitted to Angewandte Chemie. This work was performed in collaboration with Dr. Dariusz Śmiłowicz, Dr. Andrey Joaqui-Joaqui, Dr. Abhijit Bera, Zhuoran Zhong and Dr. Eszter Boros and the Cyclotron research group at the University of Wisconsin-Madison. The Boros group synthesized all ligands used in this work. Justin Jeffery, Ashley Weichmann and Dr. Zachary Rosenkrans at the University of Wisconsin-Madison Carbone Cancer center assisted with animal experiments. All collaborators participated in fruitful discussions that improved the quality of work in this chapter and participated in editing the manuscript in some way, shape or form.

Cobalt exhibits environment-dependent redox activity between its divalent and trivalent oxidation states for most complexes in solution [110,112,156–161]. Although there have been no reports regarding reduced *in vivo* stability of Co radiopharmaceuticals due to this potentially redox active nature, such considerations for Cu have led to a new family of sarcophagine-based radiopharmaceuticals that are currently undergoing clinical trials [108,109,140,141]. Nevertheless, there is a noticeable lack of experimental evidence to confirm the oxidation state of Co-NOTA radiopharmaceuticals, where many publications do not consider Co oxidation after radiolabeling [113,162,163].

Prior to complexation with (radio)pharmaceutical precursors, Co is likely in the divalent oxidation state due to the large hexaaqua $Co^{3+/2+}$ reduction (redox) potential [156]. However, the redox potential of $Co^{3+/2+}$ complexes can be altered by different donor ligands, where even the ligand environment can have a substantial effect (see Figure 4-1). To illustrate this, researchers synthesized similar CoN_6 coordinating complexes and observed differences of ~0.6 V depending on the substituent group(s) [164,165]. Given the wide range of redox potentials for Co complexes, Table 4-1 lists the redox potentials for various Co-chelate complexes in solution for reference.

Table 4-1 A survey of Co$^{3+/2+}$ redox potentials for cobalt-chelate complexes found in literature. Redox potentials not reported against the normal hydrogen electrode (NHE) are marked with an asterisk and brackets denote the voltage offset used to convert values to NHE.

Complex	Redox potential vs. NHE (V)	Reference
$Co(OH_2)_6{}^{3+/2+}$	1.4-1.9	[166]
$Co(DTPA)\text{-}Rev^{-/2-}$	1.111	[161]
$Co(NO2A)\text{-}CF_3{}^{+/0}$	0.207	[112]
$Co(EDTA)\text{-}Rev^{0/-}$	0.146	[161]
$Co(DO3A)\text{-}Rev^{0/-}$	0.142	[161]
$Co(NOTA)^{0/-}$	0	[111]
$Co(NH_3)_6{}^{3+/2+}$	-0.02	[167]
$[Co((NH_3)_2sar)]^{5+/4+}$	-0.304* (+0.236 V)	[165]
$[Co((CO_2Et,CH_3)oxosarH_{-})]^{2+/+}$	-0.564* (+0.236 V)	[165]

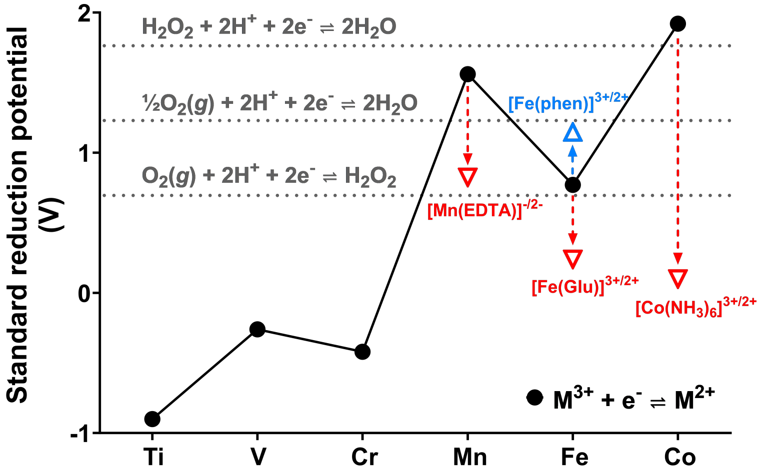

Figure 4-1 The reduction potential of various first-row transition metals in aqueous media against the standard hydrogen electrode (data taken from [168]). The reduction potential can be modulated by altering the coordinating environment.

Most Co radiopharmaceuticals are conjugated with NOTA, DOTA, or their derivatives. For Co-DO3A/DOTA complexes, Heppeler et al. assigned Co the divalent oxidation state based on results from nuclear magnetic resonance (NMR, high spin paramagnetic complex) and X-ray crystallography (lack of Jahn-Teller distortion) [169]. Heppeler et al. also alluded to results from previous works that demonstrated general redox stability for methylated tertiary amine complexes with divalent transition metals (both open chain and macrocyclic) [170,171]. However, those authors did not discuss differences in redox potential/stability between their tertiary amine compounds and (poly)amino(poly)carboxylic acids such as EDTA, diethylenetriaminepentaacetic acid (DTPA), NOTA, and DOTA. Several bodies of work to determine an optimal chelate construct for Co radiopharmaceuticals referenced these results to assume that Co(II) does not oxidize after complexation with NOTA and DOTA derivatives [113,162]. Previous studies had shown that NOTA can stabilize the trivalent state of Co [111], in contrast to 1,4,7-triazacyclononane (TACN) complexes with amide/alcohol pendent arms and other functional groups [172]. Additionally, Yu et al. also demonstrated that NO2A can form redox active complexes with $Co^{3+/2+}$ [112]. Previous assumptions regarding the redox stability of Co-NOTA radiopharmaceuticals have led to scant discussions regarding oxidation kinetics. As the redox potential of common oxidizing agents such as O_2 (E^0 1.2 V vs. NHE) and H_2O_2 (E^0 1.8 V vs. NHE) are above most $Co^{3+/2+}$ complexes, their presence (including generated hydroxyl radicals from ionizing radiation) may also influence the redox activity of $Co^{3+/2+}$ complexes due to large concentration differences. Furthermore, the carrier-free Co concentration in radiolabeling solutions is ~nM (specific activity of 120 GBq/μg for ^{55}Co) which will be orders of magnitude lower than the concentration of O_2 in aerated solutions. The absence of such discussions in literature regarding the redox activity of Co-NOTA radiopharmaceuticals serves as the major impetus for this chapter, where the main goal is to elucidate the chemical redox speciation of Co-NOTA and -DOTA complexes.

In this work, NO2A- and NOTA-W-NH_2 complexes are first used as model ligand systems to simulate amide conjugation for analyzing the chemical speciation of Co-NO2A and -NOTA complexes (see Figure 4-2). The speciation of each complex is analyzed by LC-MS and radio-HPLC. Further characterizations by the Boros group will be alluded to in this chapter and are part of the submitted manuscript. Potential differences in oxidation rates for various CoL concentration are explored by incubating samples at 10-100’s μM CoL and compared to n.c.a. ^{55}Co. The oxidation kinetics are also investigated under a variety of biologically relevant conditions and/or those relevant for radiolabeling. Results from model ligand systems are then employed to synthesize single-redox species of [^{55}Co]Co-NO2A, -NOTA and -DO3A-PSMA-617, and administered *in vivo* using murine prostate cancer xenograft models to assess potential discrepancies.

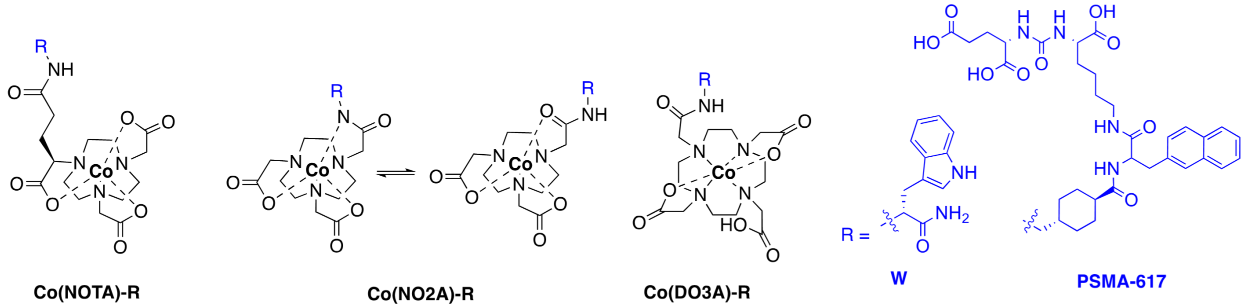

Figure 4-2 The chemical structures of select cobalt-chelate complexes that will be used in this work. Although PSMA-617 refers to the PSMA-targeting vector with DO3A conjugation in literature, the chelators will be explicitly named in this work to reduce confusion (e.g., DO3A-PSMA-617).

4.1 Materials and methods

4.1.1 Cyclotron production and separation of ^{55}Co

Cobalt-55 was produced by irradiating isotopically enriched ^{54}Fe targets (30-45 mg) with 8.2 MeV deuterons using the GE PETtrace at University of Wisconsin-Madison following methods from Chapter 2. The purified product was evaporated to dryness and reconstituted in 0.01 M HCl or DI H_2O for radiolabeling. All reagents used, e.g., 30% H_2O_2, were the same grade and purity as previously stated.

4.1.2 Synthesis of cobalt-chelate constructs

All ligands were synthesized by the Boros group at the University of Wisconsin-Madison and used as received. LC-MS analysis was performed by using an Agilent 1100 Series apparatus with an LC/MSD trap and Daly conversion dynode detector with UV detection at 220 and 254 nm (column: Phenomenex Luna, C18(2) 150x3 mm). Gradient of A (0.1 % formic acid in water) to 95 % B (0.1 % formic acid in MeCN), flow rate 0.8 mL min 0–3 min: 5 % B, 3–10 min: 5–95 % B, 10–13 min: 95 % B, 13–13.5 min: 95–5 % B, 13.5–16 min: 5 % B. The LC-MS was operated in the positive ion mode for all analysis. Radio-HPLC analysis was performed using an Agilent 1260 Infinity II equipped with a binary gradient pump, UV-vis detector (254 nm), manual injector (20 μL), a radio-detector and with the same Phenomenex column model, gradient and solvents as LC-MS. All samples were exposed to air and analyzed at 254 nm or with a radio-detector.

$NO2A-W-NH_2$ (1)

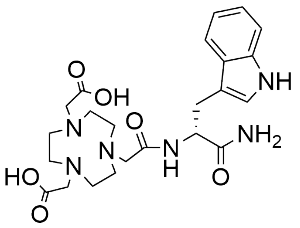

Chemical Formula: $C_{23}H_{32}N_6O_6$
Exact Mass: 488.24
Molecular Weight: 488.55

(1)

*Figure 4-3 Chemical structure of (**1**).*

Approximately 1.5 µmol (~0.7 mg) of NO2A-W-NH_2 (**1**) was dissolved in 1.5 mL room-temperature (~25°C) ultrapure water. The solution was buffered to pH 7.4 using 0.1 M HEPES and complexed with Co using 1.5 molar equivalent of $CoCl_2$ (final volume 2.1 mL, 700 µM Co(**1**)). The complex formation was confirmed by LC-MS, and then 700 µL was taken for incubation with 8 or 100 molar equivalent H_2O_2. Given unexpected results of Co(**1**) from LC-MS analysis, Zn(**1**) complexes were synthesized using $Zn(NO_3)_2$ at the same concentration and M:L ratio, and incubated with 8 and 100 molar equivalents of H_2O_2 after confirming complex formation by LC-MS.

Reference Co(**1**) samples were then analyzed on the radio-HPLC (UV-vis at 254 nm) to corroborate the retention times of Co(**1**) and [^{55}Co]Co(**1**) given slight delays between the UV-vis detector and radio-detector. Co(**1**) was synthesized at pH 7.4 using 0.1 M HEPES buffer using methods described above except at lower ligand concentration and volume to better simulate radiolabeling conditions (20 µM product in 250 µL final volume). The final concentration of H_2O_2 in select samples was set at 0.1 M H_2O_2 instead of 100 molar equivalents H_2O_2 due to low ligand concentration expected for radiolabeling. [^{55}Co]Co(**1**) was radiolabeled at 3.7 MBq/nmol (1.85 MBq/vial, 250 µL final volume, pH=7.4) and reactions were first set at room temperature (~25°C) for approximately 60 minutes then incubated in 0.1 M H_2O_2 over several time points after confirming quantitative labeling by radio-HPLC. [^{55}Co]Co(**1**) was also radiolabeled at 9 MBq/nmol (3.7 MBq/vial, 100 µL final volume) to investigate the impact of pH, heat and sodium gentisate (GA) on speciation behavior. The solution was buffered to pH 4.5 using 0.1 M sodium acetate or pH 7.4 using 0.1 M HEPES buffer and reacted at room temperature (~25°C) for approximately 30 minutes. Then, after quantitative labeling as confirmed by radio-HPLC, aliquots of [^{55}Co]Co(**1**) were distributed into separate reaction vessels and incubated with GA (final concentration 10 mM GA) at 95°C over several time points.

NOTA-W-NH$_2$ (2)

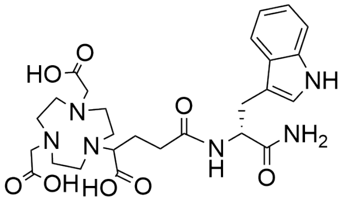

Chemical Formula: $C_{26}H_{36}N_6O_8$
Exact Mass: 560.26
Molecular Weight: 560.61

(2)

*Figure 4-4 Chemical structure of (**2**).*

Approximately 1.5 µmol (~0.7 mg) of NOTA-W-NH$_2$ (**2**) was dissolved in 1.5 mL room-temperature ultrapure water. The solution was buffered to pH 7.4 using 0.1 M HEPES and complexed with Co using 1.5 molar equivalent of $CoCl_2$ (final volume 2.1 mL, 700 µM Co(**2**)). The complex formation was confirmed by LC-MS then 700 µL was taken for incubation with 8 or 100 molar equivalent H_2O_2.

Reference Co(**2**) samples were also analyzed on the radio-HPLC (UV-vis at 254 nm) to corroborate the retention times of Co(**2**) and [^{55}Co]Co(**2**). [^{55}Co]Co(**2**) for both carrier added (c.a.) and n.c.a. samples were synthesized at pH 4.5 or pH 7.4 at a final concentration of 0.1 M sodium acetate or HEPES, respectively. Each sample either had 2 µM or 500 µM of (**2**) with 1.85 MBq ^{55}Co/vial (250 µL final volume). Carrier added samples were synthesized by first mixing $CoCl_2$ with (**2**) then adding ^{55}Co (final concentration of Co(**2**) ranged from 3.5 µM to 350 µM). Samples with 10 mM GA or 10 mM H_2O_2 were synthesized by adding 1:10 of 100 mM GA or 100 mM H_2O_2, respectively. Samples incubated at 95°C were vortexed periodically to maintain solution concentration. All samples were exposed to air and the fraction of oxidized species was determined by relative peak area from radio-HPLC. In cases where the fraction of oxidized species was clearly <50% by eye, the fraction of oxidized species was determined by 1 minus the relative peak area of the non-oxidized species.

DO3A-W-NH$_2$ (3)

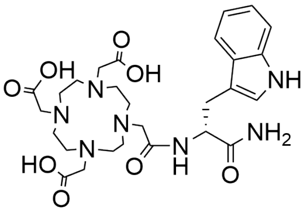

Chemical Formula: $C_{27}H_{39}N_7O_8$
Exact Mass: 589.29
Molecular Weight: 589.65

(3)

*Figure 4-5 Chemical structure of (**3**)*

The Boros group synthesized Co(**3**) under the same conditions and concentrations as Co(**1**) and Co(**2**) for LC-MS analysis.

NO2A-PSMA-617 (4)

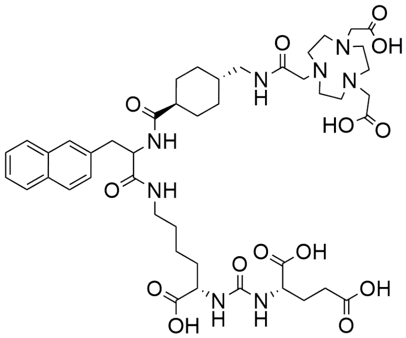

Chemical Formula: $C_{45}H_{64}N_8O_{14}$
Exact Mass: 940.45
Molecular Weight: 941.05

(4)

*Figure 4-6 Chemical structure of (**4**)*

Approximately 0.2 µmol (~0.2 mg) of NO2A-PSMA-617 (**4**) was dissolved in 1.0 mL room-temperature ultrapure water (200 µM (**4**)). Then, a sample vial containing 20 µL of 200 µM (**4**) solution was buffered to pH 4.5 using 0.1 M sodium acetate and complexed with Co using 1.5 molar equivalent of $CoCl_2$ (final volume 100 µL, 40 µM Co(**4**)). From this, each sample was mixed 1:1 with either ultrapure water or 20 mM GA and reacted at 95°C for 1 h (final volume 100 µL, 20 µM Co(**4**)). $[^{55}Co]$Co(**4**) was radiolabeled at 9 MBq/nmol (3.7 MBq/vial, 100 µL final volume). The solution was buffered to pH 4.5 using 0.1 M sodium acetate buffer and reacted at room temperature (25°C) for approximately 60 minutes. Then, after quantitative labeling as confirmed by radio-HPLC, samples taken for incubation with GA (final concentration 10 mM GA) at 95°C for 1 h to fully oxidize the compound.

NOTA-PSMA-617 (5)

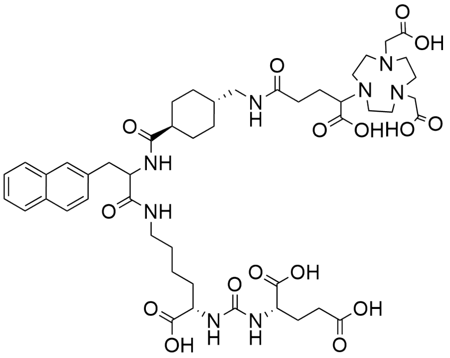

Chemical Formula: $C_{48}H_{68}N_8O_{16}$
Exact Mass: 1012.48
Molecular Weight: 1013.11
(5)

*Figure 4-7 Chemical structure of (**5**)*

Approximately 0.2 µmol (~0.2 mg) of NOTA-PSMA-617 (**5**) was dissolved in 1.0 mL room-temperature ultrapure water (200 µM (**5**)). Then, a sample vial containing 20 µL of 200 µM (**5**) solution was buffered to pH 7.4 using 0.1 M HEPES buffer and complexed with Co using 1.5 molar equivalent of $CoCl_2$ at 25°C for 1 h (final volume 200 µL, 20 µM Co(**5**)). [^{55}Co]Co(**5**) was radiolabeled at pH 7.4 and 25°C for 1 h (final volume 200 µL, 2 MBq ^{55}Co at 18.5 MBq/nmol). Carrier-added [^{55}Co]Co(**5**) was set by first mixing $CoCl_2$ with 20 µM (**5**) and labeled with 2 MBq ^{55}Co (15 µM Co(**5**) final concentration).

DO3A-PSMA-617 (6)

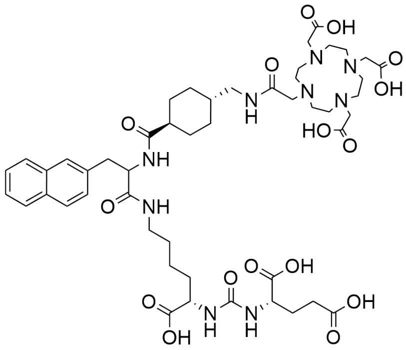

Chemical Formula: $C_{49}H_{71}N_9O_{16}$
Exact Mass: 1041.50
Molecular Weight: 1042.15

(6)

*Figure 4-8 Chemical structure of (**6**)*

Approximately 0.2 μmol (~0.2 mg) of DO3A-PSMA-617 (**6**) was dissolved in 0.5 mL room-temperature ultrapure water. The solution was buffered to pH 7.4 or pH 4.5 using 0.1 M HEPES or 0.1 M sodium acetate, respectively, and complexed with Co using 1.5 molar equivalent of $CoCl_2$ (final volume 1.0 mL, 200 μM Co(**6**)). The complex formation was confirmed by LC-MS. [^{55}Co]Co(**6**) was radiolabeled at pH 4.5 and 80°C for 1 h.

4.1.3 *In vitro* stability and cell experiments

Human serum stability

Sample purification after radiolabeling was performed using HLB cartridges (30 mg). Briefly, the cartridge was equilibrated with 3 mL DI H_2O, loaded with the sample, rinsed with 1 mL DI H_2O then eluted using 1 mL EtOH. The sample was evaporated under light Ar flow at 80°C and reconstituted in PBS to <10% EtOH. All samples had one dominant peak before and after purification. Purified ^{55}Co compounds were incubated with human serum at 37°C then mixed 1:1 with MeCN and centrifuged to remove excess protein prior to radio-HPLC analysis. Most of the activity was present in the supernatant for all compounds analyzed, suggesting a lack of transchelation to proteins in the serum.

Cell culture

PC3-PIP (PSMA positive) and PC3-Flu (PSMA negative) human prostate adenocarcinoma cells (ATCC) were cultured in RPMI 1640 medium with 10% FBS and 1% Pen-Strep at 37°C in a 5% CO_2 atmosphere using T75 flasks. Cells were resuspended using 0.25% Trypsin-EDTA and counted using a hemocytometer via an optical microscope.

Cell uptake and internalization

HLB purified [^{55}Co]Co(**4**), [^{55}Co]Co(**5**), and [^{55}Co]Co(**6**) were incubated with 10^5 PC3-PIP/PC3-Flu cells in 2 mL media (10 nM ligand, 3.7 MBq/nmol) for 4 h at 37°C in 35 mm Petri dishes. The membrane bound activity was stripped by incubating cells with 1 mL 0.1 M pH2 sodium citrate/citric acid solution for 5 min at room temperature (~25°C), and cells were dissociated using 1 mL 0.25% Trypsin-EDTA after incubating for 5 min at

37°C. Each petri dish was rinsed with at least 2 mL PBS prior to the next step (and last step).

4.1.4 Animal models

All animal studies were conducted under a protocol approved by the University of Wisconsin Institutional Animal Care and Use Committee. Food and water were available to mice *ad libitum*. Male athymic nude mice (5-6 weeks old) were purchased from the Jackson Laboratory. PC3-PIP and PC3-Flu tumors were established by subcutaneous injection of approximately 10^6 cells suspended in 100 µL of 1:1 PBS and Matrigel into the right and left axillary, respectively. Mice were inoculated with PC3-Flu tumors to confirm tracer specificity. *In vivo* PET imaging and *ex vivo* biodistribution were performed following methods from Chapter 3. Tumor sizes were ~5 mm in diameter prior to animal experiments (~1.5 weeks post xenograft). Each mouse (N=4 for each tracer) received either 2.6 MBq of HLB purified [^{55}Co]Co(**4**), [^{55}Co]Co(**5**) or [^{55}Co]Co(**6**) via tail vein injection. All samples had one dominant peak before and after purification. The total ligand mass injected per mouse was kept constant at approximately 0.8 nmol per mouse. PET imaging acquired pharmacokinetic profiles at 1, 4, 9 and 24 h p.i. Unless otherwise noted, uptake values are reported as mean±SD. Urine samples were non-invasively acquired from mice and injected directly onto the radio-HPLC for metabolite analysis.

4.2 Results

4.2.1 Redox speciation analysis for model peptides

The model ligands were designed to imitate the amide conjugation of most radiopharmaceuticals that employ NO2A/NOTA, provide large spectroscopic absorbance for analysis via LC-MS/HPLC and be stable against oxidizing agents such as H_2O_2. The ^{59}Co complexation studies used aqueous $CoCl_2$ to match the chemical form of ^{55}Co after separation from ^{54}Fe targets and pH7.4 was chosen to match physiological conditions. LC-MS analysis demonstrated that Co(**1**) is more stable against air oxidation (Figure 4-9) than Co(**2**) (Figure 4-10) but develops at least five resolvable chemical species (3 for Co^{2+}, 2 for Co^{3+}). LC-MS resolved two main chemical species for Co(**2**) after exposure to air for <10 min that correspond to the expected *m/z* for [$Co^{3+/2+}$(**2**)].

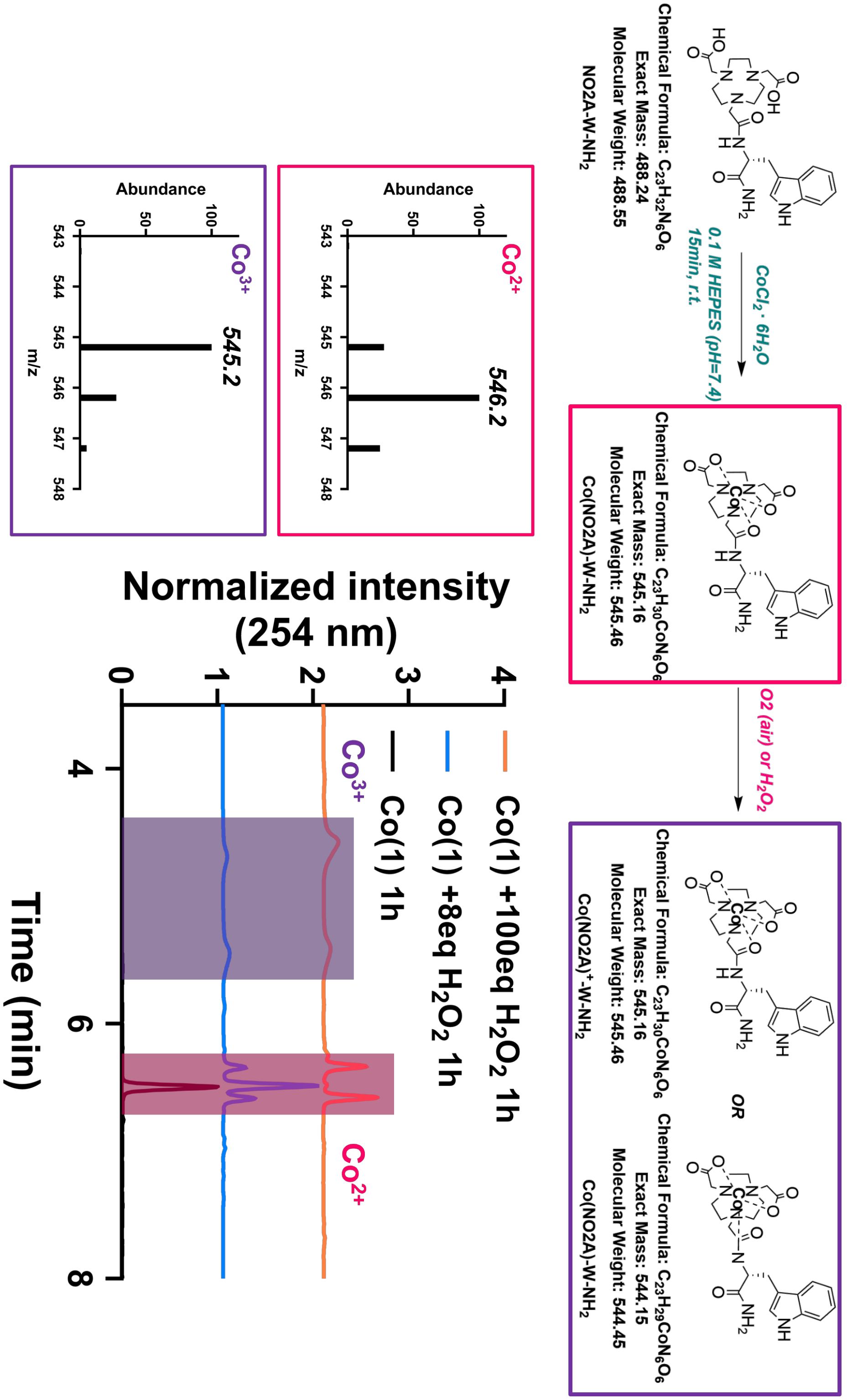

*Figure 4-9 Reaction scheme and corresponding LC-MS analysis for Co(**1**) incubated with and without H_2O_2. The limits were set to better visualize the relevant peaks of interest. The sample at 24 h did not exhibit any significant differences from the control sample at 1 h so it is omitted for clarity. The expected m/z for [Co(II)(**1**)+H$^+$]$^+$ and [Co(III)(**1**)]$^+$ is 546.16 (detected 546.2) and 545.16 (detected 545.2), respectively. The complex will have the same detected m/z even if the amide is coordinated to Co. The m/z for the two additional peaks in the Co(II)(**1**) region was checked by LC-MS and found to correspond with the original Co(II)(**1**) peak with no observed degradation.*

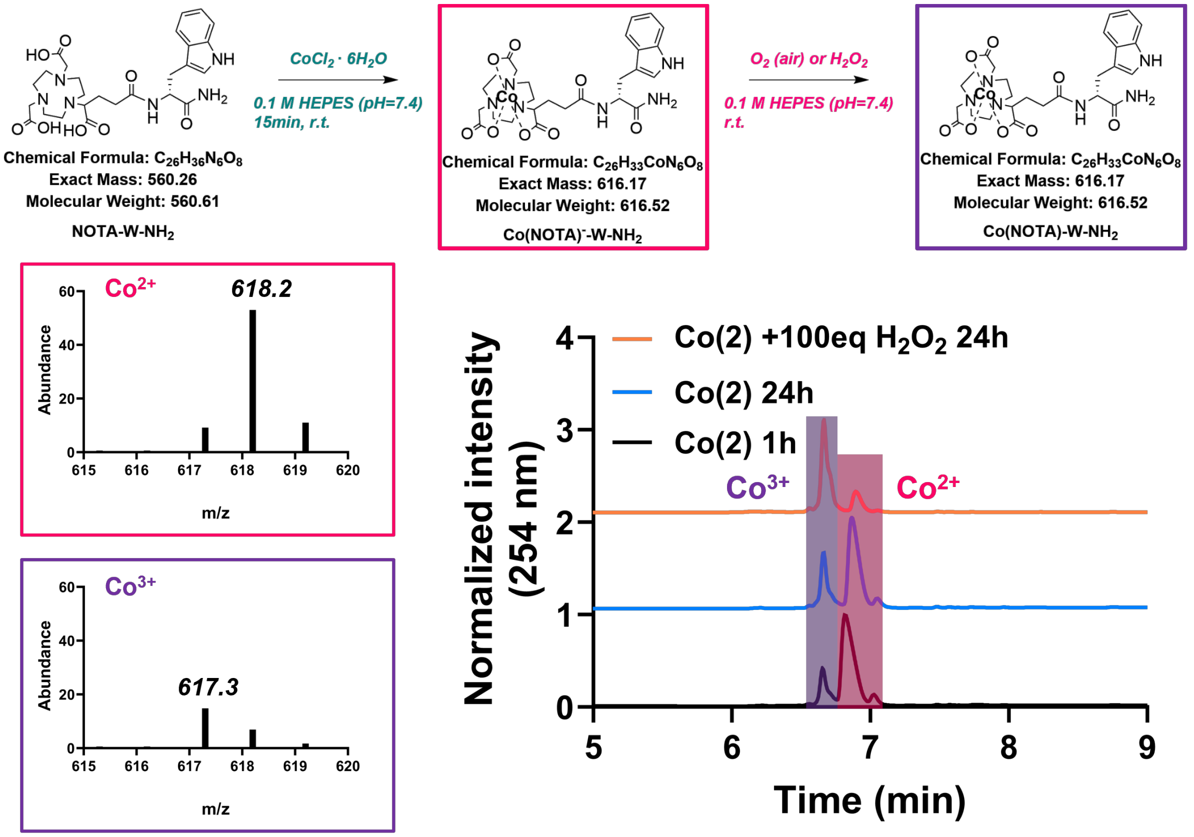

*Figure 4-10 Reaction scheme and corresponding LC-MS analysis for Co(**2**) incubated with and without H_2O_2. The limits were set to better visualize the relevant peaks of interest. Only the 100 eq H_2O_2 reaction at 24 h is shown for simplicity to demonstrate the increased rate of oxidation as compared to the control. The expected m/z for $[Co(II)(\mathbf{2})+2H^+]^+$ and $[Co(III)(\mathbf{2})+H^+]^+$ is 618.17 (detected 618.2) and 617.17 (detected 617.3), respectively.*

Due to the unexpected behavior of Co(**1**), Zn(**1**) was synthesized and incubated with H_2O_2 to assess ligand degradation (Figure 4-11). The reason for choosing Zn over other elements is due to its lack of redox activity for practically all aqueous complexes and similar coordination structure to Co(**1**). Although Zn(**1**) did not oxidize into a compound with -1 *m/z* unit, suggesting lack of Zn oxidation as expected, there was an observable degradation product after incubating with 100 eq H_2O_2 for 24 h that was not observed under similar conditions with Co(**1**). This degradation product may correspond to kynurenine (208.2 Da) and/or formylkynurenine (236.2 Da), which are known oxidation products of tryptophan (204.2 Da), based on LC-MS results.

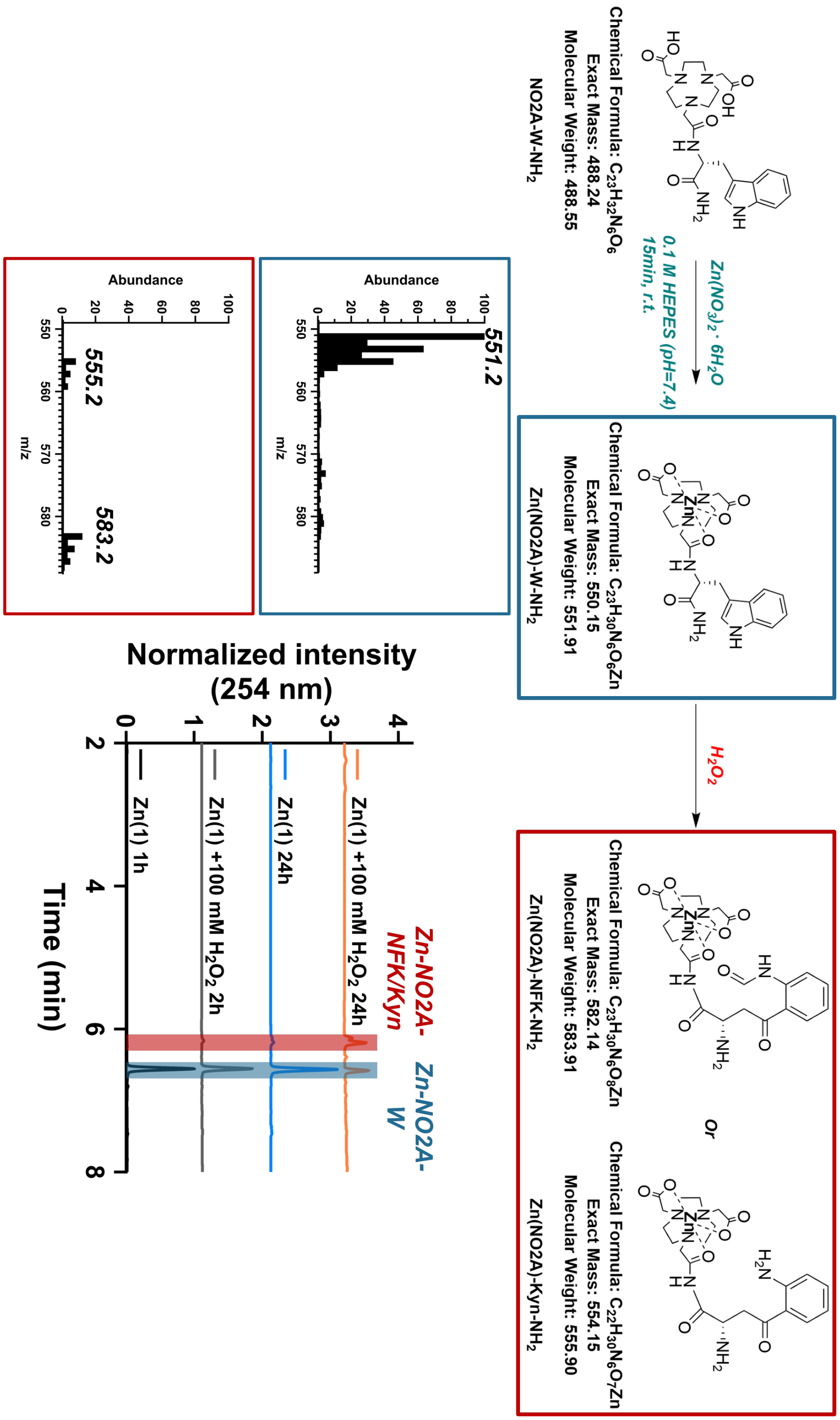

*Figure 4-11 Reaction scheme and corresponding LC-MS analysis for Zn(**1**) incubated with and without H_2O_2. The limits were set to better visualize the relevant peaks of interest. Incubating at 8 eq H_2O_2 did not show major deviation from the control (as compared to 100 eq H_2O_2). The expected m/z for $[Zn(II)(\mathbf{1})+H^+]^+$ is 551.15 (detected 551.2). If the tryptophan is oxidized to formylkynurenine (NFK) or kynurenine (Kyn) then the expected m/z will be 583.14 (detected 583.2) or 555.15 (detected 555.2), respectively.*

Radiochemical studies using n.c.a. ^{55}Co show that different oxidation states of [^{55}Co]Co(**1**) can be resolved on the radio-HPLC (Figure 4-12), though there appears to be more radiochemical species with lower retention times than [Co(**II**)(**1**)] that were not observed from Co(**1**). Interestingly, the radio-signal at the solvent front suggests that [^{55}Co]Co(**1**) may be degraded and/or dechelated. Due to the lack of observed signal(s) corresponding to (**1**) from LC-MS analysis of Co(**1**) over time, there is likely degradation beyond dechelation. Also, the multiple [^{55}Co][Co(**II**)(**1**)] peaks are nearly unresolvable due to larger peak widths from the radio-detector. Nevertheless, it is evident that the oxidation rate of the radiolabeled compound increases with lower pH, higher temperature, additional H_2O_2 and GA at 95°C.

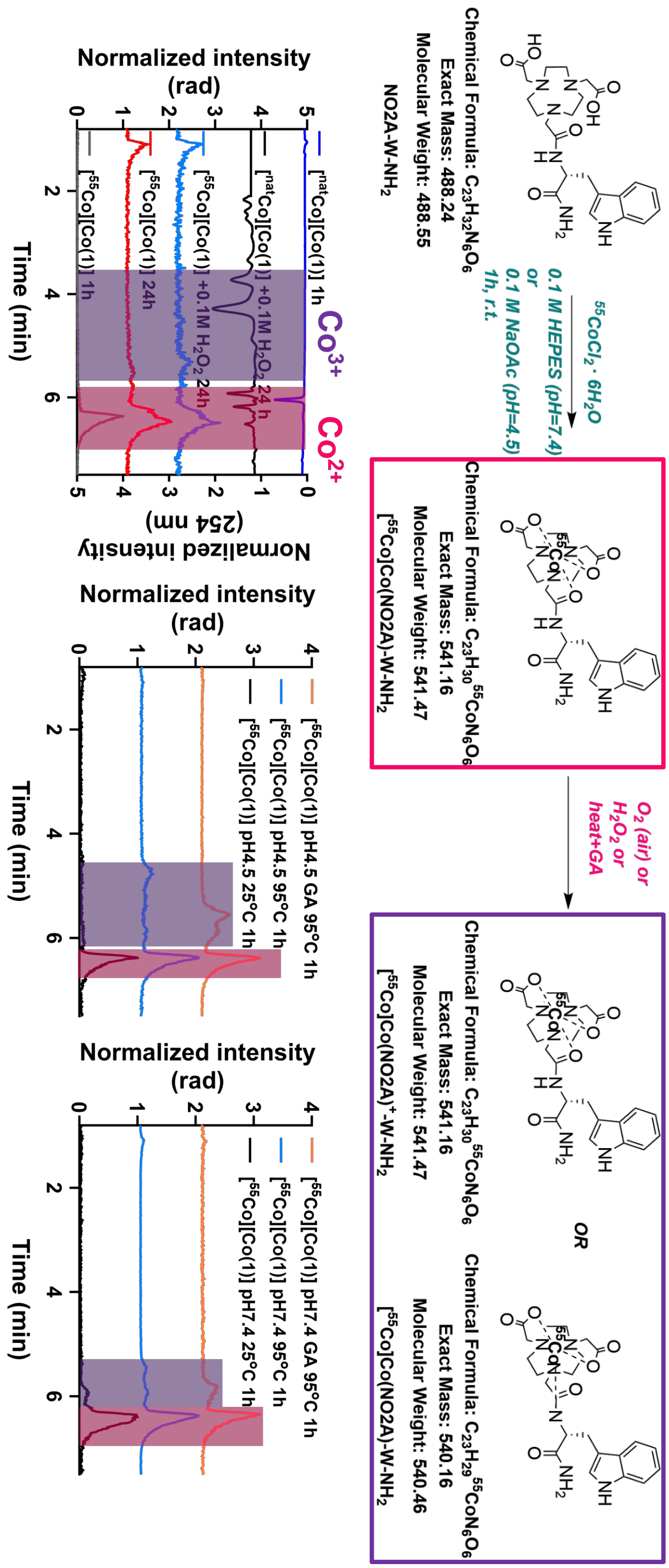

*Figure 4-12 Corresponding reaction scheme and HPLC/radio-HPLC chromatograms for Co(**1**) and [^{55}Co]Co(**1**) samples. All chromatograms in the bottom left plot were acquired using samples incubated at pH7.4. Radiochemical species with retention time less than [Co(II)(**1**)]^0, and larger than the solvent front, are assumed to be [^{55}Co][Co(III)(**1**)]$^+$ in this illustration.*

Similarly, different oxidation states of [^{55}Co]Co(**2**) can also be resolved on the radio-HPLC (Figure 4-13). However, unlike Co(**1**), the radiochemical speciation of [^{55}Co]Co(**2**) corresponds well with Co(**2**). Thus, a larger panel of experiments was designed to characterize the oxidation kinetics for [^{55}Co]Co(**2**). The fastest rate of oxidation can be ordered into the following categories (all else equal at pH7.4): GA+95°C, 95°C, pH4.5, and 10 mM H_2O_2. Also, the initial fraction of oxidation can be reduced by carrier addition in a concentration dependent manner.

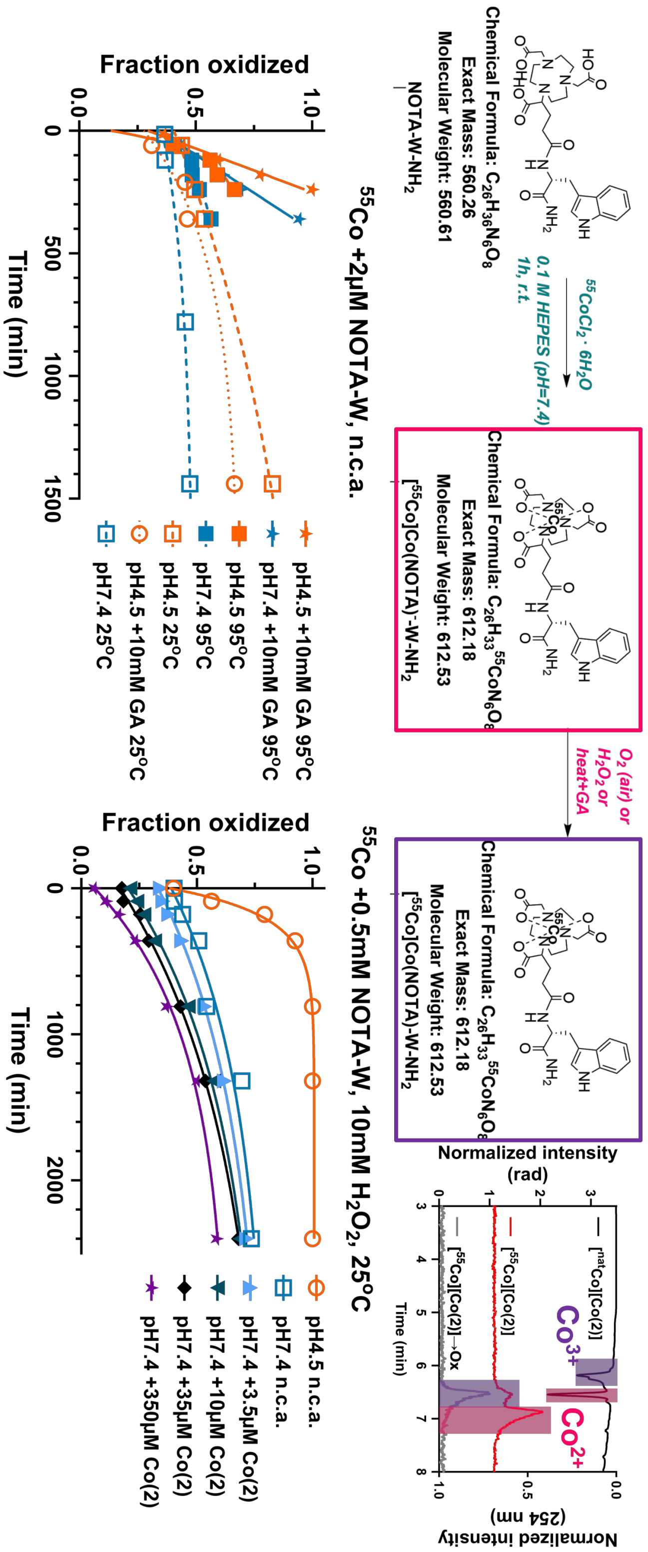

*Figure 4-13 Corresponding reaction scheme and HPLC/radio-HPLC chromatograms for Co(**2**) and [^{55}Co]Co(**2**) samples with the fraction of oxidized [^{55}Co]Co(**2**) under different conditions over time presented in the bottom two plots. All chromatograms in the top right plot were acquired using samples incubated at pH7.4. Due to the large (>70) number of chromatograms needed for kinetics analysis, only reference chromatograms are shown to demonstrate the two different redox species of Co(**2**) and [^{55}Co]Co(**2**).*

4.2.2 Redox speciation of ^{55}Co-labeled NO2A-, NOTA- and DO3A-PSMA-617

Since model complexes Co(**1**) and Co(**2**) demonstrate that the Co metal center could be oxidized from Co(II) to Co(III), the respective chelators were functionalized with a PSMA targeting vector and complexed with Co to verify the redox activity for radiopharmaceutical applications. Although LC-MS/radio-HPLC analysis for Co(**1**)/[^{55}Co]Co(**1**) exhibited behavior beyond the scope of Co redox considerations, only two chemical species of Co(**4**), corresponding to [Co(II)(**4**)] and [Co(III)(**4**)], were resolved on the LC-MS (Figure 4-14). The radiochemical species of [^{55}Co]Co(**4**) correspond well with Co(**4**), and [^{55}Co]Co(**4**) could be quantitatively oxidized by incubating the sample at pH4.5, 95°C and with 10 mM GA for 1 h.

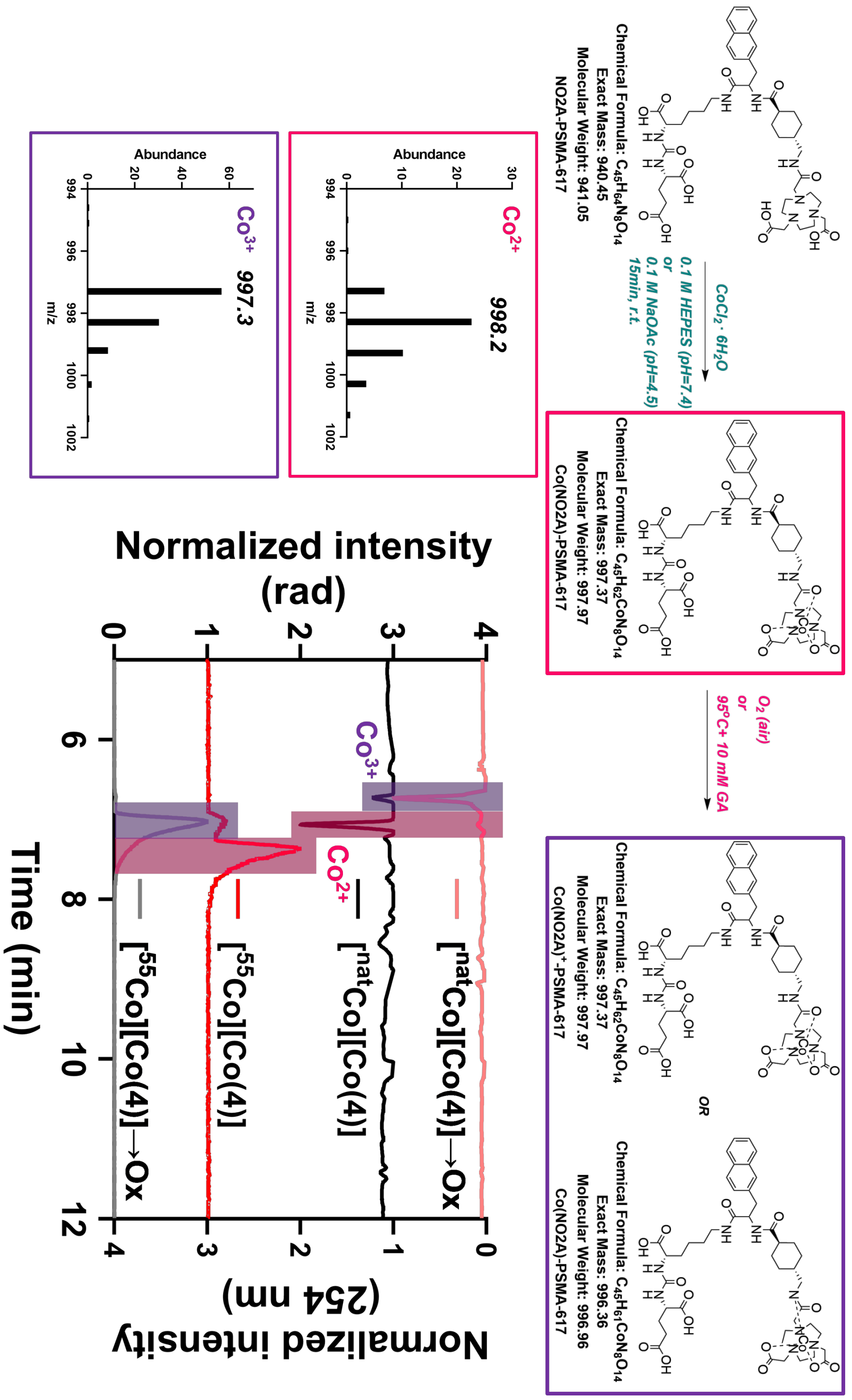

*Figure 4-14 Reaction scheme with proposed structures for Co(**4**) and corresponding LC-MS analysis. The UV-vis signal from GA has been removed to aid visualization. "Ox" refers to pH4.5 samples that were oxidized by incubating at 95°C with 10 mM GA for 1 h. The expected m/z for $[Co(II)(\mathbf{4})+H^+]^+$ and $[Co(III)(\mathbf{4})]^+$ is 998.37 (detected 998.2) and 997.37 (detected 997.3), respectively. The complex will have the same detected m/z even if the amide is coordinated to Co. Radio-HPLC traces for $[^{55}Co]Co(\mathbf{4})$ are included to better visualize the correspondence between the reference Co(**4**) chromatograms.*

In agreement with the redox behavior of Co(**2**), two chemical species of Co(**5**), [Co(II)(**5**)] and [Co(III)(**5**)], were resolved on the LC-MS and the radiochemical species of [^{55}Co]Co(**5**) correspond well with the reference (Figure 4-15). Also, [^{55}Co]Co(**5**) could be quantitatively oxidized under mild reaction conditions.

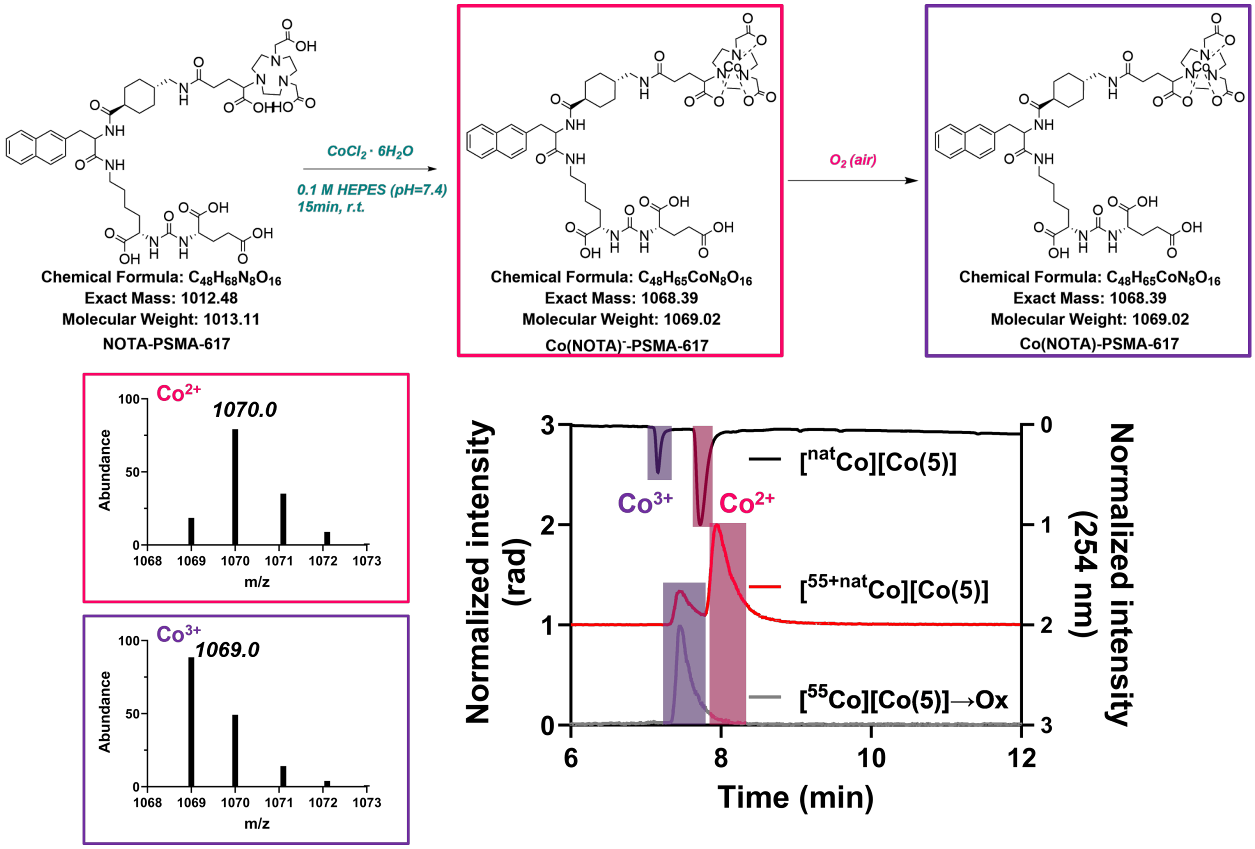

*Figure 4-15 Reaction scheme with proposed structures for Co(**5**) and corresponding LC-MS analysis. "Ox" refers to the sample that was oxidized by air with no carrier added. The expected m/z for $[Co(II)(\mathbf{5})+2H^+]^+$ and $[Co(III)(\mathbf{5})+H^+]^+$ is 1070.39 (detected 1070.0) and 1069.39 (detected 1069.0), respectively. Radio-HPLC traces for [^{55}Co]Co(**5**) are included to better visualize the correspondence between the reference Co(**5**) chromatograms.*

Since previously published results have shown that Co-DO3A complexes likely stabilize Co(II) [169], Co(**6**) was synthesized and incubated in pH7.4 and pH4.5 to evaluate its redox activity under mild conditions. In general, Co(**6**) is more redox stable than Co(**4**) and Co(**5**) but [Co(III)(**6**)] was confirmed by LC-MS 96 h post incubation in pH4.5 solution (Figure 4-16). Although there may be some oxidation at 48 h for the sample incubated at pH4.5, MS analysis had insufficient signal to confirm its existence. Also, because [^{55}Co]Co(**6**) was redox stable after radiolabeling at pH4.5 and 80°C for 1 h, it is likely that attempts to oxidize the sample will be impractical for radiopharmaceutical applications using ^{55}Co/^{58m}Co.

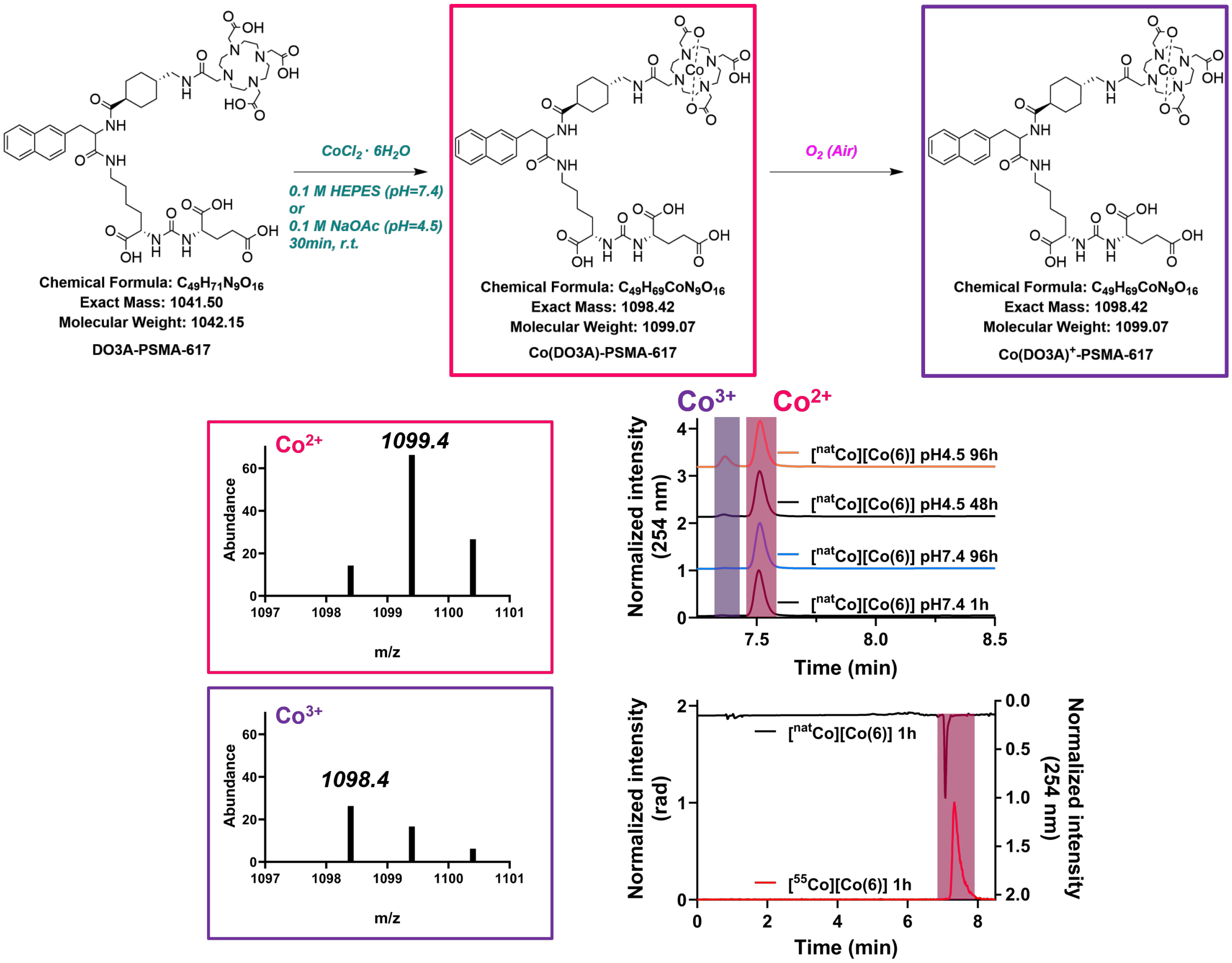

Figure 4-16 Reaction scheme with proposed structures for Co(**6**) and corresponding LC-MS analysis. The expected m/z for [Co(II)(**6**)+H$^+$]$^+$ and [Co(III)(**6**)]$^+$ is 1099.42 (detected 1099.4) and 1098.42 (detected 1098.4), respectively. Radio-HPLC trace for [^{55}Co]Co(**6**) is included to better visualize the correspondence between the reference Co(**6**) chromatogram.

4.2.3 *In vitro* serum stability and *in vitro* cell uptake

Since [^{55}Co]Co(**4**), [^{55}Co]Co(**5**) and [^{55}Co]Co(**6**) could be stabilized as one radiochemical species, each radiopharmaceutical was purified using HLB after radiolabeling with >95% radiochemical purity and incubated in human serum or PBS to assess the *in vitro* stability. Explicitly, the compounds investigated were [^{55}Co][Co(III)(**4**)], [^{55}Co][Co(III)(**5**)] and [^{55}Co][Co(II)(**6**)] based on prior LC-MS analysis. All compounds retained high radiochemical purity up to 48 h, and only [^{55}Co]Co(**4**) exhibited slight redox activity at 24 h after human serum incubation (Figure 4-17).

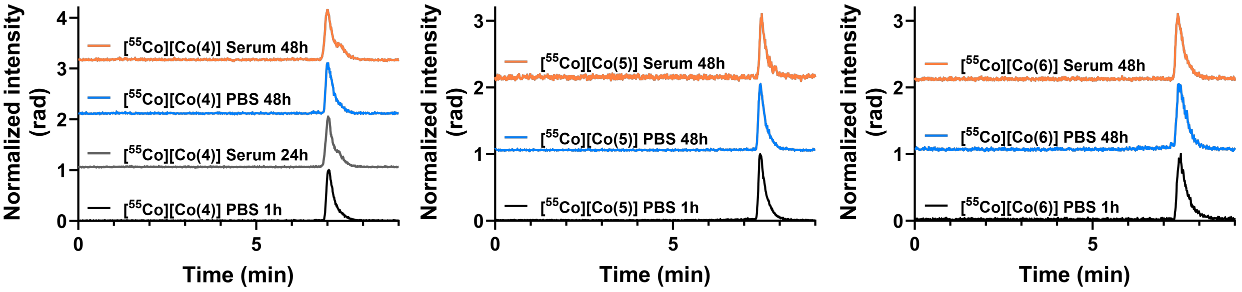

*Figure 4-17 Radio-HPLC chromatograms for [^{55}Co]Co(**4**) (left), [^{55}Co]Co(**5**) (middle) and [^{55}Co]Co(**6**) (right) incubated in either PBS or human serum.*

Given the promising *in vitro* stability for each compound, *in vitro* cell uptake experiments were performed to verify the PSMA-targeting properties of the radiopharmaceutical prior to *in vivo* animal experiments. Each petri dish (N=2 in triplicate) was seeded with the same batch of resuspended cells and incubated with 10 nM of each respective compound (radiolabeled at 3.7 MBq/nmol). As seen in Figure 4-18, all compounds exhibited high specificity for PSMA-positive PC3-PIP cells and similar fraction of internalized bound activity (~25%), where [^{55}Co]Co(**6**) achieved the highest uptake out of the 3 compounds and [^{55}Co]Co(**4**) had the lowest uptake.

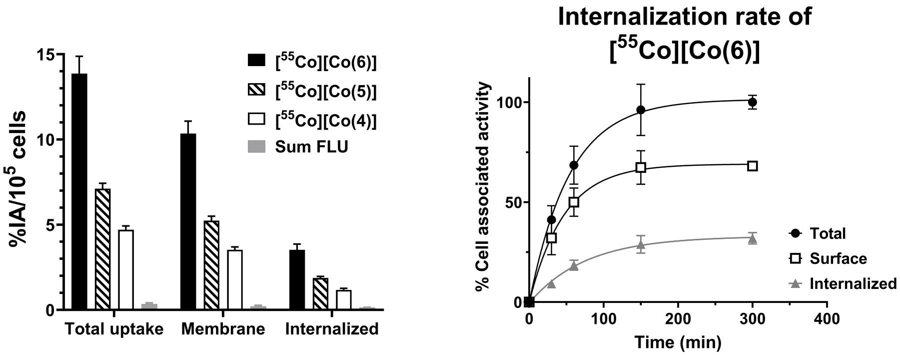

*Figure 4-18 In vitro cell uptake for each ^{55}Co radiopharmaceutical (left) incubated for 4 h at 37°C (10 nM ligand, 3.7 MBq/nmol). "Sum FLU" refers to the total uptake of all three compounds incubated with PSMA-negative PC3-Flu cells. The 4 h timepoint was chosen based on the internalization rate of [^{55}Co]Co(**6**) (right).*

4.2.4 *In vivo* biodistribution of ^{55}Co-labeled NO2A-, NOTA- and DO3A-PSMA-617

After validating the targeting properties of [^{55}Co]Co(**4**), [^{55}Co]Co(**5**) and [^{55}Co]Co(**6**) *in vitro*, each radiopharmaceutical was then administered in mice bearing PSMA-positive and -negative tumor xenografts to assess the *in vivo* biodistribution and tumor uptake. The biodistribution profile is similar for all three compounds, and [^{55}Co]Co(**6**) achieved the highest tumor uptake and tumor-to-kidney ratio at 24 h p.i. (see Figure 4-19, Figure 4-20 and Figure 4-21 for [^{55}Co]Co(**4**), [^{55}Co]Co(**5**) and [^{55}Co]Co(**6**), respectively, and Figure 4-22 shows the *ex vivo* biodistribution at 24 h p.i.).

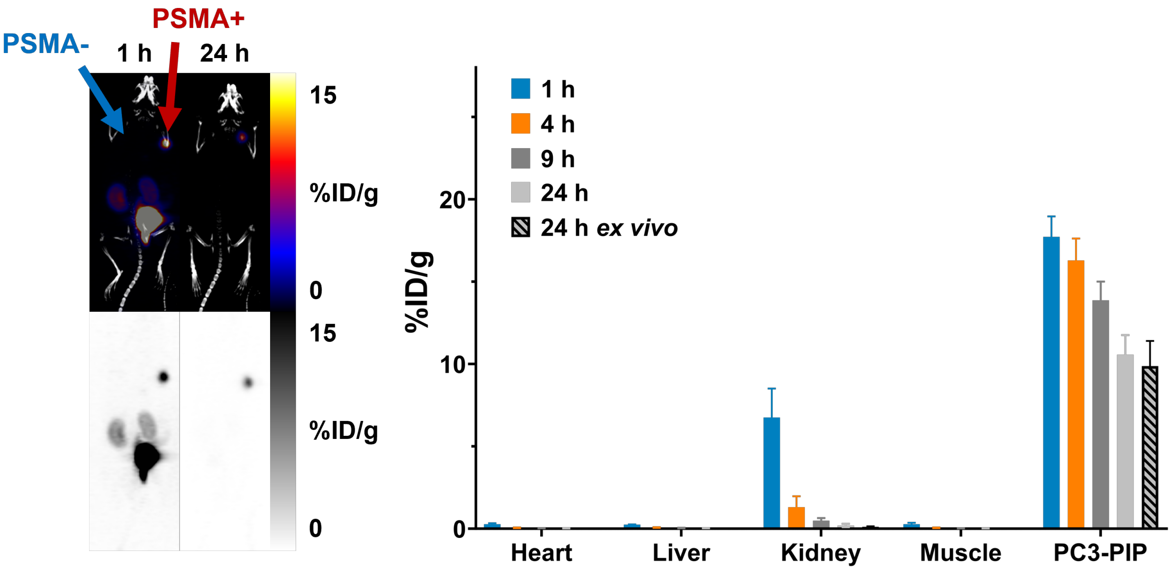

*Figure 4-19 In vivo maximum intensity projection PET/CT (left, top) and PET (left, bottom) images acquired at 1 and 24 h p.i. for [^{55}Co]Co(**4**). The arrows indicate positions of PSMA+ and PSMA- tumor xenografts. PET ROI quantified organ uptake values for select organs agree well with the ex vivo biodistribution at 24 h (right).*

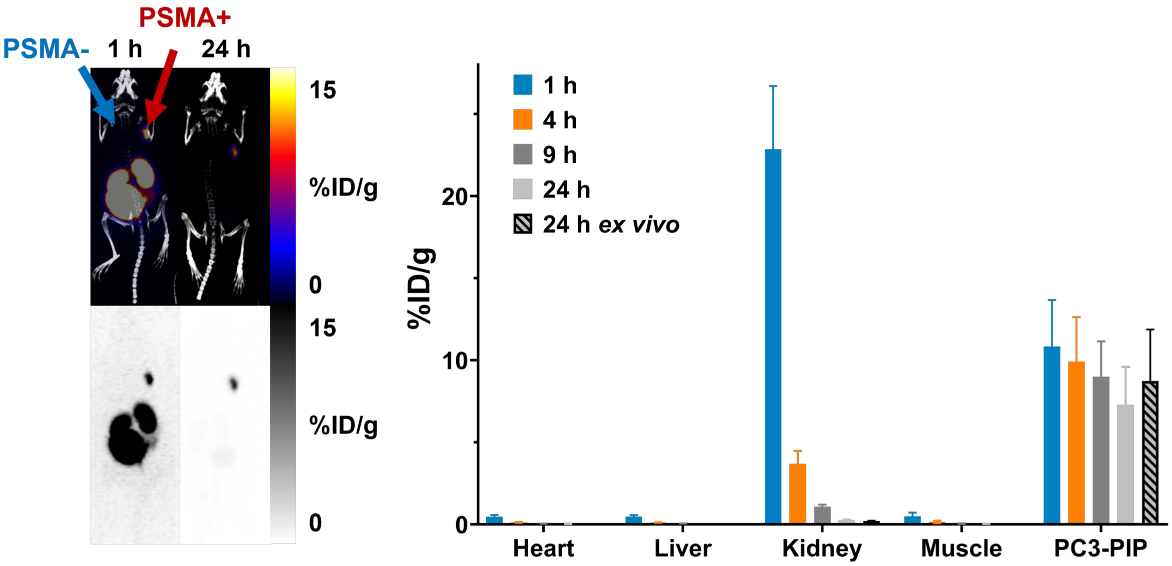

*Figure 4-20 In vivo maximum intensity projection PET/CT (left, top) and PET (left, bottom) images acquired at 1 and 24 h p.i. for [^{55}Co]Co(**5**). The arrows indicate positions of PSMA+ and PSMA- tumor xenografts. PET ROI quantified organ uptake values for select organs agree well with the ex vivo biodistribution at 24 h (right).*

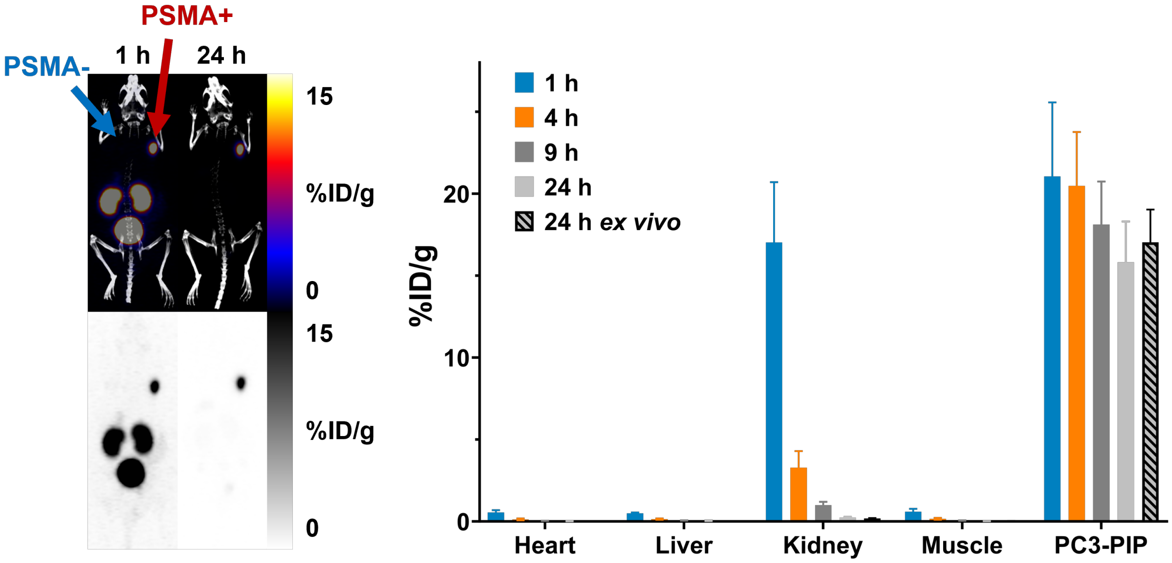

*Figure 4-21 In vivo maximum intensity projection PET/CT (left, top) and PET (left, bottom) images acquired at 1 and 24 h p.i. for [^{55}Co]Co(**6**). The arrows indicate positions of PSMA+ and PSMA- tumor xenografts. PET ROI quantified organ uptake values for select organs agree well with the ex vivo biodistribution at 24 h (right).*

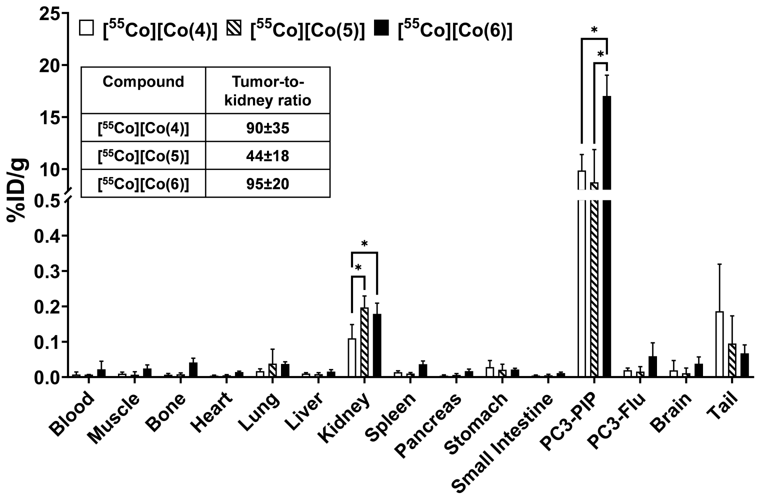

Compound	Tumor-to-kidney ratio
[^{55}Co][Co(4)]	90±35
[^{55}Co][Co(5)]	44±18
[^{55}Co][Co(6)]	95±20

*Figure 4-22 The ex vivo biodistribution of [^{55}Co]Co(**4**), [^{55}Co]Co(**5**) and [^{55}Co]Co(**6**) at 24 h p.i. The tumor uptake and tumor-to-kidney ratio was highest for [^{55}Co]Co(**6**). One star refers to $p<0.05$ using a two-tailed unpaired t-test.*

Although the tumor-to-kidney ratio for [^{55}Co]Co(**4**) was comparable to [^{55}Co]Co(**6**), urine metabolite analysis at 1 h p.i. show that [^{55}Co]Co(**4**) had degraded ~10% whereas the other two compounds did not have any observable degradation products (Figure 4-23).

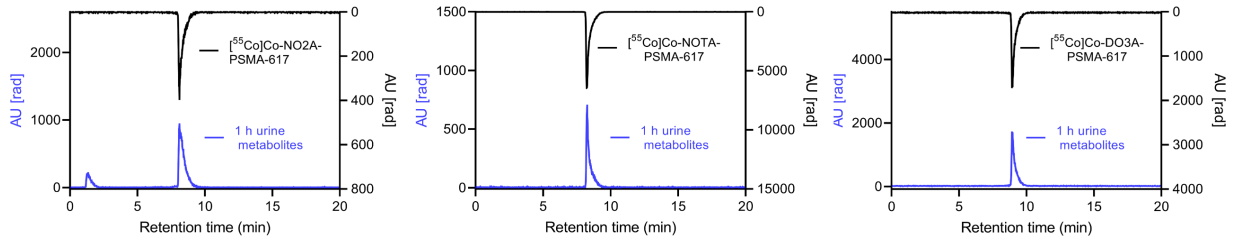

*Figure 4-23 Urine metabolite analysis at 1 h p.i. for [^{55}Co]Co(**4**) (left), [^{55}Co]Co(**5**) (middle) and [^{55}Co]Co(**6**) (right).*

4.3 Discussion

The redox potentials of Co-NO2A (0.2 V vs. NHE) and Co-NOTA (0 V vs. NHE) suggest that Co-NOTA complexes favor oxidation more than Co-NO2A. In this work, Co(**2**) and Co(**5**) oxidized faster than Co(**1**) and Co(**4**), respectively, agreeing with the predicted redox behavior. However, the existence of several [Co(II)(**1**)] species after incubating with H_2O_2 was unexpected, and the oxidation experiment with Zn(**1**) suggests that these are specific to the Co-NO2A chelate complex. Furthermore, the lack of observed tryptophan degradation for Co(**1**) compared to Zn(**1**) is likely due to the availability of an alternative oxidation pathway (i.e., Zn does not oxidize but Co can). Although [Co(II)(**1**)] exhibited multiple chemical species, these species were not resolved with [Co(II)(**4**)] using the same HPLC protocol which indicates that smaller molecules may be more effective to characterize the redox speciation of metal chelate complexes. Nonetheless, the model peptides were able to illustrate different oxidation states of Co-NO2A and -NOTA and enable subsequent radiochemical studies using ^{55}Co.

For both Co(**1**) and Co(**2**), the oxidation rate could be increased by incubating with H_2O_2 and at higher temperature. Given that the model complexes seemed to form Co(III) complexes after increased temperature and time, these results suggest that NO2A and NOTA form more thermodynamically stable complexes with Co(III). Interestingly, the Boros group was able to oxidize Co-DOTA and [^{55}Co]Co-DOTA (not functionalized) by adding 10 mM H_2O_2 (~25°C, exposed to air for 1 h). However, $[^{55}Co]$Co-DOTA with 10 mM H_2O_2 was reduced over time and became nearly identical to $[^{55}Co]$Co-DOTA without H_2O_2 at 20 h, in contrast to $[^{55}Co]$Co-NO2A which steadily oxidized over time. Furthermore, their results with Co(**3**) also suggested that the complex was redox stable in air at pH7.4 without H_2O_2. In combination with Co(**6**) and $[^{55}Co]$[Co(**6**)] complexes observed in this work, these results corroborate previously published work demonstrating that DO3A/DOTA likely stabilize Co(II) under radiopharmaceutical conditions [169]. The presence of detectable [Co(III)(**6**)] after incubating at pH4.5 for 96 h corroborates the observed oxidation of Co-DOTA from the Boros group but it contrasts with redox behavior at pH7.4 (i.e., oxidized product reduces over time for Co-DOTA). Nevertheless, the reaction conditions are likely impractical for synthesizing and stabilizing Co(III)-DO3A radiopharmaceuticals.

Downstream radiochemical experiments showed that the oxidation kinetics for Co-NO2A and Co-NOTA can be increased even further by adding sodium gentisate and incubating at 95°C. The exact mechanism for this behavior is not explored in this work but incubating with ascorbic acid and glutathione at low pH has led to similar results based on experience. One potential explanation could be that the degradation products from oxidized radical scavenger(s) have sufficiently high redox potential to oxidize the Co complexes but not high enough to degrade other parts of the molecule. The PSMA-functionalized Co-NO2A/NOTA (Co(**4**) and Co(**5**)) oxidized faster than the tryptophan-functionalized complexes (Co(**1**) and Co(**2**)). These results suggest that differences in ligand environment can lead to changes in oxidation rate despite having the same coordinating groups/structure [164,165]. Furthermore, the initial fraction of oxidation for

[^{55}Co]Co(**2**) and [^{55}Co]Co(**5**) can be reduced by carrier addition. A closer inspection of the oxidation rate reveals that the exponential constant (K) for each of the c.a. [^{55}Co]Co(**2**) reactions set at pH7.4 are not significantly different once the model is constrained using a plateau of 1 (five reactions, unpaired statistical p=0.8999 assuming constant K=4.0x10^{-4} min^{-1} for each reaction), which suggests that the inherent oxidation rate is not changed with Co concentration. Unfortunately, a similar analysis using [^{55}Co]Co(**5**) is impractical due to the rapid oxidation of n.c.a. [^{55}Co]Co(**5**) without any additives at pH7.4 and 25°C (quantitative oxidation in <5 min). The initial fraction of oxidization was ~0.10 for both c.a. [^{55}Co]Co(**2**) and [^{55}Co]Co(**5**) using 350 μM Co(**2**) and Co(**5**), respectively. Preliminary experiments show that 20 μM Co(**4**) and n.c.a. [^{55}Co]Co(**4**) both had similar initial fraction of oxidation (~0.20) and can both be quantitatively oxidized after incubating at pH4.5, 95°C with 10 mM GA for 1 h. The differences in oxidation kinetics observed in this work for Co(**1**)/Co(**4**), Co(**2**)/Co(**5**) and their ^{55}Co counterparts will need to be thoroughly evaluated using other NO2A/NOTA conjugated molecules prior to any conclusive statements. As the first work of its kind, the results presented here will facilitate future experimentation in this area.

This work demonstrated the possibility of synthesizing one observable radiochemical species of ^{55}Co with functionalized NO2A, NOTA and DO3A at timescales relevant for radiopharmaceuticals. The administration of a single radiochemical species enables direct evaluations of the complex and facilitates the interpretation of subsequent *in vitro* and *in vivo* results. *In vitro* cell uptake experiments demonstrated approximately 2x more uptake for [^{55}Co]Co(**6**) relative to [^{55}Co]Co(**5**) and 1.4x more uptake for [^{55}Co]Co(**5**) relative to [^{55}Co]Co(**4**). This trend may be due to differences in the overall charge of the complex, which can lead to changes in the binding affinity of the ligand-receptor complex. Explicitly, each compound likely exists as [^{55}Co][Co(II)(**6**)]$^{-}$, [^{55}Co][Co(III)(**5**)]^{0} and [^{55}Co][Co(III)(**4**)]$^{+1}$ during incubation with cells at pH7.4. Due to the possibility for amide coordination to the Co metal center, [^{55}Co][Co(III)(**4**)] may exist as [^{55}Co][Co(III)(**4**)]^{0} which would confound the interpretation above. Future experiments to elucidate the redox states and coordination structure of Co-NO2A radiopharmaceuticals are currently ongoing. However, the NO2A chelator may be less suitable for Co radiopharmaceuticals due to its slight redox instability in human serum and degradation *in vivo*. Alternatively, this degradation effect may be exploited to implement other modes of drug delivery though more research is necessary to characterize the degradation pathway. The *in vitro* cell uptake experiments would predict the highest tumor uptake for [^{55}Co]Co(**6**) then [^{55}Co]Co(**5**) and [^{55}Co]Co(**4**), in descending order, but the animal studies indicate that [^{55}Co]Co(**5**) and [^{55}Co]Co(**4**) attained similar *in vivo* tumor uptake. Thus, *in vitro* results should only be referred to as a general guideline for screening radiopharmaceuticals and *in vivo* animal models are necessary to probe complex biological systems. Although [^{55}Co]Co(**6**) exhibited the best tumor uptake and tumor-to-kidney ratio, NOTA could still be a viable chelator for other Co radiopharmaceuticals given its stability under a wide variety of conditions explored in this work and the fast oxidation rate.

4.4 Conclusion

Co-NO2A and -NOTA complexes stabilize Co(III), contrasting Co-DO3A complexes that preferentially stabilize Co(II), and Co-NOTA complexes oxidize faster than Co-NO2A. The oxidation rate for both Co-NO2A and -NOTA complexes can be increased with lower pH, increased temperature (with/without sodium gentisate) and additional H_2O_2. Overall trends in redox behavior correspond well between model peptides and PSMA-functionalized chelators, where Co-NOTA complexes oxidize faster than Co-NO2A complexes. The ^{55}Co radiopharmaceuticals investigated in this work can be synthesized as one radiochemical species, and their overall biodistributions were similar (renal clearance with short blood circulation times). [^{55}Co]Co-DO3A-PSMA-617 achieved the highest tumor uptake (~18%ID/g at 24 h p.i.) and both [^{55}Co]Co-NO2A-PSMA-617 and [^{55}Co]Co-NOTA-PSMA-617 had similar tumor uptake (~10%ID/g at 24 h p.i.). The tumor-to-kidney ratio was similar between [^{55}Co]Co-DO3A-PSMA-617 and [^{55}Co]Co-NO2A-PSMA-617 (~90 at 24 h p.i.) and about half for [^{55}Co]Co-NOTA-PSMA-617. Slight degradation products in the urine at 1 h p.i. for [^{55}Co]Co-NO2A-PSMA-617 suggests that NOTA and DO3A may be more suitable chelators for Co radiopharmaceuticals with longer blood circulation times.

Chapter 5. Theranostic cobalt-55/58m for neurotensin receptor-mediated radiotherapy *in vivo*: pilot studies with dosimetry

Disclaimer: data from this chapter related to NO2A-NT-20.3 was published in Pharmaceutics and Nuclear Medicine and Biology in collaboration with Dr. Hailey Houson, Dr. Volkan Tekin and Dr. Suzanne E. Lapi from the University of Alabama at Birmingham (UAB) and the Cyclotron research group at the University of Wisconsin-Madison. UAB provided the NO2A-NT-20.3 molecule. Data from this chapter related to NOTA-CB-SR142948A was published in The Journal of Nuclear Medicine in collaboration with Dr. German Oscar Fonseca Cabrera, Xinrui Ma, Dr. Zibo Li and Dr. Zhanhong Wu from UNC and the Cyclotron research group at the University of Wisconsin-Madison. UNC synthesized the NOTA-CB-SR142948A molecule. Justin Jeffery, Ashley Weichmann and Dr. Zachary Rosenkrans at the University of Wisconsin-Madison Carbone Cancer center assisted with animal experiments. Dr. Andres Mejia from Research Animal Resources and Compliance Comparative Pathology laboratory at University of Wisconsin-Madison interpreted and conducted mouse kidney histology. All collaborators participated in editing the manuscripts in some way, shape or form.

Research from the preceding chapters can be synthesized to facilitate theranostic applications of ^{55}Co and ^{58m}Co. The target fabrication, irradiation and ^{5x}Co purification process as described in Chapter 2 can lead to [^{55}Co]Co-NOxA and -DOxA with AMA suitable for RPT applications. Radiochemical investigations of ^{55}Co from Chapter 3 and Chapter 4 characterized the behavior of Co chelation and redox activity under n.c.a. conditions for most clinically relevant chelators at the time of writing this document. As previously mentioned, ^{55}Co is an attractive chemical surrogate for ^{58m}Co because of the ease of handling (moderate half-life and high detectability) and possibility for PET imaging. Thus, all the radiochemical development processes and pre-treatment dosimetry can be performed with ^{55}Co. Following this, ^{58m}Co productions can then be focused primarily on *in vitro* cytotoxicity and *in vivo* therapy studies in theranostic fashion.

The type 1 neurotensin receptor (NTSR1) was identified as a potentially suitable target for LEE RPT with ^{58m}Co in this work because the neurotensin (NTS)/NTSR1 complex is highly internalizing and can localize near the cell nucleus [116,117,173]. Additionally, NTSR1 is also expressed by a wide variety of cancers including breast, pancreatic, prostate, colon and non-small cell lung cancers due to its role in cellular proliferation, survival and migration [118]. Furthermore, NTS has sub-nanomolar affinity for NTSR1 which potentially enables NTS-derivatives to effectively target cancer cells *in vivo* under radiopharmaceutical conditions [115,173]. Unfortunately, due to rapid degradation of NTS *in vivo*, several modifications are necessary to enhance the metabolic stability for nuclear medicine applications [115,119–121,174,175]. From prior investigations, neurotensin(6-13) with N-methylation at Arg(8), and Tle substitution with Ile(12), “NT-20.3”, achieved one of the best overall targeting properties *in vitro* and *in vivo*, though the molecule was only ~25% stable after circulating for 15 min in mice. More recently, another set of NTSR1 agonists achieved >2x tumor uptake of NT-20.3 around 1 h p.i. [122]. However, these studies did not investigate tumor retention beyond 45 min and the molecules are more difficult to synthesize.

On the other hand, NTSR1 antagonists, such as SR 142948A [150], are not exposed to the same enzymatic cleavage sites as NTS and thus demonstrate high metabolic stability *in vivo* with high binding affinity for NTSR1 [176]. NTSR1 antagonists radiolabeled with ^{177}Lu have improved (preclinical) treatment efficacies as compared to other agonists investigated in literature [124,125] and a phase 1 clinical trial was recently completed (NCT03525392). However, antagonistic targeting vectors often do not internalize to the same degree as agonists due to the lack of downstream cellular signaling after ligand-receptor binding. Despite this, since ^{177}Lu emits electrons that do not benefit from cellular internalization beyond geometrical considerations due to their low initial LET, ^{177}Lu RPT of macroscopic tumors with antagonists generally result in better therapeutic efficacies due to the higher tumor uptake and retention. In fact, tumors at ~mm scale are well-suited to maximize the absorbed dose from electrons emitted by ^{177}Lu. Conversely, the optimal target size for ^{58m}Co RPT is around 20-100 μm and ^{58m}Co internalization can improve the therapeutic window due to increased LET and relatively low range for its emitted electrons. The internalization rate of NTSR1 antagonists is not well established in literature, so there may also be a tradeoff between *in vivo* tumor uptake and *in vitro*-derived cytotoxicity for ^{58m}Co LEE RPT. Nevertheless, because ^{58m}Co emits electrons that have sufficient energy to traverse a cell diameter, cell surface localization may still enhance cytotoxicity and improve the therapeutic window relative to ^{177}Lu.

This chapter investigates the therapeutic potential of both NO2A-NT-20.3 (NT) and NOTA-CB-SR142948A (SR) for LEE RPT targeting NTSR1 using the theranostic ^{55}Co/^{58m}Co matched pair. To simplify notation, NT and SR will refer to the modified NTS agonist and antagonist, respectively. The structure of both molecules is shown in Figure 5-1. The NO2A and NOTA chelating moieties were chosen based on availability and their rapid radiolabeling under mild conditions with n.c.a. ^{55}Co/^{58m}Co. This work begins by radiolabeling ^{55}Co to NT and SR and evaluating the compound's *in vitro* stability against PBS and human serum. Then, the targeting properties are verified *in vitro* by incubating ^{55}Co-radiolabeled NT and SR with NTSR1-positive HT29 cells. The cytotoxicity of ^{58m}Co-labeled NT and SR is then assessed *in vitro*, and ^{55}Co-labeled NT and SR are administered *in vivo* in HT29 tumor-bearing mice for dosimetry analysis. Finally, ^{58m}Co-labeled NT and SR are used for pilot therapy studies to evaluate their therapeutic efficacy.

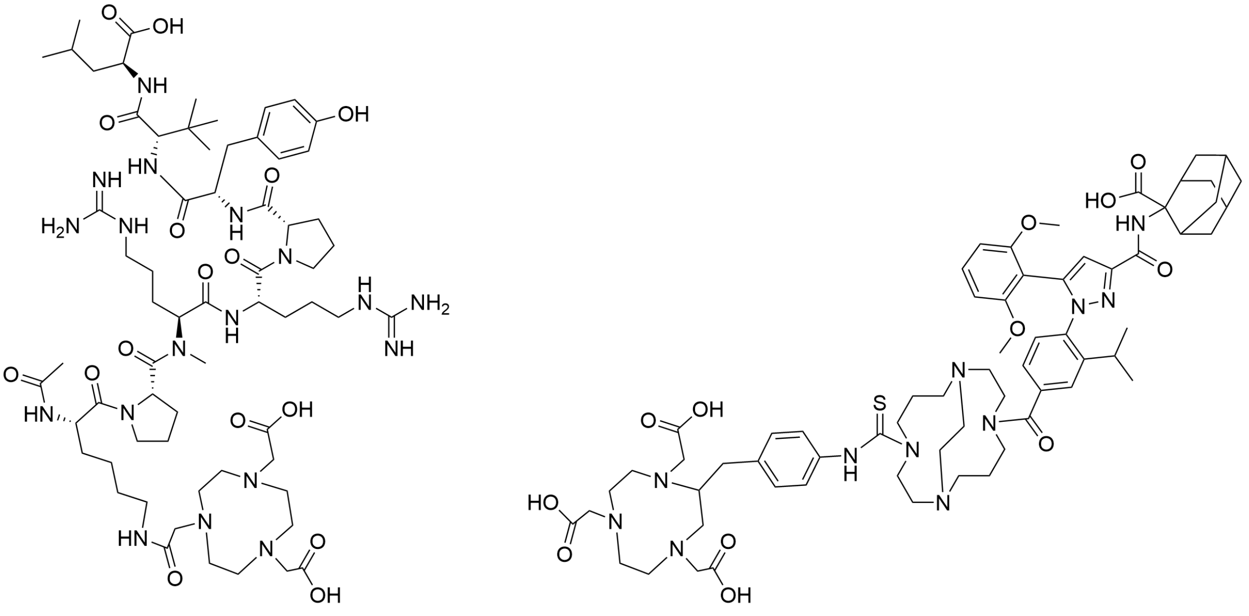

NO2A-NT-20.3 ("NT")

NOTA-CB-SR142948A ("SR")

Figure 5-1 Chemical structures of NO2A-NT-20.3 (NT) and NOTA-CB-SR142948A (SR).

5.1 Materials and methods

5.1.1 Cyclotron production and separation of ^{55}Co and ^{58m}Co

Cobalt-55 and cobalt-58m were produced from deuteron bombardment of isotopically enriched ^{54}Fe and ^{57}Fe, respectively, and processed using the cation exchange/branched-DGA method as described in Chapter 2 or anion exchange/branched-DGA method from [92]. Quantification methods for ^{58m}Co were described in Chapter 2.

5.1.2 Radiolabeling and stability

NO2A-NT-20.3 (NT)

NT was acquired from CPC Scientific by Dr. Lapi's group at the University of Alabama at Birmingham, and lyophilized fractions were sent to UW-Madison. NT was used without further purification and radiolabeled with $^{55/58m}$Co at pH4.5, 95°C for 1 h using 0.1 M pH4.5 sodium acetate buffer and 10 mM sodium gentisate. Radiolabeled compounds were completely oxidized prior to HLB purification. The HLB purification process was described in previous chapters (no TFA addition). All compounds were used within 1 h after purification and AMA for each experiment ranged from 3.7 to 37 MBq/nmol at EOS. Samples were analyzed by radio-HPLC using a reverse-phase 250 x 4.60 mm C18 5μm 100Å column (DIONEX) and the following gradient: 0-3.5min 95% A, 5% B; 3.5-13.5min 95-65% A, 5-35% B; 13.5-15min 65-10% A, 35-90% B; 10% A, 90% B until 19min; 19-20min 10-95% A, 90-5% B; 95% A, 5% B until 25min. A=0.1% TFA H_2O, B=MeCN. To verify the expected mass of Co-NT, 40 nmol NT was labeled with 200 nmol Co under the same conditions as above, then Co-NT was purified by HPLC and sent to University of Wisconsin's Analytical Instrumentation Center for mass spectrometry (Bruker MaXis Ultra-High Resolution Quadrupole Time-of-Flight MS). The *m/z* for $[M+H^+]^{2+}$ and $[M+2H^+]^{3+}$ were 720.36 (expected 720.36) and 480.58 (expected 480.58), respectively, corresponding to a trivalent Co complex as expected from Co redox studies in Chapter 4.

NOTA-CB-SR142948A (SR)

SR was synthesized at the University of North Carolina at Chapel Hill according to recently published methods by Cabrera et al. [144] and used without further purification.

SR was radiolabeled with $^{55/58m}$Co at pH4.5, 55°C for 1 h using 0.1 M pH4.5 sodium acetate buffer and 10 mM sodium gentisate. Radiolabeled compounds were quantitatively oxidized after radiolabeling. All compounds were used within 1 h after purification and AMA for each experiment ranged from 3.7 to 150 MBq/nmol. Samples were analyzed by radio-HPLC (same DIONEX column) using the following gradient: 0-2min 95% A, 5% B; 2-3.5min 95-75% A, 5-25% B; 3.5-25.5min 75-40% A, 25-60% B; 25.5-26min 40-5% A, 60-95% B; 5% A, 90% B until 29min; 29-29.5min 5-95% A, 95-5% B; 95% A, 5% B until 30min. A=0.1% TFA H_2O, B=MeCN.

Human serum stability

All samples had one dominant peak before and after purification. Purified ^{55}Co compounds were incubated with human serum at 37°C then mixed 1:1 with MeCN and centrifuged to remove excess protein prior to HPLC analysis. Most of the activity was present in the supernatant for both compounds.

5.1.3 *In vitro* studies with HT29 cells

HT29 (NTSR1 positive) and Caco2 (NTSR1 negative) human colorectal adenocarcinoma cells (ATCC) were cultured in McCoy's 5A medium and Eagle's Minimum Essential Medium, respectively, with 10% fetal bovine serum and 1% Pen-Strep at 37°C in a 5% CO_2 atmosphere using T75 flasks. Cells were harvested using previously discussed methods. Binding saturation assays were conducted by incubating 10^5 cells/well from sequential dilutions of 200 nM NT radiolabeled with ^{55}Co stock on filtered 96 well plates for 2 h. Filters were drained, rinsed with 3 mL PBS per well, dried and assayed for total bound activity. Binding saturation curves were modeled as one-site total binding ($Y=Bmax*X/(K_D + X)+ NS*X + Background$, where X is the concentration of the ligand). Internalization was assessed by incubating 10^5 HT29 cells in 35 mm petri dishes with 10 nM NT radiolabeled with ^{55}Co, then membrane bound activity was stripped using 0.1 M pH2 sodium citrate/citric acid buffer for 5 min and rinsing with 2 mL PBS. The internalized activity was recovered by dissociating the cells with 1 mL 0.25 % Trypsin-EDTA for >15 min and rinsing with 2 mL PBS. Internalization rates were modeled as one phase exponential association (Y=Plateau*(1-exp(-K*x)), where x is the time in minutes). Subcellular localization assays were performed by first incubating 10^7 HT29 cells with [^{55}Co]Co-NT in T75 flasks for 2 h. Residual membrane bound activity was stripped using 10 mL 0.1 M pH 2 sodium citrate/citric acid buffer for 5 min and rinsed with 3x 10 mL PBS. Cells were dissociated with 3 mL 0.25 % trypsin-EDTA, and centrifuged into a pellet, then cellular contents in each compartment were extracted using a commercially available kit (Thermo Scientific Subcellular Protein Fractionation Kit for Cultured Cells).

MIRDcell V3.12 [78,177] was used to determine HT29 cellular absorbed dose rate per unit activity for ^{58m}Co by assuming a cell radius of 8 μm and nuclear radius of 5 μm [178]. Cobalt-58m transformations [179] were imported into MIRDcell manually. Although MIRDcell V3.12 does not consider contributions from gamma rays and x-rays with the given dimensions, these are negligible for ^{58m}Co at the cellular level. Cytotoxicity was evaluated by incubating [^{58m}Co]Co-NT with 2×10^3 HT29 cells using optical 96 well plates (Thermo Fisher Scientific), where viability was assessed with ATP assays (CellTiter-Glo®, Promega) using a Tecan Spark™ 10 M multi-mode microplate reader. The cytotoxicity was modeled as an inhibitory dose-response ($Y=100/(1+X/IC_{50})$, where X is the (activity) concentration). All model fits and statistical analyses were computed using GraphPad PRISM version 10.1.2 (GraphPad Software). All *in vitro* experiments were performed in triplicate and samples were assayed with an automated gamma-counter (PerkinElmer). The same studies and procedures were performed with [$^{55/58m}$Co]Co-SR. Fit parameters are provided with 68% confidence interval. Unless otherwise stated, reported values are given as mean±SD.

5.1.4 Animal models

General

All animal studies were conducted under a protocol approved by the University of Wisconsin Institutional Animal Care and Use Committee. Food and water were available to mice *ad libitum*. Female athymic nude mice (5–6 weeks old) were purchased from the Jackson Laboratory. HT29 and Caco2 tumors were established by subcutaneous injection of approximately 10^6 cells suspended in 100 µL of 1:1 PBS and Matrigel into the right and left axillary, respectively, of the mice. The xenograft location was chosen to distinguish tumor uptake from kidneys and bladder. *In vivo* experiments were performed once tumor diameters reached ~5 mm (1 week). Mice were inoculated with Caco2 tumors to confirm tracer specificity. Mice for therapeutic studies were not xenografted with Caco2 tumors.

In vivo pharmacokinetics and biodistribution

Pharmacokinetics of Co-labeled NT and SR was determined with *in vivo* PET imaging using [^{55}Co]Co-NT and -SR. *In vivo* PET imaging and *ex vivo* biodistribution were performed following methods from Chapter 3.

In vivo therapy studies using [^{58m}Co]Co-NT and -SR

Prior to therapeutic evaluations with [^{58m}Co]Co-NT/SR, two non-tumor bearing mice were administered approximately 165 MBq of [^{58m}Co]Co-NT/SR to assess general toxicities (euthanized after 3 months). Kidneys were harvested and sectioned for hematoxylin and eosin (H&E) staining and Masson's trichrome to ascertain presence/absence of fibrosis. The treated mice were administered 110 ± 15 MBq [^{58m}Co]Co-NT (N=3, ~3 nmol NT) or 150±10 MBq [^{58m}Co]Co-SR (N=4, ~1 nmol SR). The control groups (N=3 each) received only PBS. As tumors were <6 g throughout the entire experiment, the area method (L × W) was adequate for estimating relative tumor size [180]. Blood samples were acquired from the submandibular vein for complete blood count analysis before and 4 and 8 days after therapy for [^{58m}Co]Co-NT. Mice tumor sizes were measured along two perpendicular axes using a digital caliper and total body weights were determined using a digital scale. Once tumor sizes reached beyond 16 mm, or after 30 days, xenografted mice in the therapy study were euthanized by CO_2 asphyxiation then exsanguinated.

5.1.5 Dosimetry

Dosimetry was assessed via the Medical Internal Radiation Dose (MIRD) formalism [181]. Time-integrated activity in each organ was calculated from the trapezoidal sum of time-activity curves with physical decay of ^{58m}Co or the Bateman fit of ^{58g}Co. Organ uptake beyond 24 h was extrapolated using an exponential decay model from data at 4-24 h. Uncertainty from integrating extrapolated mono-exponential fits were derived using standard error propagation, and uncertainty from fitting was estimated using the confidence interval. Absorbed dose coefficients were calculated by converting time-integrated activity via:

$$d(r_T) = \frac{1}{A_0} \sum_{S} \tilde{A}(r_S) \times S(r_T \leftarrow r_S) \tag{5.1}$$

Where $d(r_T)$ is the absorbed dose coefficient for organ r_T, $\tilde{A}(r_S)$ is the time-integrated activity in organ r_S and $S(r_T \leftarrow r_S)$ is the absorbed dose rate per unit activity for source organ r_S and target organ r_T. The absorbed dose rate per unit activity was assumed to be independent of time. Since the γ dose from ^{58g}Co delivered to off-target tissues are negligible relative to local dose from ^{58g}Co's β+, LEE and LEE from ^{58m}Co, the summation can be simplified to just one term. To quickly convert between units, 1 unit of %ID-h/g is equivalent to 5.77×10^{-3} mGy/MBq-keV (keV in this context refers to the amount of decay energy from a particular radionuclide absorbed by the tissue in keV). The radiation dose to female humans was calculated by scaling the radiation dose to mice with mass ratios [182]. Mouse organ masses were taken from table 3 of [183]. The ^{58g}Co decay energy absorbed in the mouse HT29 tumor, mouse kidney and mouse liver were estimated using GEANT4 [80,184,185] and found to be approximately 37, 43 and 52 keV, respectively. The tissues were assumed to be a sphere of water with radius 2.5, 4.5 and 8.0 mm for the HT29 tumor, kidney (0.38 g) and liver (2.14 g), respectively, and with uniformly distributed activity (10^6 events). The human kidney and liver were assumed to weigh 138 and 1400 g, respectively.

5.2 Results

5.2.1 Radiolabeling and stability of [^{55}Co]Co-NT and [^{55}Co]Co-SR

NT and SR were first analyzed on the HPLC to ascertain their chemical purity. After verifying the chemical purity, and forming the expected Co-NT and -SR complexes, each compound was radiolabeled with ^{55}Co and purified. The samples were then incubated in PBS or human serum at 37°C. Both [^{55}Co]Co-NT and [^{55}Co]Co-SR could be radiolabeled with >95% radiochemical purity and were stable in PBS and human serum for 24 h (Figure 5-2). Due to co-produced ^{57}Co and ^{58g}Co, the radiochemical speciation of ^{58m}Co labeled compounds can be indirectly detected on the radio-HPLC through these surrogates.

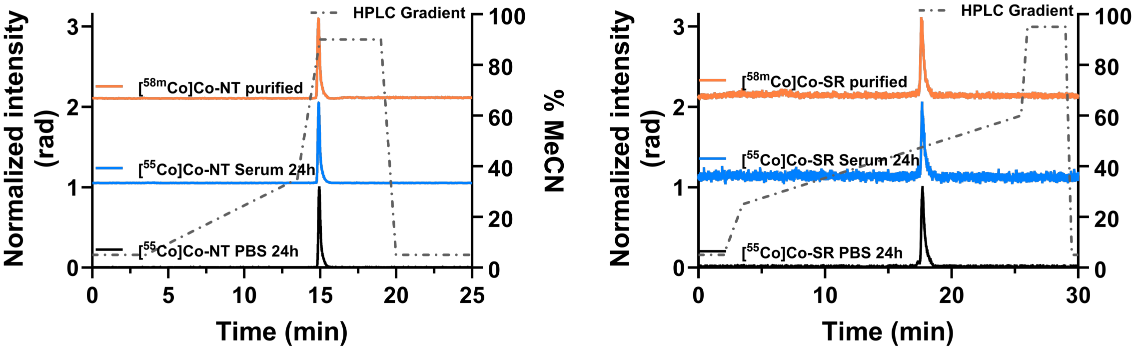

Figure 5-2 Radio-HPLC chromatograms of [^{55}Co]Co-NT (left) and -SR (right) after incubating in PBS and human serum for 24 h. The radio-HPLC chromatograms for [^{58m}Co]Co-NT and -SR after radiolabeling and purification are also included for reference. All samples were oxidized to a single radiochemical species and achieved quantitative labeling prior to purification.

5.2.2 *In vitro* cell assays

Since the ^{5x}Co radiolabeled NT and SR compounds achieved high radiochemical purity and stability in human serum, the targeting properties of each compound were verified by *in vitro* cell assays using NTSR1-positive HT29 cells. Binding saturation assays determined K_D = 5±4 nM (NS 0.06 fmol/nM) and 6±4 nM (NS 1.6 fmol/nM) with NTSR1 density of 1.1±0.2 and 0.7±0.2 x10^{5} per HT29 cell for [^{55}Co]Co-NT and [^{55}Co]Co-SR, respectively (Figure 5-3A). The measured K_D at 2 h and 4 h were similar, which suggests that equilibrium is established after 2 h of incubation. The internalization assays for [^{55}Co]Co-NT and [^{55}Co]Co-SR determined a plateau of 80±5% and 34±2% with K = 3.0±0.5 and 1.7±0.3 x10^{-2} min^{-1}, respectively (Figure 5-3B). Subcellular localization data agrees with qualitative distributions derived from images of fluorescent neurotensin probes in HT29 cells [116,186,187], demonstrating retained targeting properties (Figure 5-3C).

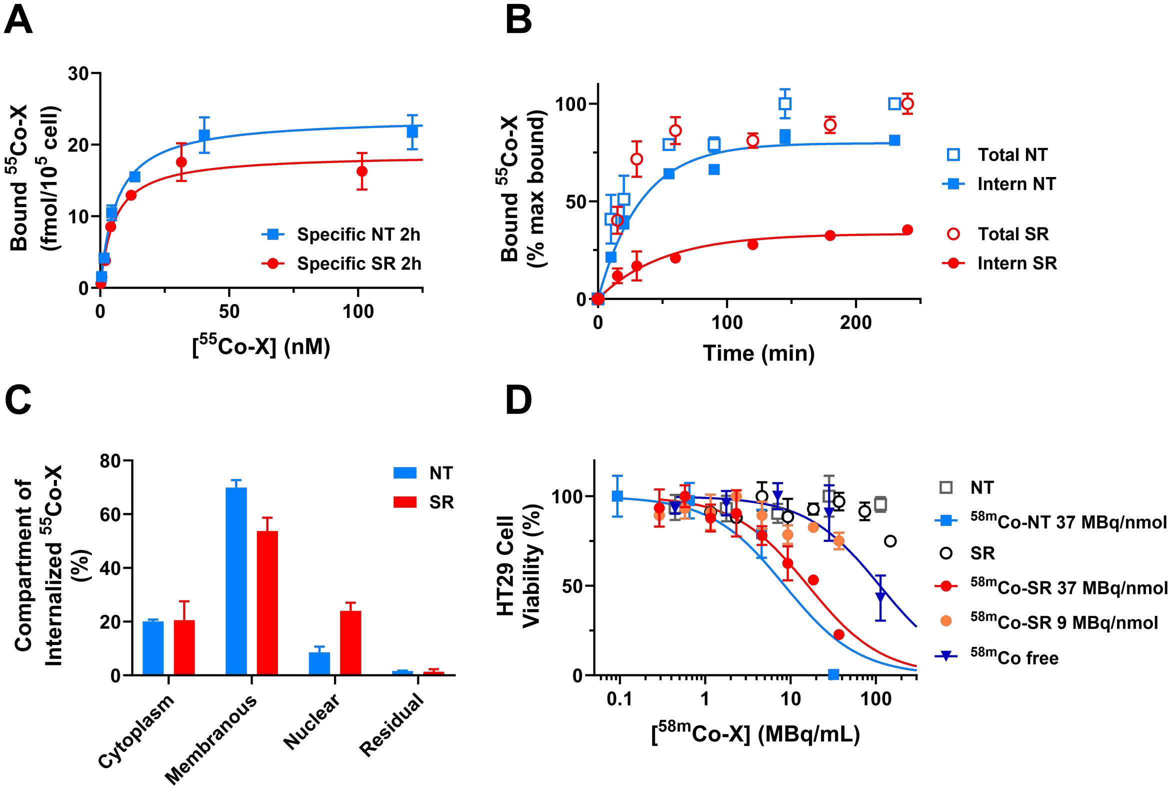

Figure 5-3 In vitro evaluations of A) total binding, B) internalization rate and C) subcellular localization using [^{55}Co]Co-NT and [^{55}Co]Co-SR. D) In vitro viability studies for evaluating the cytotoxicity of [^{58m}Co]Co-NT and [^{58m}Co]Co-SR. The concentration of ligand was set equivalent to that derived from AMA at 37 MBq/nmol. All in vitro experiments used HT29 cells.

After establishing the radiolabeling procedures and validating the targeting properties of ^{55}Co labeled NT and SR, the therapeutic potential of ^{58m}Co was evaluated *in vitro*. [^{58m}Co]Co-NT, [^{58m}Co]Co-SR and [^{58m}Co]CoCl$_2$ induced cytotoxicity in a dose-dependent manner with IC$_{50}$ = 9±2, 16±3 and 110±40 MBq/mL, respectively, after 24 h of incubation (Figure 5-3D). NT and SR did not inhibit cellular proliferation at concentrations matching ^{58m}Co-labeled compounds. Interestingly, [^{58m}Co]Co-SR at lower AMA appeared to exhibit similar behavior as unlabeled ^{58m}Co, though this may also be due to increased [SR]. No statistically significant differences were observed after incubating for 48 h. Using the conversion factor of 0.1889 mJ/MBq with a decayed fraction of 0.839 for ^{58m}Co after 24 h, the dose for [^{58m}Co]Co-NT, [^{58m}Co]Co-SR and [^{58m}Co]CoCl$_2$ at IC$_{50}$ is 1.4±0.3, 2.5±0.5 and 17±6 Gy, respectively. HT29 cellular absorbed dose rate per transformation for ^{58m}Co computed from MIRDcell is provided in Table 1-1, where the same calculations were also performed with ^{177}Lu to demonstrate differences between LEE and (soft) β- emissions. For all scenarios related to self-cell-associated activity, ^{58m}Co delivers >2x dose compared to ^{177}Lu.

Table 5-1 HT29 cellular absorbed dose rate per unit activity for ^{58m}Co and ^{177}Lu calculated from MIRDcell. "C" refers to the cell, "CS"-cell surface, "N"-nucleus, and "Cy"-cytoplasm. For example, C<CS refers to the dose to cell for activity distributed uniformly on the cell surface. HT29 cells were modeled with a nuclear radius of 5 μm and cell radius of 8 μm [178].

	S(C<C) (Gy/Bq-s)	**S(C<CS) (Gy/Bq-s)**	**S(N<N) (Gy/Bq-s)**	**S(N<Cy) (Gy/Bq-s)**	**S(N<CS) (Gy/Bq-s)**	**S(Cy<N) (Gy/Bq-s)**	**S(Cy<CS) (Gy/Bq-s)**	**S(Cy<Cy) (Gy/Bq-s)**
^{58m}Co self	1.03E-03	6.08E-04	3.11E-03	6.83E-04	3.66E-04	6.83E-04	6.87E-04	1.04E-03
^{177}Lu self	2.76E-04	1.73E-04	8.01E-04	1.72E-04	1.01E-04	1.72E-04	1.97E-04	2.88E-04

5.2.3 In vivo PET imaging and dosimetry

Given the promising *in vitro* results, ^{55}Co-labeled NT and SR were administered in mice to evaluate the pharmacokinetics. The biodistribution profile of [^{55}Co]Co-NT is similar to previous work using NT [115], where the compound achieves high tumor-to-background in <1 h p.i. due to fast renal clearance (Figure 5-4). HT29 uptake was >5x Caco2, suggesting tracer specificity. [^{55}Co]Co-NT with higher tracer mass reduced tumor uptake (see Figure 5-5) but retained similar overall biodistribution. Differences in kidney uptake are likely due to erratic voiding periods.

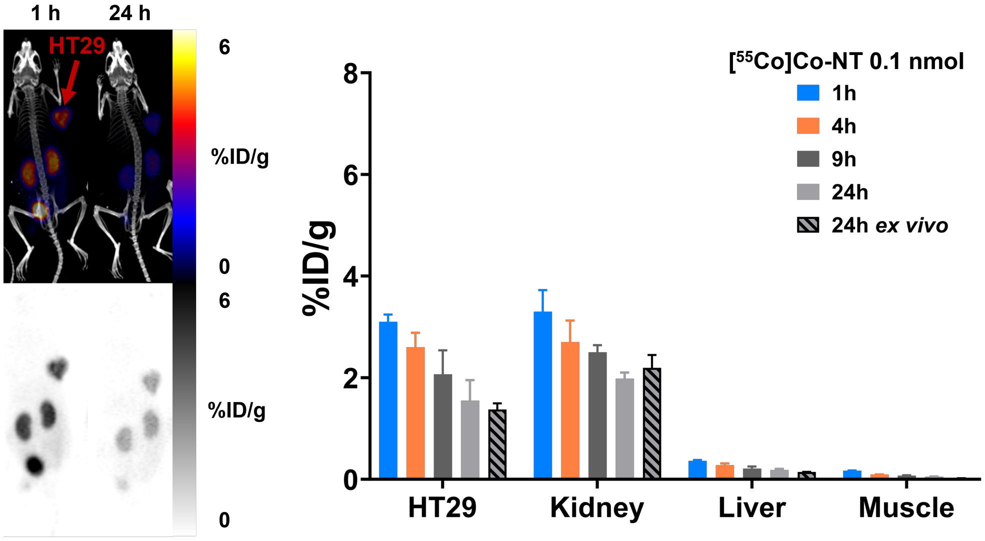

Figure 5-4 In vivo MIP PET/CT (left, top) and PET (left, bottom) images acquired at 1 and 24 h p.i. for [^{55}Co]Co-NT with 0.1 nmol of tracer injected. The arrow indicates the position of HT29 tumor xenograft. PET ROI quantified organ uptake values for select organs agree well with the ex vivo biodistribution at 24 h (right).

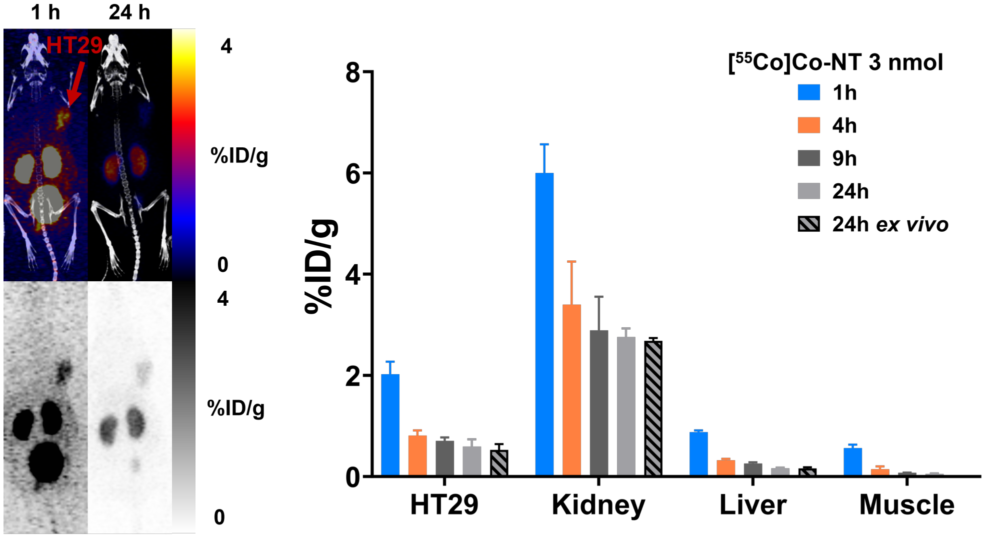

Figure 5-5 In vivo MIP PET/CT (left, top) and PET (left, bottom) images acquired at 1 and 24 h p.i. for [^{55}Co]Co-NT with 3 nmol of tracer injected. The arrow indicates the position of HT29 tumor xenograft. PET ROI quantified organ uptake values for select organs agree well with the ex vivo biodistribution at 24 h (right).

On the other hand, [^{55}Co]Co-SR exhibits a combination of hepatobiliary and renal clearance with high tumor uptake and tumor-to-background (Figure 5-6). Again, HT29 uptake was >10x Caco2, which suggests tracer specificity to NTSR1. Similarly, the tumor uptake is reduced with higher tracer mass but the overall biodistribution profile remains comparable (Figure 5-7). Even with the drastic reduction in HT29 tumor uptake with 1 nmol SR, [^{55}Co]Co-SR achieves substantially greater tumor uptake compared to [^{55}Co]Co-NT. Figure 5-8 shows the *ex vivo* biodistribution at 24 h p.i. for all groups of mice investigated in this work.

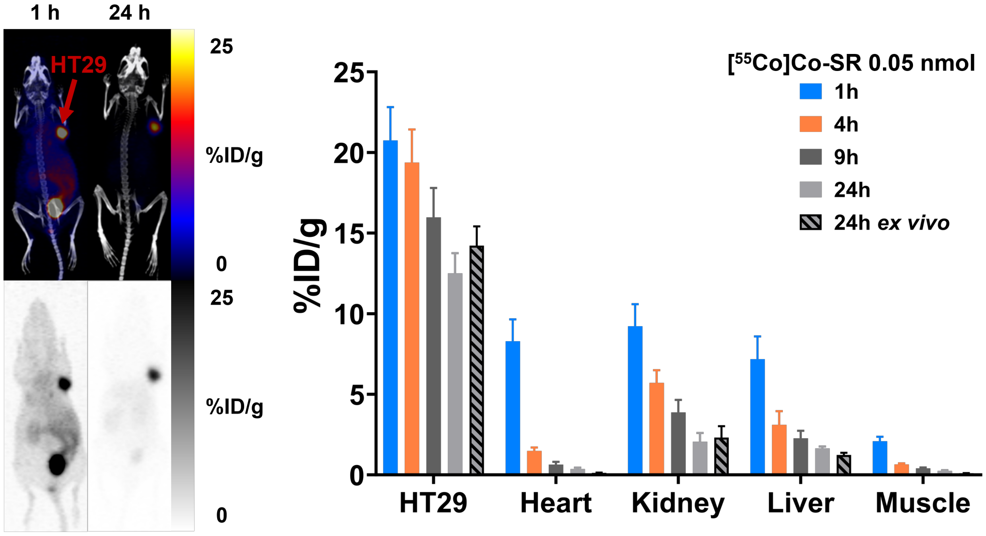

Figure 5-6 In vivo MIP PET/CT (left, top) and PET (left, bottom) images acquired at 1 and 24 h p.i. for [^{55}Co]Co-SR with 0.05 nmol of tracer injected. The arrow indicates the position of HT29 tumor xenograft. PET ROI quantified organ uptake values for select organs agree well with the ex vivo biodistribution at 24 h (right).

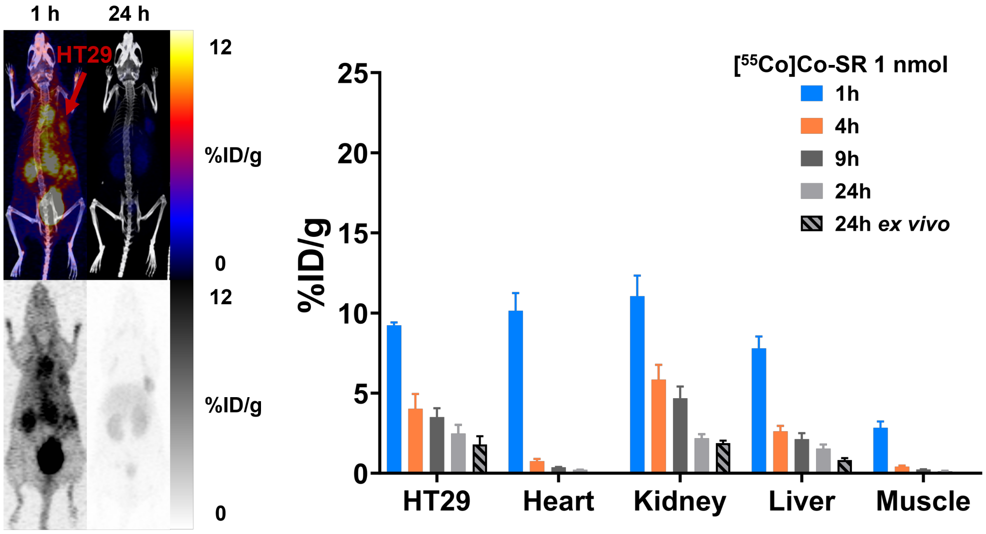

Figure 5-7 In vivo MIP PET/CT (left, top) and PET (left, bottom) images acquired at 1 and 24 h p.i. for [^{55}Co]Co-SR with 1 nmol of tracer injected. The arrow indicates the position of HT29 tumor xenograft. PET ROI quantified organ uptake values for select organs agree well with the ex vivo biodistribution at 24 h (right).

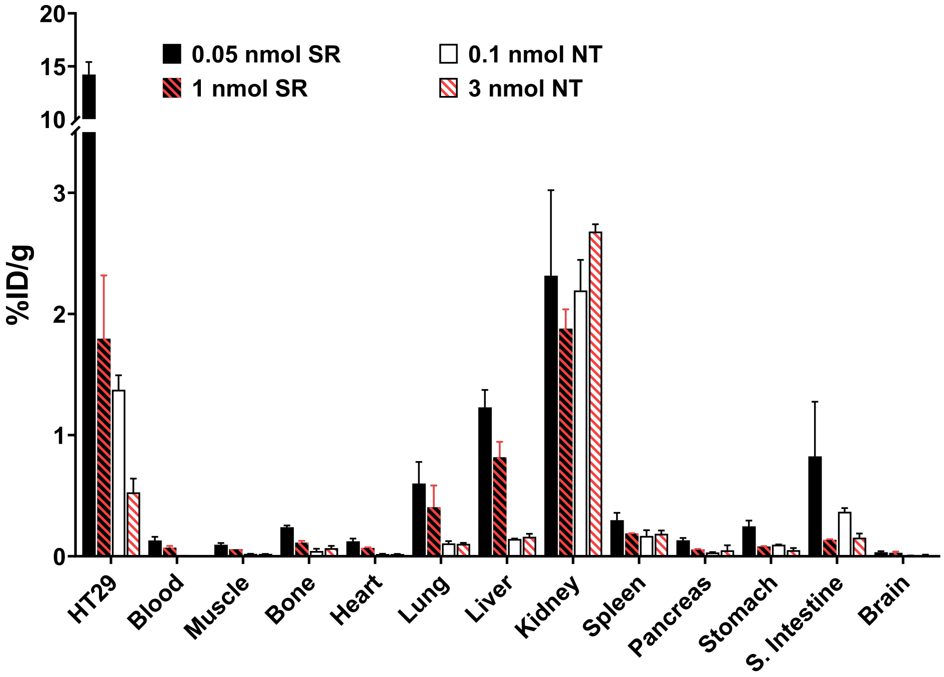

Figure 5-8 Ex vivo biodistribution at 24 h p.i. for [^{55}Co]Co-NT and -SR with low and high tracer masses.

After acquiring the *in vivo* pharmacokinetic profile of [^{55}Co]Co-NT and -SR, dosimetry for organs of interest were then calculated by substituting the physical properties of ^{55}Co with ^{58m}Co since the two radionuclides are chemically matched. Using the MIRD formalism, dosimetry for [^{58m}Co]Co-NT and [^{58m}Co]Co-SR are presented in Table 5-2 and Table 5-3, respectively. Although both [^{58m}Co]Co-NT and [^{58m}Co]Co-SR deliver more dose to the kidneys compared to the HT29 tumor, [^{58m}Co]Co-SR can achieve nearly 5x higher absorbed dose per unit activity to the tumor compared to [^{58m}Co]Co-NT.

Table 5-2 Calculated mass-normalized time-integrated relative activity ($\tilde{A}/A_0$ ×100%/M) for [^{58m}Co]Co-NT with 3 nmol NT from integrating time-activity curves and absorbed dose coefficients (d) for organs of interest.

Organ	$\frac{\tilde{A}}{A_0} \times 100\%/M$ (%ID-h/g) ^{58m}Co	$\frac{\tilde{A}}{A_0} \times 100\%/M$ (%ID-h/g) ^{58g}Co	d Mouse (mGy/MBq) ^{58m}Co/^{58g}Co*	d Human (µGy/MBq) ^{58m}Co/^{58g}Co*
HT29 Tumor	11 ± 1	0.54 ± 0.31	1.6/0.12	N/A
Kidney	43 ± 4	3.4 ± 1.2	6.1/0.84	2.0/0.28
Liver	4.1 ± 0.5	0.11 ± 0.06	0.58/0.03	0.19/0.01

*^{58g}Co contributions are stated per MBq of [^{58m}Co]Co-NT with 0.96% ^{58g}Co.

Table 5-3 Calculated mass-normalized time-integrated relative activity ($\tilde{A}/A_0$ ×100%/M) for [^{58m}Co]Co-SR with 1 nmol SR from integrating time-activity curves and absorbed dose coefficients (d) for organs of interest.

Organ	$\frac{\tilde{A}}{A_0} \times 100\%/M$ (%ID-h/g) ^{58m}Co	$\frac{\tilde{A}}{A_0} \times 100\%/M$ (%ID-h/g) ^{58g}Co	d Mouse (mGy/MBq) ^{58m}Co/^{58g}Co*	d Human (µGy/MBq) ^{58m}Co/^{58g}Co*
HT29 Tumor	50 ± 6	2.6 ± 1.1	7.2/0.55	N/A
Kidney	61 ± 6	2.1 ± 0.5	8.7/0.51	2.9/0.17
Liver	35 ± 4	1.6 ± 0.7	5.0/0.48	1.7/0.16

*^{58g}Co contributions are stated per MBq of [^{58m}Co]Co-SR with 1.4% ^{58g}Co.

5.2.4 Pilot in vivo therapy studies

Following *in vivo* PET imaging studies, 110 MBq [^{58m}Co]Co-NT (0.2 Gy to tumor, 3 nmol NT) and 130 MBq [^{58m}Co]Co-SR (0.9 Gy to tumor, 1 nmol SR) were administered per tumor-bearing mouse to evaluate the therapeutic potential of ^{58m}Co *in vivo*. In parallel, mice with no tumors were administered 165 MBq [^{58m}Co]Co-NT and 150 MBq [^{58m}Co]Co-SR to assess long-term toxicities associated with the treatment. These activities were set based on the production capacity, AMA and losses due to purification and residual activity in the syringe injection (>20% for [^{58m}Co]Co-SR). A total of 450-690 MBq and 740-925 MBq ^{58m}Co at EOB were produced for [^{58m}Co]Co-NT and [^{58m}Co]Co-SR, respectively.

[^{58m}Co]Co-SR treated mice with 1 nmol of SR were taken for PET imaging and the results corroborate with [^{55}Co]Co-SR under similar conditions (Figure 5-9). These results demonstrate the utility of using chemically matched theranostic pairs. [^{58m}Co]Co-NT treated mice were not taken for PET imaging due to low expected counting statistics. The relative tumor size and total body weight for each group of mice after treatment with [^{58m}Co]Co-SR is presented in Figure 5-10. Although treatment with either [^{58m}Co]Co-NT or [^{58m}Co]Co-SR did not lead to a meaningful therapeutic response, no toxicities were observed (blood count and body mass). The treated mice with no tumors received 1.0 ([^{58m}Co]Co-NT) and 1.3 Gy ([^{58m}Co]Co-SR) to the kidneys and had no observable renal damage (Figure 5-11).

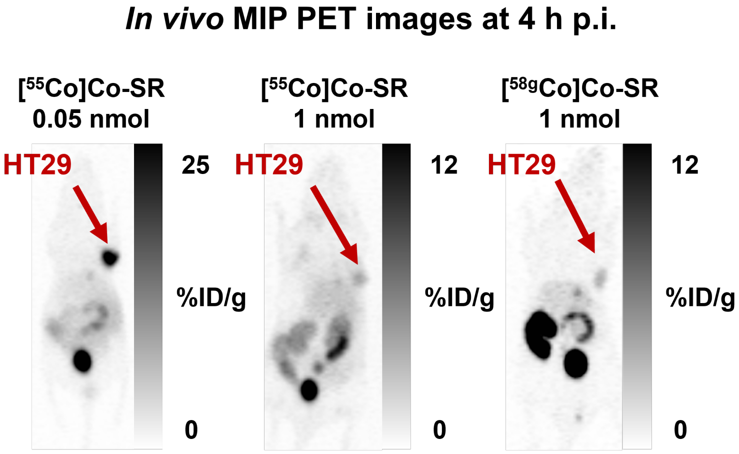

Figure 5-9 In vivo MIP PET images acquired at 4 h p.i. for [^{55}Co]Co-SR with 0.05 nmol (left) and 1 nmol (middle) of SR. Due to the improved metabolic stability, It was also possible to image [^{58g}Co]Co-SR present in [^{58m}Co]Co-SR treated mice with acceptable counting statistics (right). The arrow indicates the position of HT29 tumor xenograft.

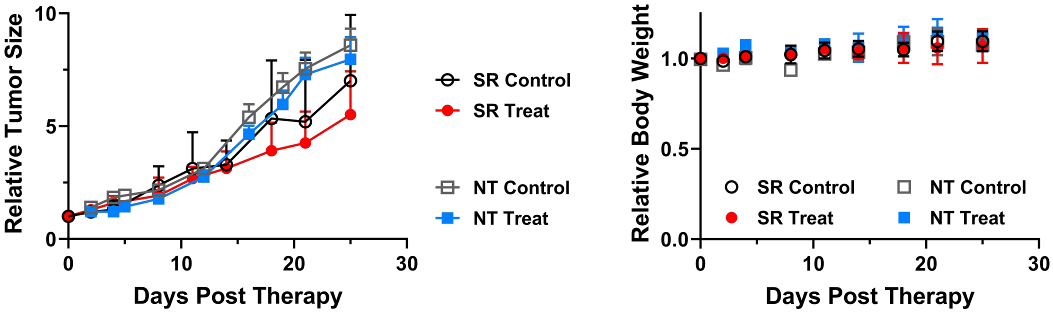

Figure 5-10 The relative tumor size of mice after treatment (left) and the respective body weights (right) for each group. Mice in the control group received no ^{58m}Co and only PBS.

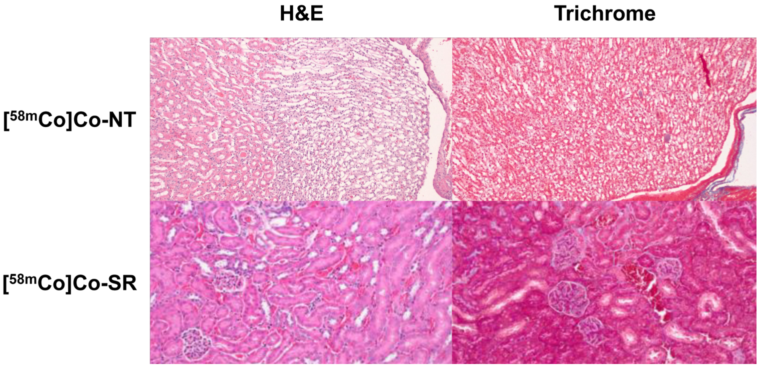

Figure 5-11 Representative mouse kidney slices stained with hematoxylin and eosin (H&E) and Masson's trichrome demonstrate normal tissue morphology in the kidneys after treatment with 165 MBq of [^{58m}Co]Co-NT and [^{58m}Co]Co-SR. Dr. Andres Mejia kindly performed the staining and histology analysis.

5.3 Discussion

The improved separation procedure from Chapter 2 enables the purified ^{58m}Co to achieve NOTA AMA of 150 MBq/nmol at EOS ([^{58m}Co]Co-SR). At the time of writing this section, this is the highest reported [^{58m}Co]Co-NOTA AMA in literature. The most recent publication with [^{58m}Co]Co-DO3A-PSMA-617 radiolabeled 1.6 GBq ^{58m}Co at 84 MBq/nmol EOS [88]. For reference, [^{55}Co]Co-DOTA AMA from Chapter 2 was 35 MBq/nmol with EOB production of ~0.25 GBq ^{55}Co. Although the authors did not explicitly mention the ^{58m}Co activity at EOB, they likely produced >2x ^{58m}Co compared to this work (max of 0.93 GBq at EOB). It is also worth noting that those researchers had access to >99% ^{58}Fe which can achieve higher ^{58m}Co yields as discussed in Chapter 1.

Since both compounds were conjugated with NOxA-based chelators, the compounds were ascertained to be one radiochemical species prior to *in vitro* and *in vivo* studies. Although MS was not successfully acquired with Co-SR, due to low ionization and concentration, results from Chapter 4 suggest ^{55}Co likely exists in the trivalent oxidation state after radiolabeling to SR under n.c.a. conditions. Based on MS results, Co-NT retained Co(III) after heating with GA at pH4.5, which corroborates Co-NO2A results from Chapter 4. The improved AMA for [^{58m}Co]Co-SR over [^{58m}Co]Co-NT is likely due to increased ^{58m}Co production and transitioning to the cation exchange/extraction chromatography method. Both [^{55}Co]Co-NT and [^{55}Co]Co-SR demonstrated good stability in PBS and human serum for >24 h. GA also helped reduce SR degradation from radiolysis.

The *in vitro* assays demonstrated that [^{58m}Co]Co-NT and [^{58m}Co]Co-SR retained their targeting properties for NTSR1-positive HT29 cells. Experimentally derived K_D for both compounds were ~5 nM, and the NTSR1 expression was comparable with other work [123]. The internalization assays showed that [^{58m}Co]Co-NT internalized faster and achieved ~2.5x greater internalization of cell-associated activity as compared to [^{58m}Co]Co-SR. Since SR does not induce agonistic effects upon binding to NTSR1 [150], the internalization of [^{58m}Co]Co-SR is likely due to changes in NTSR1 conformation after complexation with SR [188,189]. Both [^{58m}Co]Co-NT and [^{58m}Co]Co-SR were significantly more cytotoxic than [^{58m}Co]CoCl$_2$, and [^{58m}Co]Co-NT was more cytotoxic than [^{58m}Co]Co-SR by nearly 2x ($p=0.0063$). Enhanced cytotoxicity of

[^{58m}Co]Co-NT is expected because internalized ^{58m}Co delivers ~2x more dose to the cell and nucleus compared to surface bound activity (see Table 1-1). In fact, NT was chosen as a promising targeting vector for ^{58m}Co due to this consideration. Interestingly, the cytotoxicity of [^{58m}Co]Co-SR set at 9 MBq/nmol was significantly lower compared to 37 MBq/nmol, which suggests that receptor saturation reduces the cytotoxicity. Results in this work demonstrate that future cytotoxicity assays with targeted ^{58m}Co radiopharmaceuticals should aim to incubate cells starting at ~100 MBq/mL and sequentially dilute each of 7 wells by a factor of ~2x to achieve a good fit to the data. The AMA should also be varied to assess potential receptor saturation effects, though one should be mindful of potential cytotoxic effects from increased tracer concentration.

Due to the relatively low NTSR1 receptor density, each compound was evaluated by PET imaging in two groups of mice: one with low tracer mass and the other with tracer mass equal to the expected treatment dose. The overall biodistribution profile was similar between the low and high tracer mass groups but the tumor uptake for both compounds was substantially reduced with higher tracer mass. Although the *in vivo* therapy studies did not lead to a therapeutically meaningful response over time, there was no observed general toxicity associated with the treatment (blood count, mass, kidney histology). The absorbed dose coefficient for the HT29 tumor is 29 mGy/MBq for the 0.05 nmol SR group which is about 4x that of the 1 nmol SR group (with similar kidney and liver values between the two groups) and 6x that of the 0.10 nmol NT group. Despite needing more research to establish the optimal mass of tracer prior to NTSR1 saturation, the most critical consideration is to improve ^{58m}Co AMA for tumor models with relatively low receptor expression. The level of NTSR1 expression for HT29 cells may not be suitable for short-lived LEE emitters such as ^{58m}Co unless the AMA is >370 MBq/nmol, which results in a theoretical maximum of 12 Gy to tumor in one cycle for 10^5 receptors/cell and 10^9 cells/cm^3 (assuming complete retention of 61 MBq/g ^{58m}Co in the tumor and immediate uptake).

With all else equal, the AMA can be improved by increasing the production capacity, though increasing the irradiation time will produce more ^{57}Co and ^{58g}Co as a fraction of ^{58m}Co. Irradiating thick targets with larger diameter will improve on-target irradiation but the separation method will likely need to be optimized to accommodate larger masses. The costliest approach would be to buy ^{58}Fe and acquire an accelerator capable of delivering deuterons at higher energy and current. Alternative separation methods may improve the AMA, but both high AMA and production yields are simultaneously needed to effectively apply ^{58m}Co for RPT. For example, delivering 10 Gy to the tumor will require 345 MBq [^{58m}Co]Co-SR per mouse (assuming dosimetry from 0.05 nmol SR). After accounting for 85% separation yield, 80% radiochemical yield after purification/residual in syringe and 4 h of decay, this results in a minimum production of 2 GBq ^{58m}Co for treating only 3 mice. Focusing the attention now to [^{58m}Co]Co-NT, due to potentially enhanced therapeutic window from high internalization, the tumor-to-kidney ratio is 0.8 with an expected 5 mGy/MBq to the HT29 tumor in mice (assuming dosimetry from 0.1 nmol NT group). Using the controversial 23 Gy dose limit for the kidneys, this implies only 18 Gy can be delivered to the HT29 tumor and requires a total of 3.6 GBq [^{58m}Co]Co-NT (in multiple cycles since ^{58m}Co is theoretically limited at ~13 GBq/nmol). The treatment in this case will likely not be limited by the tumor burden because most of the activity is renally cleared in <1 h, though a max tumor uptake of

~5%ID/g implies 20 g of tumor(s) will deplete the tracer (assuming no other losses). Based on yield calculations presented in Figure 1-14, irradiating ~200 μm ^{58}Fe with 15 MeV deuterons can produce ~500 MBq/μAh ^{58m}Co, which is 56 GBq ^{58m}Co EOB following irradiation with 60 μA deuterons for 2 h (including saturation). Cobalt-58m from this reaction pathway is predicted to have <0.6% ^{58g}Co (<340 MBq) with negligible ^{57}Co at EOB, where ^{58g}Co dose contribution can be further modulated by the pharmacokinetics.

Alternatively, the constraints on production capacity and AMA can be less stringent if better targets and targeting vectors are considered. In comparison with prostate cancer models, the PSMA-positive PC3-PIP cells typically have 10^6 receptors/cell which is about an order of magnitude greater than NTSR1 receptors expressed by HT29 cells. This simple change in tumor model reduces the above constraint on AMA to just >37 MBq/nmol. Furthermore, the myriad of PSMA targeting vectors available in literature with exceptional tumor uptake and retention (e.g., [137,190,191] and Chapter 4) make PSMA an outstanding target even in comparison with SSTR2 [86]. In fact, preliminary *in vivo* therapy studies using [^{58m}Co]Co-DO3A-PSMA-617 was recently published with promising results [88].

5.4 Conclusion

[$^{55/58m}$Co]Co-NT and [$^{55/58m}$Co]Co-SR were synthesized with radiochemical purity suitable for *in vivo* applications. *In vitro* and *in vivo* experiments demonstrate that [$^{55/58m}$Co]Co-NT and [$^{55/58m}$Co]Co-SR retained the targeting properties of each respective tracer. Although SR is more metabolically stable than NT, cytotoxicity assays revealed that [^{58m}Co]Co-NT is likely more potent than [^{58m}Co]Co-SR, presumably due to higher internalization. Given the low NTSR1 expression for HT29 cells, receptor saturation from higher tracer mass likely reduced tumor uptake. Dosimetry analysis showed that ^{58g}Co is negligible if the tracer has a short biological half-life. Although no therapeutically meaningful response was observed after treatment with 110 MBq of [^{58m}Co]Co-NT and 130 MBq [^{58m}Co]Co-SR, there was no observed toxicity in any treated group, including those that received 165 MBq. Higher time-integrated activity and/or multiple dosing regimens will be necessary for ^{58m}Co-labeled radiopharmaceuticals to achieve observable therapeutic responses. The development of novel PSMA-targeting probes for ^{58m}Co is currently ongoing.

Conclusion

The information presented in this dissertation serves to elucidate the behavior of Co radiopharmaceuticals and facilitate their application. During my degree, I substantially reduced the fabrication time for iron electrodeposition [131], developed an efficient method for separating cyclotron produced ^{5x}Co from ^{5x}Fe targets [192], explored the radiolabeling parameters for novel [^{55}Co]Co-Sar complexes [193], demonstrated the chemical redox speciation of Co-NO2A, -NOTA and -DO3A complexes (manuscript under review) and implemented ^{55}Co/^{58m}Co for theranostic RPT applications [90,132,144]. Future work with ^{55}Co/^{58m}Co could include automating the separation process, performing systematic comparisons of Co-Sar radiopharmaceuticals with Cu, exploiting the redox activity of Co complexes and/or treating tumors with ^{58m}Co radiopharmaceuticals that have even better tumor targeting properties than PSMA-617. Surveying the publications related to ^{55}Co/^{58m}Co since 2011 (first ^{58m}Co publication with relevance for RPT) and excluding those that I was a part of, only 14 publications have applied ^{55}Co/^{58m}Co suitable for RPT [87,88,91–94,114,137,162,163,194–197]. By the time this document is accessible, I will have contributed 6 additional original articles in this area. Given the recent positive treatment results from [^{58m}Co]Co-DO3A-PSMA-617, I also anticipate increased interest in using ^{58m}Co for RPT and I look forward to future developments using the ^{55}Co/^{58m}Co theranostic pair. It was truly a unique experience to explore nearly all facets of isotope production and application, including nuclear cross section measurements, neutron spectrum unfolding and concrete shielding simulations (see Appendix A-C), and none of this would have been possible without the enthusiastic support of my lab, advisor and wonderful collaborators.

References:

[1] Neelapu SS, Tummala S, Kebriaei P, Wierda W, Gutierrez C, Locke FL, et al. Chimeric antigen receptor T-cell therapy — assessment and management of toxicities. Nat Rev Clin Oncol 2018;15:47–62. https://doi.org/10.1038/nrclinonc.2017.148.

[2] Brudno JN, Lam N, Vanasse D, Shen Y, Rose JJ, Rossi J, et al. Safety and feasibility of anti-CD19 CAR T cells with fully human binding domains in patients with B-cell lymphoma. Nat Med 2020;26:270–80. https://doi.org/10.1038/s41591-019-0737-3.

[3] Esfahani K, Roudaia L, Buhlaiga N, Del Rincon SV, Papneja N, Miller WH. A Review of Cancer Immunotherapy: From the Past, to the Present, to the Future. Current Oncology 2020;27:87–97. https://doi.org/10.3747/co.27.5223.

[4] Grosser R, Cherkassky L, Chintala N, Adusumilli PS. Combination Immunotherapy with CAR T Cells and Checkpoint Blockade for the Treatment of Solid Tumors. Cancer Cell 2019;36:471–82. https://doi.org/10.1016/j.ccell.2019.09.006.

[5] Baah S, Laws M, Rahman KM. Antibody–Drug Conjugates—A Tutorial Review. Molecules 2021;26:2943. https://doi.org/10.3390/molecules26102943.

[6] Buchbinder EI, Desai A. CTLA-4 and PD-1 Pathways. Am J Clin Oncol 2016;39:98–106. https://doi.org/10.1097/COC.0000000000000239.

[7] Kaczmarek M, Poznańska J, Fechner F, Michalska N, Paszkowska S, Napierała A, et al. Cancer Vaccine Therapeutics: Limitations and Effectiveness—A Literature Review. Cells 2023;12:2159. https://doi.org/10.3390/cells12172159.

[8] Baskar R, Lee KA, Yeo R, Yeoh K-W. Cancer and Radiation Therapy: Current Advances and Future Directions. Int J Med Sci 2012;9:193–9. https://doi.org/10.7150/ijms.3635.

[9] Hanahan D, Weinberg RA. Hallmarks of Cancer: The Next Generation. Cell 2011;144:646–74. https://doi.org/10.1016/j.cell.2011.02.013.

[10] Hanahan D. Hallmarks of Cancer: New Dimensions. Cancer Discovery 2022;12:31–46. https://doi.org/10.1158/2159-8290.CD-21-1059.

[11] Chen HHW, Kuo MT. Improving radiotherapy in cancer treatment: Promises and challenges. Oncotarget 2017;8:62742–58. https://doi.org/10.18632/oncotarget.18409.

[12] Olivares-Urbano MA, Griñán-Lisón C, Marchal JA, Núñez MI. CSC Radioresistance: A Therapeutic Challenge to Improve Radiotherapy Effectiveness in Cancer. Cells 2020;9:1651. https://doi.org/10.3390/cells9071651.

[13] Baumann M, Krause M, Overgaard J, Debus J, Bentzen SM, Daartz J, et al. Radiation oncology in the era of precision medicine. Nat Rev Cancer 2016;16:234–49. https://doi.org/10.1038/nrc.2016.18.

[14] Brown A, Suit H. The centenary of the discovery of the Bragg peak. Radiotherapy and Oncology 2004;73:265–8. https://doi.org/10.1016/j.radonc.2004.09.008.

[15] Paganetti H. Range uncertainties in proton therapy and the role of Monte Carlo simulations. Phys Med Biol 2012;57:R99–117. https://doi.org/10.1088/0031-9155/57/11/R99.

[16] Koketsu J, Kumada H, Takada K, Takei H, Mori Y, Kamizawa S, et al. 3D-printable lung phantom for distal falloff verification of proton Bragg peak. J Appl Clin Med Phys 2019;20:86–94. https://doi.org/10.1002/acm2.12706.

[17] Suwa T, Kobayashi M, Nam J-M, Harada H. Tumor microenvironment and radioresistance. Exp Mol Med 2021;53:1029–35. https://doi.org/10.1038/s12276-021-00640-9.

[18] Chargari C, Deutsch E, Blanchard P, Gouy S, Martelli H, Guérin F, et al. Brachytherapy: An overview for clinicians. CA: A Cancer Journal for Clinicians 2019;69:386–401. https://doi.org/10.3322/caac.21578.

[19] Herskovic A, Martz K, Al-Sarraf M, Leichman L, Brindle J, Vaitkevicius V, et al. Combined Chemotherapy and Radiotherapy Compared with Radiotherapy Alone in Patients with Cancer of the Esophagus. New England Journal of Medicine 1992;326:1593–8. https://doi.org/10.1056/NEJM199206113262403.

[20] Begg AC, Stewart FA, Vens C. Strategies to improve radiotherapy with targeted drugs. Nat Rev Cancer 2011;11:239–53. https://doi.org/10.1038/nrc3007.

[21] Majidpoor J, Mortezaee K. Steps in metastasis: an updated review. Med Oncol 2021;38:3. https://doi.org/10.1007/s12032-020-01447-w.

[22] Ganesh K, Massagué J. Targeting metastatic cancer. Nat Med 2021;27:34–44. https://doi.org/10.1038/s41591-020-01195-4.

[23] Mukherjee M, Levine H. Cluster size distribution of cells disseminating from a primary tumor. PLoS Comput Biol 2021;17:e1009011. https://doi.org/10.1371/journal.pcbi.1009011.

[24] Schuster E, Taftaf R, Reduzzi C, Albert MK, Romero-Calvo I, Liu H. Better together: circulating tumor cell clustering in metastatic cancer. Trends in Cancer 2021;7:1020–32. https://doi.org/10.1016/j.trecan.2021.07.001.

[25] Mavrogenis AF, Angelini A, Vottis C, Pala E, Calabrò T, Papagelopoulos PJ, et al. Modern Palliative Treatments for Metastatic Bone Disease. The Clinical Journal of Pain 2016;32:337–50. https://doi.org/10.1097/AJP.0000000000000255.

[26] Dillekås H, Rogers MS, Straume O. Are 90% of deaths from cancer caused by metastases? Cancer Med 2019;8:5574–6. https://doi.org/10.1002/cam4.2474.

[27] Incidence and Relative Survival by Stage at Diagnosis for Common Cancers | CDC 2023. https://www.cdc.gov/cancer/uscs/about/data-briefs/no25-incidence-relative-survival-stage-diagnosis.htm (accessed January 8, 2024).

[28] Hennrich U, Kopka K. Lutathera®: The First FDA- and EMA-Approved Radiopharmaceutical for Peptide Receptor Radionuclide Therapy. Pharmaceuticals 2019;12:114. https://doi.org/10.3390/ph12030114.

[29] Hennrich U, Eder M. [^{177}Lu]Lu-PSMA-617 (PluvictoTM): The First FDA-Approved Radiotherapeutical for Treatment of Prostate Cancer. Pharmaceuticals (Basel) 2022;15:1292. https://doi.org/10.3390/ph15101292.

[30] Jang A, Kendi AT, Johnson GB, Halfdanarson TR, Sartor O. Targeted Alpha-Particle Therapy: A Review of Current Trials. International Journal of Molecular Sciences 2023;24:11626. https://doi.org/10.3390/ijms241411626.

[31] Healy A, Ho E, Kuo P, Zukotynski K. A brief overview of targeted radionuclide therapy trials in 2022. Frontiers in Nuclear Medicine 2023;3.

[32] Liston DR, Davis M. Clinically relevant concentrations of anticancer drugs: A guide for nonclinical studies. Clin Cancer Res 2017;23:3489–98. https://doi.org/10.1158/1078-0432.CCR-16-3083.

[33] Heiland S, Erb G, Ziegler S, Krix M. Where Contrast Agent Concentration Really Matters – A Comparison of CT and MRI. Investigative Radiology 2010;45:529. https://doi.org/10.1097/RLI.0b013e3181ea703d.

[34] Patel RB, Hernandez R, Carlson P, Grudzinski J, Bates AM, Jagodinsky JC, et al. Low-dose targeted radionuclide therapy renders immunologically cold tumors responsive to immune checkpoint blockade. Science Translational Medicine 2021;13:eabb3631. https://doi.org/10.1126/scitranslmed.abb3631.

[35] Suman SK, Subramanian S, Mukherjee A. Combination radionuclide therapy: A new paradigm. Nuclear Medicine and Biology 2021;98–99:40–58. https://doi.org/10.1016/j.nucmedbio.2021.05.001.

[36] Shah HJ, Ruppell E, Bokhari R, Aland P, Lele VR, Ge C, et al. Current and upcoming radionuclide therapies in the direction of precision oncology: A narrative review. European Journal of Radiology Open 2023;10:100477. https://doi.org/10.1016/j.ejro.2023.100477.

[37] Miller C, Rousseau J, Ramogida CF, Celler A, Rahmim A, Uribe CF. Implications of physics, chemistry and biology for dosimetry calculations using theranostic pairs. Theranostics 2022;12:232–59. https://doi.org/10.7150/thno.62851.

[38] Rösch F, Herzog H, Qaim SM. The Beginning and Development of the Theranostic Approach in Nuclear Medicine, as Exemplified by the Radionuclide Pair ^{86}Y and ^{90}Y. Pharmaceuticals (Basel) 2017;10. https://doi.org/10.3390/ph10020056.

[39] Jong M de, Breeman WAP, Valkema R, Bernard BF, Krenning EP. Combination Radionuclide Therapy Using ^{177}Lu- and ^{90}Y-Labeled Somatostatin Analogs. Journal of Nuclear Medicine 2005;46:13S-17S.

[40] Valkema R, Pauwels SA, Kvols LK, Kwekkeboom DJ, Jamar F, Jong M de, et al. Long-Term Follow-Up of Renal Function After Peptide Receptor Radiation Therapy with ^{90}Y-DOTA0,Tyr3-Octreotide and ^{177}Lu-DOTA0, Tyr3-Octreotate. Journal of Nuclear Medicine 2005;46:83S-91S.

[41] Müller C, Umbricht CA, Gracheva N, Tschan VJ, Pellegrini G, Bernhardt P, et al. Terbium-161 for PSMA-targeted radionuclide therapy of prostate cancer. Eur J Nucl Med Mol Imaging 2019;46:1919–30. https://doi.org/10.1007/s00259-019-04345-0.

[42] Borgna F, Haller S, Rodriguez JMM, Ginj M, Grundler PV, Zeevaart JR, et al. Combination of terbium-161 with somatostatin receptor antagonists—a potential paradigm shift for the treatment of neuroendocrine neoplasms. Eur J Nucl Med Mol Imaging 2022;49:1113–26. https://doi.org/10.1007/s00259-021-05564-0.

[43] International Commission on Radiation Units and Measurements. Report 85: Fundamental quantities and units for ionizing radiation. J ICRU 2011;11:1–31. https://doi.org/10.1093/jicru/ndr011.

[44] Andreo P. Monte Carlo simulations in radiotherapy dosimetry. Radiation Oncology 2018;13:121. https://doi.org/10.1186/s13014-018-1065-3.

[45] Kellerer AM, Hahn K, Rossi HH. Intermediate dosimetric quantities. Radiat Res 1992;130:15–25.

[46] Kassis AI. Molecular and cellular radiobiological effects of Auger emitting radionuclides. Radiation Protection Dosimetry 2011;143:241–7. https://doi.org/10.1093/rpd/ncq385.

[47] Sgouros G, Roeske JC, McDevitt MR, Palm S, Allen BJ, Fisher DR, et al. MIRD Pamphlet No. 22 (Abridged): Radiobiology and Dosimetry of α-Particle Emitters for Targeted Radionuclide Therapy. Journal of Nuclear Medicine 2010;51:311–28. https://doi.org/10.2967/jnumed.108.058651.

[48] Ziegler JF, Ziegler MD, Biersack JP. SRIM – The stopping and range of ions in matter (2010). Nuclear Instruments and Methods in Physics Research Section B: Beam Interactions with Materials and Atoms 2010;268:1818–23. https://doi.org/10.1016/j.nimb.2010.02.091.

[49] Howell RW, Narra VR, Rao DV, Sastry KSR. Radiobiological Effects of Intracellular ^{210}Po Alpha Emissions: A Comparison with Auger Emitters. Radiation Protection Dosimetry 1990;31:325–8. https://doi.org/10.1093/oxfordjournals.rpd.a080690.

[50] Marcu L, Bezak E, Allen BJ. Global comparison of targeted alpha vs targeted beta therapy for cancer: In vitro, in vivo and clinical trials. Critical Reviews in Oncology/Hematology 2018;123:7–20. https://doi.org/10.1016/j.critrevonc.2018.01.001.

[51] Pouget J-P, Constanzo J. Revisiting the Radiobiology of Targeted Alpha Therapy. Front Med (Lausanne) 2021;8:692436. https://doi.org/10.3389/fmed.2021.692436.

[52] Castillo-Rico LR, Flores-Mancera MA, Massillon-JL G. Stopping power and CSDA range of electrons in liquid water, LiF, CaF_2, and Al_2O_3 from the energy gap up to 433 keV. Nuclear Instruments and Methods in Physics Research Section B: Beam Interactions with Materials and Atoms 2021;502:189–97. https://doi.org/10.1016/j.nimb.2021.07.002.

[53] Berger MJ, Coursey JS, Zucker MA. ESTAR, PSTAR, and ASTAR: Computer Programs for Calculating Stopping-Power and Range Tables for Electrons, Protons, and Helium Ions (version 1.21). NIST 1999.

[54] Hobbs RF, Howell RW, Song H, Baechler S, Sgouros G. Redefining Relative Biological Effectiveness in the Context of the EQDX Formalism: Implications for Alpha-Particle Emitter Therapy. Radiat Res 2014;181:90–8. https://doi.org/10.1667/RR13483.1.

[55] Dale RG, Jones B. The assessment of RBE effects using the concept of biologically effective dose. International Journal of Radiation Oncology*Biology*Physics 1999;43:639–45. https://doi.org/10.1016/S0360-3016(98)00364-2.

[56] Baechler S, Hobbs RF, Prideaux AR, Wahl RL, Sgouros G. Extension of the biological effective dose to the MIRD schema and possible implications in radionuclide therapy dosimetry. Med Phys 2008;35:1123–34.

[57] van Leeuwen CM, Oei AL, Crezee J, Bel A, Franken NAP, Stalpers LJA, et al. The alfa and beta of tumours: a review of parameters of the linear-quadratic model, derived from clinical radiotherapy studies. Radiation Oncology 2018;13:96. https://doi.org/10.1186/s13014-018-1040-z.

[58] McMahon SJ. The linear quadratic model: usage, interpretation and challenges. Phys Med Biol 2018;64:01TR01. https://doi.org/10.1088/1361-6560/aaf26a.

[59] Lawhn-Heath C, Hope TA, Martinez J, Fung EK, Shin J, Seo Y, et al. Dosimetry in radionuclide therapy: the clinical role of measuring radiation dose. The Lancet Oncology 2022;23:e75–87. https://doi.org/10.1016/S1470-2045(21)00657-4.

[60] Pandit-Taskar N, Iravani A, Lee D, Jacene H, Pryma D, Hope T, et al. Dosimetry in Clinical Radiopharmaceutical Therapy of Cancer: Practicality Versus Perfection in Current Practice. Journal of Nuclear Medicine 2021;62:60S-72S. https://doi.org/10.2967/jnumed.121.262977.

[61] Bernhardt P, Svensson J, Hemmingsson J, van der Meulen NP, Zeevaart JR, Konijnenberg MW, et al. Dosimetric Analysis of the Short-Ranged Particle Emitter ^{161}Tb for Radionuclide Therapy of Metastatic Prostate Cancer. Cancers 2021;13:2011. https://doi.org/10.3390/cancers13092011.

[62] Liatsou I, Josefsson A, Yu J, Li Z, Davis K, Brayton C, et al. Early Normal Tissue Effects and Bone Marrow Relative Biological Effectiveness for an Actinium 225-Labeled HER2/neu-Targeting Antibody. International Journal of Radiation Oncology*Biology*Physics 2023;117:1028–37. https://doi.org/10.1016/j.ijrobp.2023.06.003.

[63] Matsakis D, Coster A, Laster B, Sime R. A renaming proposal: “The Auger–Meitner effect.” Physics Today 2019;72:10–1. https://doi.org/10.1063/PT.3.4281.

[64] Filosofov D, Kurakina E, Radchenko V. Potent candidates for Targeted Auger Therapy: Production and radiochemical considerations. Nuclear Medicine and Biology 2021;94–95:1–19. https://doi.org/10.1016/j.nucmedbio.2020.12.001.

[65] Bolcaen J, Gizawy MA, Terry SYA, Paulo A, Cornelissen B, Korde A, et al. Marshalling the Potential of Auger Electron Radiopharmaceutical Therapy. Journal of Nuclear Medicine 2023;64:1344–51. https://doi.org/10.2967/jnumed.122.265039.

[66] Pouget J-P, Santoro L, Raymond L, Chouin N, Bardiès M, Bascoul-Mollevi C, et al. Cell Membrane is a More Sensitive Target than Cytoplasm to Dense Ionization Produced by Auger Electrons. Radiation Research 2008;170:192–200. https://doi.org/10.1667/RR1359.1.

[67] Santoro L, Boutaleb S, Garambois V, Bascoul-Mollevi C, Boudousq V, Kotzki P-O, et al. Noninternalizing Monoclonal Antibodies Are Suitable Candidates for ^{125}I Radioimmunotherapy of Small-Volume Peritoneal Carcinomatosis. Journal of Nuclear Medicine 2009;50:2033–41. https://doi.org/10.2967/jnumed.109.066993.

[68] Shen CJ, Minn I, Hobbs RF, Chen Y, Josefsson A, Brummet M, et al. Auger radiopharmaceutical therapy targeting prostate-specific membrane antigen in a micrometastatic model of prostate cancer. Theranostics 2020;10:2888–96. https://doi.org/10.7150/thno.38882.

[69] Kassis AI, Sastry KSR, Adelstein SJ. Kinetics of Uptake, Retention, and Radiotoxicity of ^{125}IUdR in Mammalian Cells: Implications of Localized Energy Deposition by Auger Processes. Radiation Research 1987;109:78–89. https://doi.org/10.2307/3576869.

[70] Pirovano G, Jannetti SA, Carter LM, Sadique A, Kossatz S, Guru N, et al. Targeted Brain Tumor Radiotherapy Using an Auger Emitter. Clinical Cancer Research 2020;26:2871–81. https://doi.org/10.1158/1078-0432.CCR-19-2440.

[71] Macapinlac HA, Kemeny N, Daghighian F, Finn R, Zhang J, Humm J, et al. Pilot clinical trial of 5-[^{125}I]iodo-2'-deoxyuridine in the treatment of colorectal cancer metastatic to the liver. J Nucl Med 1996;37:25S-29S.

[72] Riad A, Gitto SB, Lee H, Winters HD, Martorano PM, Hsieh C-J, et al. PARP Theranostic Auger Emitters Are Cytotoxic in BRCA Mutant Ovarian Cancer and Viable Tumors from Ovarian Cancer Patients Enable Ex-Vivo Screening of Tumor Response. Molecules 2020;25:6029. https://doi.org/10.3390/molecules25246029.

[73] Akudugu JM, Neti PVSV, Howell RW. Changes in Lognormal Shape Parameter Guide Design of Patient-Specific Radiochemotherapy Cocktails. Journal of Nuclear Medicine 2011;52:642–9. https://doi.org/10.2967/jnumed.110.083584.

[74] Kassis AI, Adelstein SJ. Radiobiologic Principles in Radionuclide Therapy. Journal of Nuclear Medicine 2005;46:4S-12S.

[75] Hubbell JH, Seltzer SM. Tables of x-ray mass attenuation coefficients and mass energy-absorption coefficients 1 keV to 20 meV for elements z = 1 to 92 and 48 additional substances of dosimetric interest. National Inst. of Standards and Technology - PL, Gaithersburg, MD (United States). Ionizing Radiation Div.; 1995.

[76] Peter Bernhardt EF-A Lars Jacobsson, Gunnar Skarnemark. Low-energy Electron Emitters for Targeted Radiotherapy of Small Tumours. Acta Oncologica 2001;40:602–8. https://doi.org/10.1080/028418601750444141.

[77] Uusijärvi H, Bernhardt P, Ericsson T, Forssell-Aronsson E. Dosimetric characterization of radionuclides for systemic tumor therapy: influence of particle range, photon emission, and subcellular distribution. Med Phys 2006;33:3260–9. https://doi.org/10.1118/1.2229428.

[78] Katugampola S, Wang J, Rosen A, Howell RW. MIRD Pamphlet No. 27: MIRDcell V3, a Revised Software Tool for Multicellular Dosimetry and Bioeffect Modeling. Journal of Nuclear Medicine 2022;63:1441–9. https://doi.org/10.2967/jnumed.121.263253.

[79] Solanki JH, Tritt T, Pasternack JB, Kim JJ, Leung CN, Domogauer JD, et al. Cellular Response to Exponentially Increasing and Decreasing Dose Rates: Implications for Treatment Planning in Targeted Radionuclide Therapy. Rare 2017;188:221–34. https://doi.org/10.1667/RR14766.1.

[80] Allison J, Amako K, Apostolakis J, Arce P, Asai M, Aso T, et al. Recent developments in Geant4. Nuclear Instruments and Methods in Physics Research Section A: Accelerators, Spectrometers, Detectors and Associated Equipment 2016;835:186–225. https://doi.org/10.1016/j.nima.2016.06.125.

[81] Champion C, Zanotti-Fregonara P, Hindié E. CELLDOSE: A Monte Carlo Code to Assess Electron Dose Distribution—S Values for ^{131}I in Spheres of Various Sizes. Journal of Nuclear Medicine 2008;49:151–7. https://doi.org/10.2967/jnumed.107.045179.

[82] Ftá_niková S, Böhm R. Monte Carlo Calculations of Energy Deposition on Cellular, Multicellular and Organ Level for Auger Emitters. Radiation Protection Dosimetry 2000;92:279–88. https://doi.org/10.1093/oxfordjournals.rpd.a033293.

[83] Eckerman K, Endo A. ICRP Publication 107. Nuclear decay data for dosimetric calculations. Ann ICRP 2008;38:7–96. https://doi.org/10.1016/j.icrp.2008.10.004.

[84] Barrett KE, Houson HA, Lin W, Lapi SE, Engle JW. Production, Purification, and Applications of a Potential Theranostic Pair: Cobalt-55 and Cobalt-58m. Diagnostics 2021;11:1235. https://doi.org/10.3390/diagnostics11071235.

[85] Valdovinos H, Hernandez R, Goel S, Graves S, Barnhart T, Cai W, et al. Cyclotron production of ^{58m}Co for Auger electron-based targeted radioimmunotherapy and PET imaging post-therapy with the daughter ^{58g}Co. J Nucl Med 2016;57:332–332.

[86] Thisgaard H, Olsen BB, Dam JH, Bollen P, Mollenhauer J, Høilund-Carlsen PF. Evaluation of Cobalt-Labeled Octreotide Analogs for Molecular Imaging and Auger Electron–Based Radionuclide Therapy. Journal of Nuclear Medicine 2014;55:1311–6. https://doi.org/10.2967/jnumed.114.137182.

[87] Thisgaard H, Olesen ML, Dam JH. Radiosynthesis of ^{55}Co- and ^{58m}Co-labelled DOTATOC for positron emission tomography imaging and targeted radionuclide therapy: Radiosynthesis of ^{55}Co- and ^{58m}Co-labelled DOTATOC. J Label Compd Radiopharm 2011;54:758–62. https://doi.org/10.1002/jlcr.1919.

[88] Baun C, Dam JH, Hildebrandt MG, Ewald JD, Kristensen BW, Gammelsrød VS, et al. Preclinical evaluation of [^{58m}Co]Co-DOTA-PSMA-617 for Auger electron therapy of prostate cancer. Sci Rep 2023;13:18837. https://doi.org/10.1038/s41598-023-43429-8.

[89] Sargeson AM. The potential for the cage complexes in biology. Coordination Chemistry Reviews 1996;151:89–114. https://doi.org/10.1016/S0010-8545(96)90197-6.

[90] Houson HA, Tekin V, Lin W, Aluicio-Sarduy E, Engle JW, Lapi SE. PET Imaging of the Neurotensin Targeting Peptide NOTA-NT-20.3 Using Cobalt-55, Copper-64 and Gallium-68. Pharmaceutics 2022;14:2724. https://doi.org/10.3390/pharmaceutics14122724.

[91] Garousi J, Andersson KG, Dam JH, Olsen BB, Mitran B, Orlova A, et al. The use of radiocobalt as a label improves imaging of EGFR using DOTA-conjugated Affibody molecule. Scientific Reports 2017;7:5961. https://doi.org/10.1038/s41598-017-05700-7.

[92] Valdovinos HF, Hernandez R, Graves S, Ellison PA, Barnhart TE, Theuer CP, et al. Cyclotron production and radiochemical separation of ^{55}Co and ^{58m}Co from ^{54}Fe, ^{58}Ni and ^{57}Fe targets. Applied Radiation and Isotopes 2017;130:90–101. https://doi.org/10.1016/j.apradiso.2017.09.005.

[93] Mastren T, Marquez BV, Sultan DE, Bollinger E, Eisenbeis P, Voller T, et al. Cyclotron Production of High–Specific Activity ^{55}Co and In Vivo Evaluation of the Stability of ^{55}Co Metal-Chelate-Peptide Complexes. Mol Imaging 2015;14:7290.2015.00025. https://doi.org/10.2310/7290.2015.00025.

[94] Thisgaard H, Elema D r., Jensen M. Production and dosimetric aspects of the potent Auger emitter ^{58m}Co for targeted radionuclide therapy of small tumors. Medical Physics 2011;38:4535–41. https://doi.org/10.1118/1.3608905.

[95] Kinsey RR, Dunford CL, Tuli JK, Burrows TW. The NUDAT/PCNUDAT program for nuclear data. Hungary: Springer; 1997.

[96] Otuka N, Takács S. Definitions of radioisotope thick target yields. Radiochimica Acta 2015;103:1–6. https://doi.org/10.1515/ract-2013-2234.

[97] Koning AJ, Rochman D, Sublet J-Ch, Dzysiuk N, Fleming M, van der Marck S. TENDL: Complete Nuclear Data Library for Innovative Nuclear Science and

Technology. Nuclear Data Sheets 2019;155:1–55. https://doi.org/10.1016/j.nds.2019.01.002.

[98] IAEA Safety Standards Classification of Radioactive Waste. IAEA; 2009.

[99] Strelow FWE, Van Zyl CR, Bothma CJC. Distribution coefficients and the cation-exchange behaviour of elements in hydrochloric acid-ethanol mixtures. Analytica Chimica Acta 1969;45:81–92. https://doi.org/10.1016/S0003-2670(00)89389-7.

[100] Strelow FWE, Victor AH, Van Zyl CR, Eloff Cynthia. Distribution coefficients and cation exchange behavior of elements in hydrochloric acid-acetone. Anal Chem 1971;43:870–6. https://doi.org/10.1021/ac60302a015.

[101] Strelow FWE, Weinert CHSW, Eloff Cynthia. Distribution coefficients and anion exchange behavior of elements in oxalic acid-hydrochloric acid mixtures. Anal Chem 1972;44:2352–6. https://doi.org/10.1021/ac60322a001.

[102] Sudár S, Qaim SM. Isomeric cross-section ratio for the formation of $^{58}Co^{m,g}$ in neutron, proton, deuteron, and alpha-particle induced reactions in the energy region up to 25 MeV. Phys Rev C 1996;53:2885–92. https://doi.org/10.1103/PhysRevC.53.2885.

[103] Valdovinos HF, Hernandez R, Goel S, Graves S, Barnhart T, Cai W, et al. Auger electron-based targeted radioimmunotherapy with 58mCo, a feasibility study. AIP Conference Proceedings 2016;1747:080006. https://doi.org/10.1063/1.4954126.

[104] Del Monte U. Does the cell number 10^9 still really fit one gram of tumor tissue? Cell Cycle 2009;8:505–6. https://doi.org/10.4161/cc.8.3.7608.

[105] Geue RJ, Hambley TW, Harrowfield JM, Sargeson AM, Snow MR. Metal ion encapsulation: cobalt cages derived from polyamines, formaldehyde, and nitromethane. J Am Chem Soc 1984;106:5478–88. https://doi.org/10.1021/ja00331a016.

[106] Bottomley GA, Clark IJ, Creaser II, Engelhardt LM, Geue RJ, Hagen KS, et al. The Synthesis and Structure of Encapsulating Ligands: Properties of Bicyclic Hexamines. Aust J Chem 1994;47:143–79. https://doi.org/10.1071/ch9940143.

[107] Bigham NP, Wilson JJ. Investigation of Cobalt(III) Cage Complexes as Inhibitors of the Mitochondrial Calcium Uniporter. European Journal of Inorganic Chemistry 2023;26:e202200735. https://doi.org/10.1002/ejic.202200735.

[108] Cooper MS, Ma MT, Sunassee K, Shaw KP, Williams JD, Paul RL, et al. Comparison of ^{64}Cu-Complexing Bifunctional Chelators for Radioimmunoconjugation: Labeling Efficiency, Specific Activity, and in Vitro/in Vivo Stability. Bioconjugate Chem 2012;23:1029–39. https://doi.org/10.1021/bc300037w.

[109] S. Donnelly P. The role of coordination chemistry in the development of copper and rhenium radiopharmaceuticals. Dalton Transactions 2011;40:999–1010. https://doi.org/10.1039/C0DT01075H.

[110] Comba P, Sickmüller AF. Modeling of the Redox Properties of (Hexaamine)cobalt(III/II) Couples. Inorg Chem 1997;36:4500–7. https://doi.org/10.1021/ic9701625.

[111] Wieghardt K, Bossek U, Chaudhuri P, Herrmann W, Menke BC, Weiss J. 1,4,7-Triazacyclononane-N,N',N''-triacetate (TCTA), a new hexadentate ligand for divalent and trivalent metal ions. Crystal structures of [CrIII(TCTA)], [FeIII(TCTA)],

and Na[CuII(TCTA)].bul.2NaBr.bul.8H2O. Inorg Chem 1982;21:4308–14. https://doi.org/10.1021/ic00142a037.

[112] Yu M, Xie D, Phan KP, Enriquez JS, Luci JJ, Que EL. A Co^{II} complex for ^{19}F MRI-based detection of reactive oxygen species. Chem Commun 2016;52:13885–8. https://doi.org/10.1039/C6CC08207F.

[113] Mitran B, Thisgaard H, Rinne S, Dam JH, Azami F, Tolmachev V, et al. Selection of an optimal macrocyclic chelator improves the imaging of prostate cancer using cobalt-labeled GRPR antagonist RM26. Sci Rep 2019;9:17086. https://doi.org/10.1038/s41598-019-52914-y.

[114] Radford LL, Fernandez S, Beacham R, El Sayed R, Farkas R, Benešová M, et al. New ^{55}Co-labeled Albumin-Binding Folate Derivatives as Potential PET Agents for Folate Receptor Imaging. Pharmaceuticals 2019;12:166. https://doi.org/10.3390/ph12040166.

[115] Alshoukr F, Rosant C, Maes V, Abdelhak J, Raguin O, Burg S, et al. Novel Neurotensin Analogues for Radioisotope Targeting to Neurotensin Receptor-Positive Tumors. Bioconjugate Chem 2009;20:1602–10. https://doi.org/10.1021/bc900151z.

[116] Falciani C, Fabbrini M, Pini A, Lozzi L, Lelli B, Pileri S, et al. Synthesis and biological activity of stable branched neurotensin peptides for tumor targeting. Mol Cancer Ther 2007;6:2441–8. https://doi.org/10.1158/1535-7163.MCT-07-0164.

[117] Morinville A, Martin S, Lavallée M, Vincent J-P, Beaudet A, Mazella J. Internalization and trafficking of neurotensin via NTS3 receptors in HT29 cells. The International Journal of Biochemistry & Cell Biology 2004;36:2153–68. https://doi.org/10.1016/j.biocel.2004.04.013.

[118] Wu zherui, Martinez-Fong D, Trédaniel J, Forgez P. Neurotensin and its high affinity receptor 1 as a potential pharmacological target in cancer therapy. Frontiers in Endocrinology 2013;3.

[119] Bergmann R, Scheunemann M, Heichert C, Mäding P, Wittrisch H, Kretzschmar M, et al. Biodistribution and catabolism of ^{18}F-labeled neurotensin(8–13) analogs. Nuclear Medicine and Biology 2002;29:61–72. https://doi.org/10.1016/S0969-8051(01)00284-0.

[120] Janssen PJJM, Visser M de, Verwijnen SM, Bernard BF, Srinivasan A, Erion JL, et al. Five Stabilized ^{111}In-Labeled Neurotensin Analogs in Nude Mice Bearing HT29 Tumors. Https://HomeLiebertpubCom/Cbr 2009. https://doi.org/10.1089/cbr.2007.369.A.

[121] Previti S, Vivancos M, Rémond E, Beaulieu S, Longpré J-M, Ballet S, et al. Insightful Backbone Modifications Preventing Proteolytic Degradation of Neurotensin Analogs Improve NTS1-Induced Protective Hypothermia. Frontiers in Chemistry 2020;8.

[122] Schindler L, Moosbauer J, Schmidt D, Spruss T, Grätz L, Lüdeke S, et al. Development of a Neurotensin-Derived ^{68}Ga-Labeled PET Ligand with High In Vivo Stability for Imaging of NTS1 Receptor-Expressing Tumors. Cancers 2022;14:4922. https://doi.org/10.3390/cancers14194922.

[123] Geer S. Evaluation of the neurotensin receptor-1 as target for molecular imaging and radiotherapy of pancreatic and prostate cancer. Friedrich-Alexander-Universität Erlangen-Nürnberg (FAU), 2018.

[124] Schulz J, Rohracker M, Stiebler M, Goldschmidt J, Stöber F, Noriega M, et al. Proof of Therapeutic Efficacy of a ^{177}Lu-Labeled Neurotensin Receptor 1 Antagonist in a Colon Carcinoma Xenograft Model. Journal of Nuclear Medicine 2017;58:936–41. https://doi.org/10.2967/jnumed.116.185140.

[125] Baum RP, Singh A, Schuchardt C, Kulkarni HR, Klette I, Wiessalla S, et al. ^{177}Lu-3BP-227 for Neurotensin Receptor 1–Targeted Therapy of Metastatic Pancreatic Adenocarcinoma: First Clinical Results. Journal of Nuclear Medicine 2018;59:809–14. https://doi.org/10.2967/jnumed.117.193847.

[126] Fritz J. Non-aqueous solvents in anion-exchange separations. Talanta 1961;8:143–62. https://doi.org/10.1016/0039-9140(61)80049-0.

[127] Kraus K, Nelson F. Metal Separations by Anion Exchange. Symposium on Ion Exchange and Chromatography in Analytical Chemistry, ASTM International; 1958, p. 27–57. https://doi.org/10.1520/STP44180S.

[128] Strelow FWE. Distribution coefficients and ion exchange behavior of 46 elements with a macroreticular cation exchange resin in hydrochloric acid. Anal Chem 1984;56:1053–6. https://doi.org/10.1021/ac00270a045.

[129] Avila-Rodriguez MA, Nye JA, Nickles RJ. Simultaneous production of high specific activity ^{64}Cu and ^{61}Co with 11.4MeV protons on enriched ^{64}Ni nuclei. Applied Radiation and Isotopes 2007;65:1115–20. https://doi.org/10.1016/j.apradiso.2007.05.012.

[130] Graves SA, Hernandez R, Fonslet J, England CG, Valdovinos HF, Ellison PA, et al. Novel Preparation Methods of ^{52}Mn for ImmunoPET Imaging. Bioconjugate Chem 2015;26:2118–24. https://doi.org/10.1021/acs.bioconjchem.5b00414.

[131] Lin W, Wilkinson JT, Barrett KE, Barnhart TE, Gott M, Becker KV, et al. Excitation function of ^{54}Fe(p,α)^{51}Mn from 9.5 MeV to 18 MeV. Nuclear Physics A 2022;1021:122424. https://doi.org/10.1016/j.nuclphysa.2022.122424.

[132] Lin W, Aluicio-Sarduy E, Houson HA, Barnhart TE, Tekin V, Jeffery JJ, et al. Theranostic cobalt-55/58m for neurotensin receptor-mediated radiotherapy in vivo: A pilot study with dosimetry. Nuclear Medicine and Biology 2023;118–119:108329. https://doi.org/10.1016/j.nucmedbio.2023.108329.

[133] Schild M, Gundlach-Graham A, Menon A, Jevtic J, Pikelja V, Tanner M, et al. Replacing the Argon ICP: Nitrogen Microwave Inductively Coupled Atmospheric-Pressure Plasma (MICAP) for Mass Spectrometry. Anal Chem 2018;90:13443–50. https://doi.org/10.1021/acs.analchem.8b03251.

[134] Pourmand A, Dauphas N. Distribution coefficients of 60 elements on TODGA resin: Application to Ca, Lu, Hf, U and Th isotope geochemistry. Talanta 2010;81:741–53. https://doi.org/10.1016/j.talanta.2010.01.008.

[135] Horwitz EP, McAlister DR, Bond AH, Barrans RE. Novel Extraction of Chromatographic Resins Based on Tetraalkyldiglycolamides: Characterization and Potential Applications. Solvent Extraction and Ion Exchange 2005;23:319–44. https://doi.org/10.1081/SEI-200049898.

[136] Mirzayev N, Pavlova Marinova A, Marinov Marinov G, Mammadov K, Karandashev V, Rakhimov A, et al. Distribution Coefficients of 60 Elements on Cation and Anion-Exchange Resin in Ammonium Chloride Solutions. Solvent Extraction and Ion Exchange 2019;37:473–87. https://doi.org/10.1080/07366299.2019.1679458.

[137] Dam JH, Olsen BB, Baun C, Høilund-Carlsen PF, Thisgaard H. A PSMA Ligand Labeled with Cobalt-55 for PET Imaging of Prostate Cancer. Mol Imaging Biol 2017;19:915–22. https://doi.org/10.1007/s11307-017-1121-7.

[138] Taneja JN. Dissolution of iron in hydrochloric acid. 1967.

[139] M. Paterson B, Roselt P, Denoyer D, Cullinane C, Binns D, Noonan W, et al. PET imaging of tumours with a ^{64}Cu labeled macrobicyclic cage amine ligand tethered to Tyr 3 -octreotate. Dalton Transactions 2014;43:1386–96. https://doi.org/10.1039/C3DT52647J.

[140] Cullinane C, Jeffery CM, Roselt PD, Dam EM van, Jackson S, Kuan K, et al. Peptide Receptor Radionuclide Therapy with ^{67}Cu-CuSarTATE Is Highly Efficacious Against a Somatostatin-Positive Neuroendocrine Tumor Model. Journal of Nuclear Medicine 2020;61:1800–5. https://doi.org/10.2967/jnumed.120.243543.

[141] Kelly JM, Ponnala S, Amor-Coarasa A, Zia NA, Nikolopoulou A, Williams CJr, et al. Preclinical Evaluation of a High-Affinity Sarcophagine-Containing PSMA Ligand for ^{64}Cu/^{67}Cu-Based Theranostics in Prostate Cancer. Mol Pharmaceutics 2020;17:1954–62. https://doi.org/10.1021/acs.molpharmaceut.0c00060.

[142] Huynh TT, van Dam EM, Sreekumar S, Mpoy C, Blyth BJ, Muntz F, et al. Copper-67-Labeled Bombesin Peptide for Targeted Radionuclide Therapy of Prostate Cancer. Pharmaceuticals 2022;15:728. https://doi.org/10.3390/ph15060728.

[143] Dearling JLJ, van Dam EM, Harris MJ, Packard AB. Detection and therapy of neuroblastoma minimal residual disease using [^{64}/^{67}Cu]Cu-SARTATE in a preclinical model of hepatic metastases. EJNMMI Research 2021;11:20. https://doi.org/10.1186/s13550-021-00763-0.

[144] Cabrera GOF, Ma X, Lin W, Zhang T, Zhao W, Pan L, et al. Synthesis of ^{64}Cu-, ^{55}Co-, and ^{68}Ga-Labeled Radiopharmaceuticals Targeting Neurotensin Receptor-1 for Theranostics: Adjusting In Vivo Distribution Using Multiamine Macrocycles. Journal of Nuclear Medicine 2024. https://doi.org/10.2967/jnumed.124.267469.

[145] Bond AM, Lawrance GA, Lay PA, Sargeson AM. Electrochemistry of macrobicyclic (hexaamine)cobalt(III) complexes. 1. Metal-centered and substituent reductions. Inorg Chem 1983;22:2010–21. https://doi.org/10.1021/ic00156a017.

[146] Donnelly PS, Harrowfield JM, Skelton BW, White AH. Carboxymethylation of Cage Amines: Control of Alkylation by Metal Ion Coordination. Inorg Chem 2000;39:5817–30. https://doi.org/10.1021/ic000346a.

[147] Cai H, Fissekis J, Conti PS. Synthesis of a novel bifunctional chelator AmBaSar based on sarcophagine for peptide conjugation and ^{64}Cu radiolabelling. Dalton Trans 2009:5395–400. https://doi.org/10.1039/B902210D.

[148] Bartolo NMD, Sargeson AM, Donlevy TM, Smith SV. Synthesis of a new cage ligand, SarAr, and its complexation with selected transition metal ions for potential use in radioimaging. J Chem Soc, Dalton Trans 2001:2303–9. https://doi.org/10.1039/B103242A.

[149] Behm CA, Boreham PFL, Creaser II, Korybutdaszkiewicz B, Maddalena DJ, Sargeson AM, et al. Novel Cationic Surfactants Derived From Metal Ion Cage Complexes: Potential Antiparasitic Agents. Aust J Chem 1995;48:1009–30. https://doi.org/10.1071/ch9951009.

[150] Gully D, Labeeuw B, Boigegrain R, Oury-Donat F, Bachy A, Poncelet M, et al. Biochemical and Pharmacological Activities of SR 142948A, a New Potent Neurotensin Receptor Antagonist. J Pharmacol Exp Ther 1997;280:802–12.

[151] Gundlich B, Musmann P, Weber S, Nix O, Semmler W. From 2D PET to 3D PET: Issues of Data Representation and Image Reconstruction. Zeitschrift Für Medizinische Physik 2006;16:31–46. https://doi.org/10.1078/0939-3889-00290.

[152] Bashkin JK, Bass LA, Sondhi SM, Robinson KD, Beatty AM. Hydrogenation of dinitrosarcophagine Co(III); the crystal structures of Co(II) and Co(III) complexes of diaminosarcophagine. Inorganica Chimica Acta 1996;253:91–5. https://doi.org/10.1016/S0020-1693(96)05112-2.

[153] Helm L, Merbach AE. Water exchange on metal ions: experiments and simulations. Coordination Chemistry Reviews 1999;187:151–81. https://doi.org/10.1016/S0010-8545(99)90232-1.

[154] Bajpayee AG, Grodzinsky AJ. Cartilage-targeting drug delivery: can electrostatic interactions help? Nat Rev Rheumatol 2017;13:183–93. https://doi.org/10.1038/nrrheum.2016.210.

[155] Vedadghavami A, Zhang C, Bajpayee AG. Overcoming negatively charged tissue barriers: Drug delivery using cationic peptides and proteins. Nano Today 2020;34:100898. https://doi.org/10.1016/j.nantod.2020.100898.

[156] Dorazio SJ, Olatunde AO, Tsitovich PB, Morrow JR. Comparison of divalent transition metal ion paraCEST MRI contrast agents. J Biol Inorg Chem 2014;19:191–205. https://doi.org/10.1007/s00775-013-1059-4.

[157] Yu M, Bouley BS, Xie D, Enriquez JS, Que EL. ^{19}F PARASHIFT Probes for Magnetic Resonance Detection of H_2O_2 and Peroxidase Activity. J Am Chem Soc 2018;140:10546–52. https://doi.org/10.1021/jacs.8b05685.

[158] Buglyó P, Kacsir I, Kozsup M, Nagy I, Nagy S, Bényei AC, et al. Tuning the redox potentials of ternary cobalt(III) complexes containing various hydroxamates. Inorganica Chimica Acta 2018;472:234–42. https://doi.org/10.1016/j.ica.2017.07.026.

[159] Bernhardt PV, Chen K-I, Sharpe PC. Transition metal complexes as mediator-titrants in protein redox potentiometry. J Biol Inorg Chem 2006;11:930–6. https://doi.org/10.1007/s00775-006-0148-z.

[160] Ogino H, Ogino K. Redox potentials and related parameters of cobalt(III/II) complexes containing aminopolycarboxylates. Inorg Chem 1983;22:2208–11. https://doi.org/10.1021/ic00157a023.

[161] Joyner JC, Cowan JA. Targeted Cleavage of HIV RRE RNA by Rev-Coupled Transition Metal Chelates. J Am Chem Soc 2011;133:9912–22. https://doi.org/10.1021/ja203057z.

[162] Rinne SS, Dahlsson Leitao C, Saleh-nihad Z, Mitran B, Tolmachev V, Ståhl S, et al. Benefit of Later-Time-Point PET Imaging of HER3 Expression Using Optimized Radiocobalt-Labeled Affibody Molecules. Int J Mol Sci 2020;21:1972. https://doi.org/10.3390/ijms21061972.

[163] Rosestedt M, Andersson KG, Mitran B, Rinne SS, Tolmachev V, Löfblom J, et al. Evaluation of a radiocobalt-labelled affibody molecule for imaging of human epidermal growth factor receptor 3 expression. International Journal of Oncology 2017;51:1765–74. https://doi.org/10.3892/ijo.2017.4152.

[164] Lawrance GA, Lay PA, Sargeson AM. Organic substituent effects in macrobicyclic (hexaamine)cobalt(III/II) complexes: a new method of obtaining polar substituent constants. Inorg Chem 1990;29:4808–16. https://doi.org/10.1021/ic00348a042.

[165] Sargeson AM, Lay PA. Dependence of the Properties of Cobalt(III) Cage Complex as a Function of the Derivatization of Amine Substituents. Aust J Chem 2009;62:1280. https://doi.org/10.1071/CH09368.

[166] Uudsemaa M, Tamm T. Density-Functional Theory Calculations of Aqueous Redox Potentials of Fourth-Period Transition Metals. J Phys Chem A 2003;107:9997–10003. https://doi.org/10.1021/jp0362741.

[167] Hendry P, Ludi A. Structure, Reactivity, Spectra, and Redox Properties of Cobalt(III) Hexaamines. In: Sykes AG, editor. Advances in Inorganic Chemistry, vol. 35, Academic Press; 1990, p. 117–98. https://doi.org/10.1016/S0898-8838(08)60162-2.

[168] Bard AJ. Standard Potentials in Aqueous Solution. New York: Routledge; 2017. https://doi.org/10.1201/9780203738764.

[169] Heppeler A, André JP, Buschmann I, Wang X, Reubi J-C, Hennig M, et al. Metal-Ion-Dependent Biological Properties of a Chelator-Derived Somatostatin Analogue for Tumour Targeting. Chemistry – A European Journal 2008;14:3026–34. https://doi.org/10.1002/chem.200701264.

[170] Golub G, Cohen H, Meyerstein D. The stabilization of monovalent copper ions by complexation with saturated tertiary amine ligands in aqueous solutions. The case of 2,5,9,12-tetramethyl-2,5,9,12-tetraazatridecane. J Chem Soc, Chem Commun 1992:397. https://doi.org/10.1039/c39920000397.

[171] Bertini I, Messori L, Golub G, Cohen H, Meyerstein D. A ^{1}H NMR study of the complex of cobalt(II) with 2,5,8,11-tetramethyl-2,5,8,11-tetraazadodecane in aerated aqueous solutions. Inorganica Chimica Acta 1995;235:5–8. https://doi.org/10.1016/0020-1693(95)90038-8.

[172] Abozeid SM, Snyder EM, Tittiris TY, Steuerwald CM, Nazarenko AY, Morrow JR. Inner-Sphere and Outer-Sphere Water Interactions in Co(II) paraCEST Agents. Inorg Chem 2018;57:2085–95. https://doi.org/10.1021/acs.inorgchem.7b02977.

[173] Toy-Miou-Leong M, Bachelet C-M, Pélaprat D, Rostène W, Forgez P. NT Agonist Regulates Expression of Nuclear High-affinity Neurotensin Receptors. J Histochem Cytochem 2004;52:335–45. https://doi.org/10.1177/002215540405200304.

[174] Maschauer S, Einsiedel J, Hübner H, Gmeiner P, Prante O. ^{18} F- and ^{68} Ga-Labeled Neurotensin Peptides for PET Imaging of Neurotensin Receptor 1. J Med Chem 2016;59:6480–92. https://doi.org/10.1021/acs.jmedchem.6b00675.

[175] Schindler L, Bernhardt G, Keller M. Modifications at Arg and Ile Give Neurotensin(8–13) Derivatives with High Stability and Retained NTS1 Receptor Affinity. ACS Med Chem Lett 2019;10:960–5. https://doi.org/10.1021/acsmedchemlett.9b00122.

[176] Lang C, Maschauer S, Hübner H, Gmeiner P, Prante O. Synthesis and Evaluation of a ^{18}F-Labeled Diarylpyrazole Glycoconjugate for the Imaging of NTS1-Positive Tumors. J Med Chem 2013;56:9361–5. https://doi.org/10.1021/jm401491e.

[177] Vaziri B, Wu H, Dhawan AP, Du P, Howell RW, Committee I collaboration with the SM. MIRD Pamphlet No. 25: MIRDcell V2.0 Software Tool for Dosimetric Analysis

of Biologic Response of Multicellular Populations. Journal of Nuclear Medicine 2014;55:1557–64. https://doi.org/10.2967/jnumed.113.131037.

[178] Sebastian JA, Moore MJ, Berndl ESL, Kolios MC. An image-based flow cytometric approach to the assessment of the nucleus-to-cytoplasm ratio. PLoS One 2021;16:e0253439. https://doi.org/10.1371/journal.pone.0253439.

[179] International Commission on Radiological Protection S (UK). Radionuclide transformations - energy and intensity of emissions. United Kingdom: Pergamon; 1983.

[180] Tomayko MM, Reynolds CP. Determination of subcutaneous tumor size in athymic (nude) mice. Cancer Chemother Pharmacol 1989;24:148–54. https://doi.org/10.1007/BF00300234.

[181] Bolch WE, Eckerman KF, Sgouros G, Thomas SR. MIRD Pamphlet No. 21: A Generalized Schema for Radiopharmaceutical Dosimetry—Standardization of Nomenclature. Journal of Nuclear Medicine 2009;50:477–84. https://doi.org/10.2967/jnumed.108.056036.

[182] Stabin MG, Wendt RE, Flux GD. RADAR Guide: Standard Methods for Calculating Radiation Doses for Radiopharmaceuticals, Part 1—Collection of Data for Radiopharmaceutical Dosimetry. J Nucl Med 2022;63:316–22. https://doi.org/10.2967/jnumed.120.259200.

[183] Kostou T, Papadimitroulas P, Loudos G, Kagadis GC. A preclinical simulated dataset of S-values and investigation of the impact of rescaled organ masses using the MOBY phantom. Phys Med Biol 2016;61:2333. https://doi.org/10.1088/0031-9155/61/6/2333.

[184] Agostinelli S, Allison J, Amako K, Apostolakis J, Araujo H, Arce P, et al. Geant4—a simulation toolkit. Nuclear Instruments and Methods in Physics Research Section A: Accelerators, Spectrometers, Detectors and Associated Equipment 2003;506:250–303. https://doi.org/10.1016/S0168-9002(03)01368-8.

[185] Allison J, Amako K, Apostolakis J, Araujo H, Arce Dubois P, Asai M, et al. Geant4 developments and applications. IEEE Transactions on Nuclear Science 2006;53:270–8. https://doi.org/10.1109/TNS.2006.869826.

[186] Keller M, Mahuroof SA, Hong Yee V, Carpenter J, Schindler L, Littmann T, et al. Fluorescence Labeling of Neurotensin(8–13) via Arginine Residues Gives Molecular Tools with High Receptor Affinity. ACS Med Chem Lett 2020;11:16–22. https://doi.org/10.1021/acsmedchemlett.9b00462.

[187] Vandenbulcke F, Nouel D, Vincent JP, Mazella J, Beaudet A. Ligand-induced internalization of neurotensin in transfected COS-7 cells: differential intracellular trafficking of ligand and receptor. Journal of Cell Science 2000;113:2963–75. https://doi.org/10.1242/jcs.113.17.2963.

[188] Roettger BF, Ghanekar D, Rao R, Toledo C, Yingling J, Pinon D, et al. Antagonist-Stimulated Internalization of the G Protein-Coupled Cholecystokinin Receptor. Mol Pharmacol 1997;51:357–62.

[189] Ferguson SSG. Evolving Concepts in G Protein-Coupled Receptor Endocytosis: The Role in Receptor Desensitization and Signaling. Pharmacol Rev 2001;53:1–24.

[190] Cui X-Y, Li Z, Kong Z, Liu Y, Meng H, Wen Z, et al. Covalent targeted radioligands potentiate radionuclide therapy. Nature 2024;630:206–13. https://doi.org/10.1038/s41586-024-07461-6.

[191] dos Santos JC, Schäfer M, Bauder-Wüst U, Beijer B, Eder M, Leotta K, et al. Refined Chelator Spacer Moieties Ameliorate the Pharmacokinetics of PSMA-617. Front Chem 2022;10:898692. https://doi.org/10.3389/fchem.2022.898692.

[192] Lin W, Aluicio-Sarduy E, Barrett KE, Barnhart TE, Mixdorf JC, DeLuca MC, et al. Separation of cyclotron-produced cobalt-55/58m from iron targets using cation exchange chromatography with non-aqueous solvents and extraction chromatography. Applied Radiation and Isotopes 2023;200:110980. https://doi.org/10.1016/j.apradiso.2023.110980.

[193] Lin W, Fonseca Cabrera GO, Aluicio-Sarduy E, Barnhart TE, Mixdorf JC, Li Z, et al. Radiolabeling Diaminosarcophagine with Cyclotron-Produced Cobalt-55 and [^{55}Co]Co-NT-Sarcage as a Proof of Concept in a Murine Xenograft Model. Bioconjugate Chem 2024. https://doi.org/10.1021/acs.bioconjchem.4c00043.

[194] Braad PEN, Hansen SB, Thisgaard H, Høilund-Carlsen PF. PET imaging with the non-pure positron emitters: ^{55}Co, ^{86}Y and ^{124}I. Phys Med Biol 2015;60:3479–97. https://doi.org/10.1088/0031-9155/60/9/3479.

[195] Dam JH, Olsen BB, Baun C, Høilund-Carlsen P-F, Thisgaard H. In Vivo Evaluation of a Bombesin Analogue Labeled with Ga-68 and Co-55/57. Mol Imaging Biol 2016;18:368–76. https://doi.org/10.1007/s11307-015-0911-z.

[196] Andersen TL, Baun C, Olsen BB, Dam JH, Thisgaard H. Improving Contrast and Detectability: Imaging with [^{55}Co]Co-DOTATATE in Comparison with [^{64}Cu]Cu-DOTATATE and [^{68}Ga]Ga-DOTATATE. Journal of Nuclear Medicine 2020;61:228–33. https://doi.org/10.2967/jnumed.119.233015.

[197] Baun C, Mitran B, Rinne SS, Dam JH, Olsen BB, Tolmachev V, et al. Preclinical Evaluation of the Copper-64 Labeled GRPR-Antagonist RM26 in Comparison with the Cobalt-55 Labeled Counterpart for PET-Imaging of Prostate Cancer. Molecules 2020;25:5993. https://doi.org/10.3390/molecules25245993.

[198] Worrall R, Colling B, Gilbert MR, Litherland-Smith E, Nobs CR, Packer LW, et al. The development, testing and comparison of unfolding methods in SPECTRA-UF for neutron spectrometry. Fusion Engineering and Design 2020;161:112038. https://doi.org/10.1016/j.fusengdes.2020.112038.

[199] McElroy WN, Berg S, Gigas G. Neutron-Flux Spectral Determination by Foil Activation. Nuclear Science and Engineering 1967;27:533–41. https://doi.org/10.13182/NSE86-A17618.

[200] Reginatto M, Goldhagen P. MAXED, a computer code for the deconvolution of multisphere neutron spectrometer data using the maximum entropy method. Dept. of Energy, Environmental Measurements Lab., New York, NY (United States); 1998. https://doi.org/10.2172/663223.

[201] Mosby MA, Engle JW, Jackman KR, Nortier FM, Birnbaum ER. Determination of spallation neutron flux through spectral adjustment techniques. Nuclear Instruments and Methods in Physics Research Section B: Beam Interactions with Materials and Atoms 2016;381:29–33. https://doi.org/10.1016/j.nimb.2016.04.041.

[202] Engle JW, James MR, Mashnik SG, Kelsey CT, Wolfsberg LE, Reass DA, et al. MCNPX characterization of the secondary neutron flux at the Los Alamos Isotope

Production Facility. Nuclear Instruments and Methods in Physics Research Section A: Accelerators, Spectrometers, Detectors and Associated Equipment 2014;754:71–82. https://doi.org/10.1016/j.nima.2014.03.049.

[203] Tai Y-K, Millburn GP, Kaplan SN, Moyer BJ. Neutron Yields from Thick Targets Bombarded by 18- and 32-Mev Protons. Phys Rev 1958;109:2086–91. https://doi.org/10.1103/PhysRev.109.2086.

[204] Bakhtiari M, Mokhtari Oranj L, Jung N-S, Lee A, Lee H-S. Estimation of neutron production yields from $H_2{}^{18}O$ as the ^{18}F-production target bombarded by 18-MeV protons. Radiation Physics and Chemistry 2020;177:109120. https://doi.org/10.1016/j.radphyschem.2020.109120.

[205] Gear JI, Cox MG, Gustafsson J, Gleisner KS, Murray I, Glatting G, et al. EANM practical guidance on uncertainty analysis for molecular radiotherapy absorbed dose calculations. Eur J Nucl Med Mol Imaging 2018;45:2456–74. https://doi.org/10.1007/s00259-018-4136-7.

Appendix A. Nuclear cross section calculations

The rate of production of a radionuclide from particles with charge Ze incident on some target material (including decay, assuming no parent) can be described as:

$$\frac{dN}{dt} = \int_{E_{min}}^{E_{max}} dE \left(-\frac{1}{\rho}\frac{dE}{dx}\right)^{-1} \sigma(E)\frac{I(E,t)}{Ze} - \lambda N \tag{A.1}$$

Where N is the number of radionuclides, ρ is the density of the target, -dE/dx is the stopping power, σ is the cross section, I is the beam current and λ is the decay constant of the radionuclide. Then, if the target is thin enough with thickness x_0 such that the beam current and incident particle energy E_0 are not perturbed substantially as it traverses through the target, equation (A.1) can be simplified to:

$$\frac{dN}{dt} \overset{thin\ target}{\approx} \rho x_0 \sigma(E_0)\frac{I(E_0,t)}{Ze} - \lambda N \tag{A.2}$$

And solved as:

$$N(t) = \rho x_0 \sigma(E_0)\left(e^{-\lambda\tau} * \frac{I(E_0,\tau)}{Ze}\right)\Bigg|_t \tag{A.3}$$

Where * denotes the convolution operator. For a total irradiation duration of T_{EOB}, equation (A.3) can be rearranged to solve for $\sigma(E_0)$:

$$\sigma(E_0) = \frac{N(T_{EOB})}{\rho x_0 \left(e^{-\lambda\tau} * \frac{I(E_0,\tau)}{Ze}\right)\Big|_{T_{EOB}}} \tag{A.4}$$

Then, $N(T_{EOB})$ can be calculated by performing HPGe gamma spectrometry on the irradiated sample according to:

$$N(T_{EOB}) = \frac{n(E)}{t_{real}}\frac{t_{real}}{t_{live}}\frac{t_{real}}{\eta(E) I_\gamma(E)(1 - e^{-\lambda t_{real}})e^{-\lambda T_{elapsed}}} \tag{A.5}$$

Where n is the background subtracted number of counts detected by HPGe for a given ROI, t_{real} is the real time during counting, t_{live} is the live time during counting, η is the calibration efficiency for the HPGe detector, I_γ is the branching ratio of the gamma emission and $T_{elapsed}$ is the time elapsed since EOB at the start of counting.

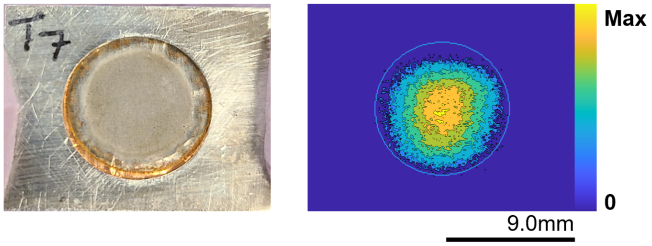

Appendix Figure A-1 An irradiated ^{54}Fe target electrodeposited on Cu substrate (both ~10 μm thick) for evaluating the cross section of ^{54}Fe(p,α)^{51}Mn (left). The sample was autoradiographed to ascertain the beam profile (right).

Appendix B. Neutron spectrum unfolding

The following is a brief discussion on neutron spectrum unfolding with focus on the maximum entropy method and the reader is advised to consult the references for more information.

In contrast to charged particle beams, the rate of radionuclide production for neutrons can be described as:

$$\frac{dN}{dt} = \int_{E_{min}}^{E_{max}} dE \ m_N \phi(E,t) \sigma(E) \ - \lambda N \tag{B.1}$$

Where φ refers to the differential neutron flux, m_N is the number of target atoms for a particular reaction pathway, and all other parameters have the same definition as previously. It is generally difficult to measure φ directly due to a variety of constraints associated with the irradiation facility, but φ computed from simulations can be corrected by using non-discriminating detectors/activation foils [198,199]. These procedures are referred to as "spectrum unfolding" (e.g., "unfolding" the integral to extract information about φ). The following outlines an instance of spectrum unfolding that adopts the maximum entropy method (φ is discretized for numerical methods) [200]:

$$S = -\Sigma_j [\ \phi_j \ ln\left(\frac{\phi_j}{\phi_j^{Initial}}\right) + \phi_j^{Initial} \ - \phi_j] \tag{B.2}$$

S refers to the cross entropy between $\varphi^{initial}$ obtained from simulations and some guess solution φ that is determined after applying the following constraints:

$$\frac{N_i}{m_i} + \epsilon_i = \Sigma_j \ \phi_j \sigma_{i,j} \Delta E_j, \qquad \Sigma_i \left(\frac{\epsilon_i}{\delta_i}\right)^2 = \Omega \tag{B.3}$$

Where i and j refer to different reactions and energies, respectively, ϵ is the deviation from calculated value, *ΔE* is the energy spacing, δ is the uncertainty and Ω is the χ^2 statistic (~degrees of freedom). This optimization problem can be solved using Lagrange multipliers to obtain:

$$\phi_j = \phi_j^{Initial} e^{-\Sigma_i \kappa_i \sigma_{i,j}} \tag{B.4}$$

For some κ that maximizes:

$$Z = -\Sigma_j \left[\phi_j^{Initial} e^{-\Sigma_i \kappa_i \sigma_{i,j}}\right] - \ \Omega \Sigma_i (\kappa_i \sigma_{i,j})^2 - \ \Sigma_i p_i \kappa_i \tag{B.5}$$

Where p=N/m for simplicity. Results from a homemade program in Python is shown in Appendix Figure B-1 below, where data were taken from [201,202] and TENDL.

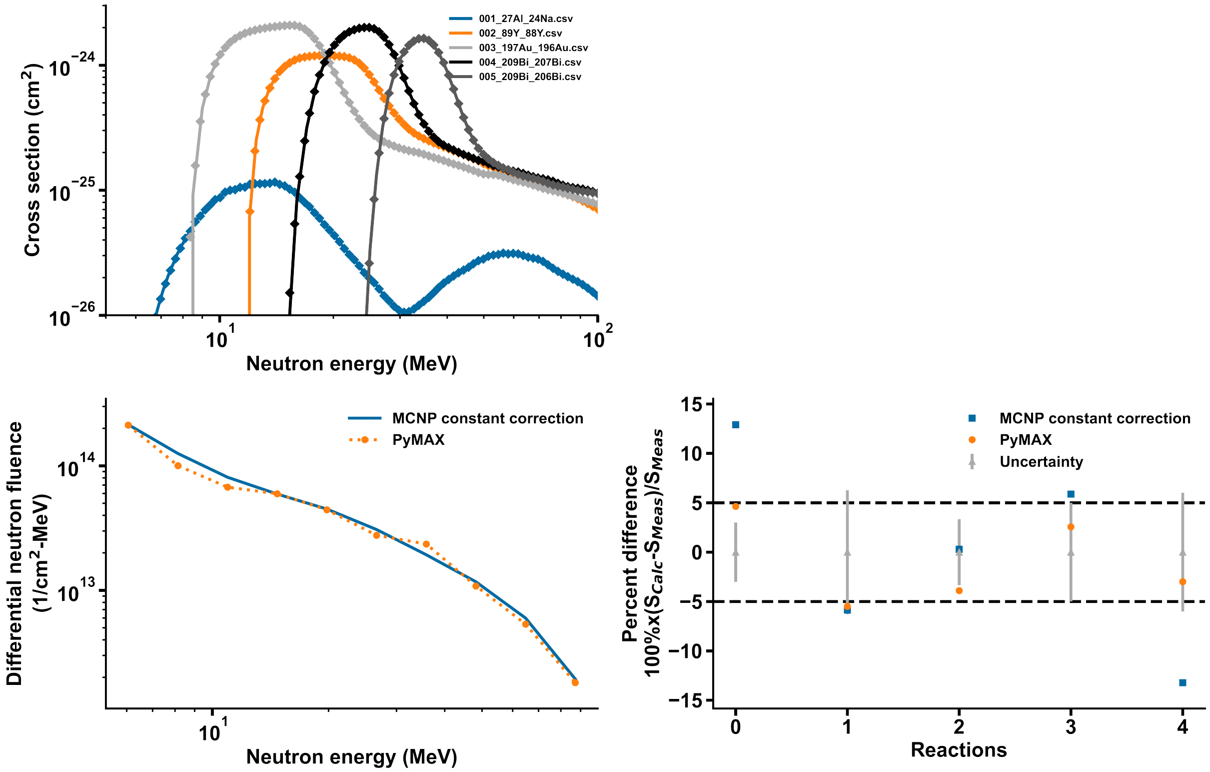

Appendix Figure B-1 Sample figures from adapted neutron spectrum unfolding program in Python showing the cross sections used for the correction (top left), the neutron fluence (bottom left) and the percent difference between measured and calculated activities (bottom right). Source code will be made available on Github.

Appendix C. Concrete shielding simulations

For a given floor plan, neutron and photon dose to personnel were simulated for 200 μA 30 MeV protons incident on thick liquid [^{18}O]H_2O and solid Be targets. The results are shown in Appendix Figure C-1.

Simulated neutron flux for Be and [^{18}O]H_2O corroborate with [203] and [204], respectively. Geant4 simulations used the AllHP physics package with no thermal scattering law, and MCNP6.x simulations validated results from Geant4. The importance sampling factor in Geant4 was approximately 1.5 and 2 per 10 cm of Portland cement concrete for photons and neutrons, respectively. Geant4 flux-to-dose conversion was performed via ANSI/ANS-6.1.1-1977 and photons/neutrons were simulated separately for 30 MeV protons on thick [^{18}O]H_2O (North) or Be (South) then post-processed. Neutrons <5 MeV were discarded, and phase space were binned in 5-10, 10-20 and 20-30 MeV groups. Since generated photons were isotropic, no such processing was performed, and no photons were discarded. Geant4 derived particle flux was calculated from counts/area for simplicity given the geometry.

Explicitly, MCNP simulations used default N, P and H physics, the built-in dose conversion via ANSI/ANS-6.1.1-1977 and applied thermal scattering law for H and Si in concrete. Importance sampling parameters were generated automatically using built-in window generator(s).

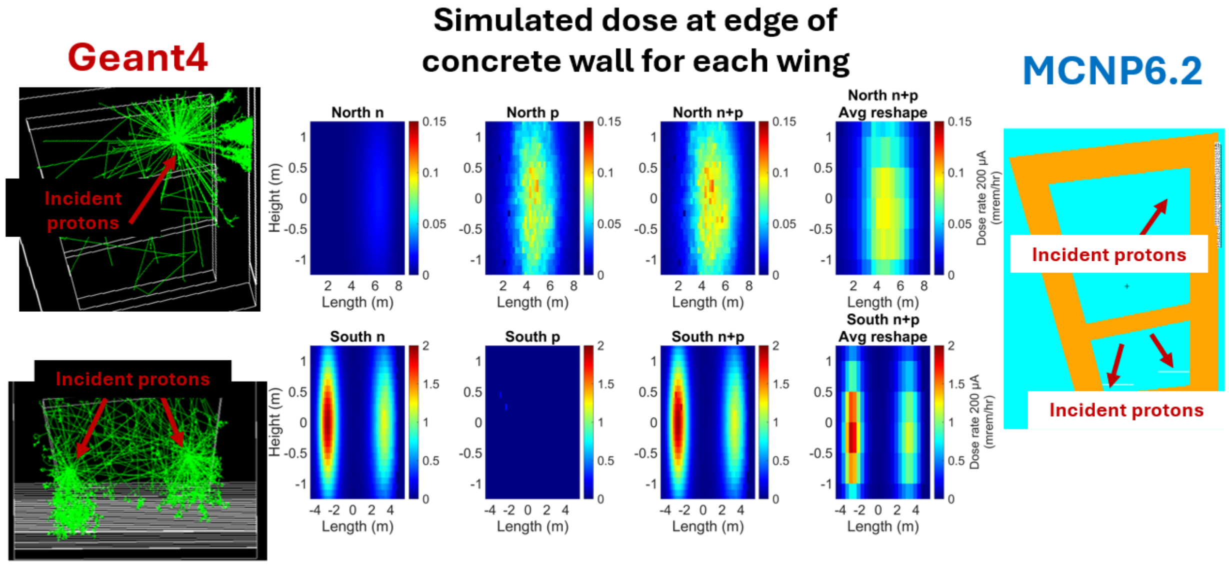

Appendix Figure C-1 Sample floor plan geometry simulated in Geant4 (left) and MCNP (right) and the resulting neutron/photon dose estimates (middle). Geant4 simulated dose agreed with MCNP.

Appendix D. Miscellaneous supporting figures

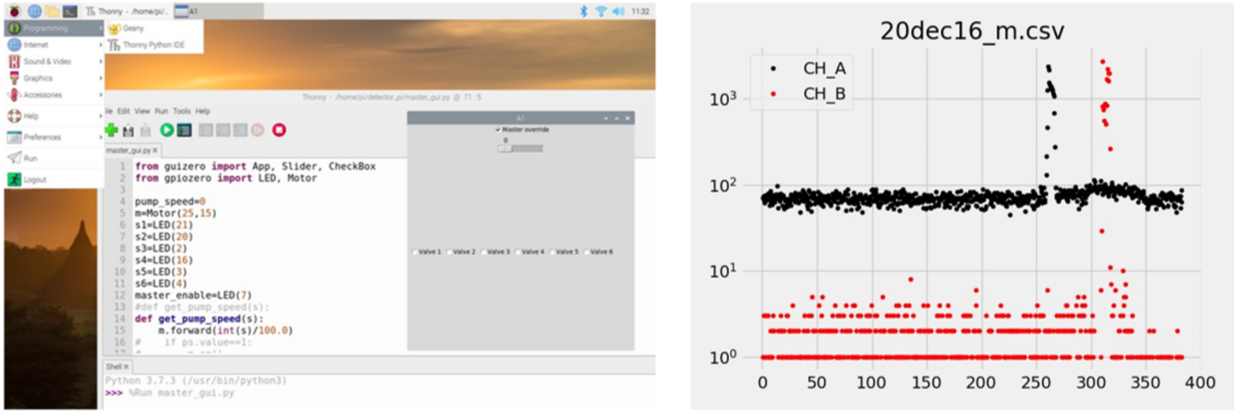

```python
from guizero import App, Slider, CheckBox
from gpiozero import LED, Motor

pump_speed=0
m=Motor(25,15)
s1=LED(21)
s2=LED(20)
s3=LED(2)
s4=LED(16)
s5=LED(3)
s6=LED(4)
master_enable=LED(7)
#def get_pump_speed(s):
def get_pump_speed(s):
    m.forward(int(s)/100.0)
#    if ps.value==1:
```

```
Python 3.7.3 (/usr/bin/python3)
>>> %Run master_gui.py
```

Appendix Figure D-1 Raspberry Pi control interface (left) for the semi-automated chemistry module. Live plotting can be performed in parallel (right).

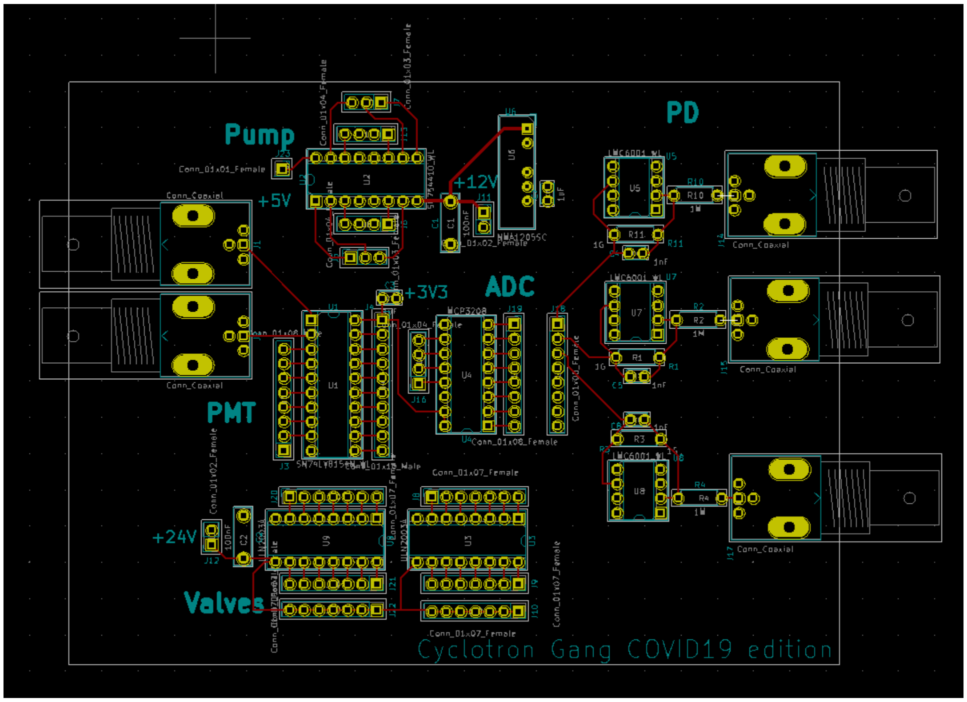

Appendix Figure D-2 External PCB coupled to the Raspberry Pi for miscellaneous tasks such as controlling the valves and motor(s), detecting voltage signals from photodiodes and/or counting pulses from photomultiplier tube(s).

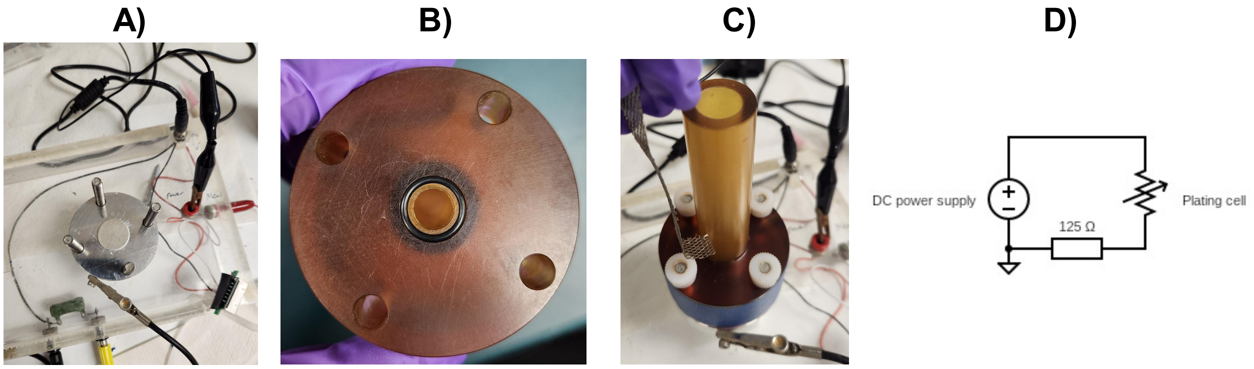

Appendix Figure D-3 Electroplating setup. A) silver disk cathode on the aluminum base, B) the acid-resistant plating piece with a Viton™ O ring seal on the bottom (9 mm plating diameter), C) platinum-coated titanium mesh anode and D) the relevant circuit diagram.

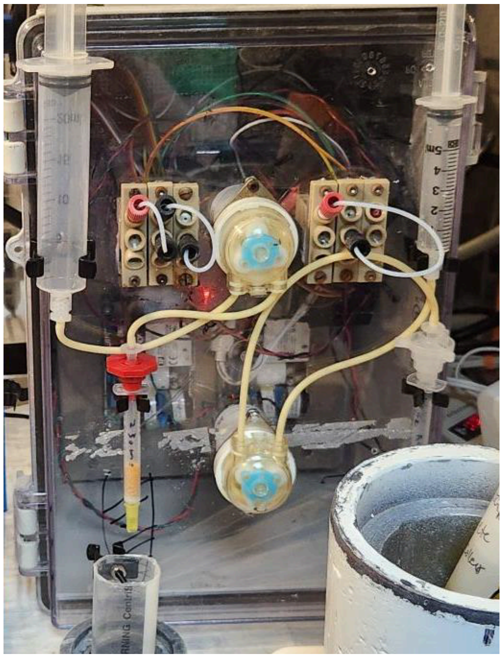

Appendix Figure D-4 The most recent radiochemistry module used for separations (with two pumps!). The AG® 50W-X8 and branched-DGA column are on the left and right side of the box, respectively. No valves were attached to this iteration of the module, but the Raspberry Pi can control 6 valves.

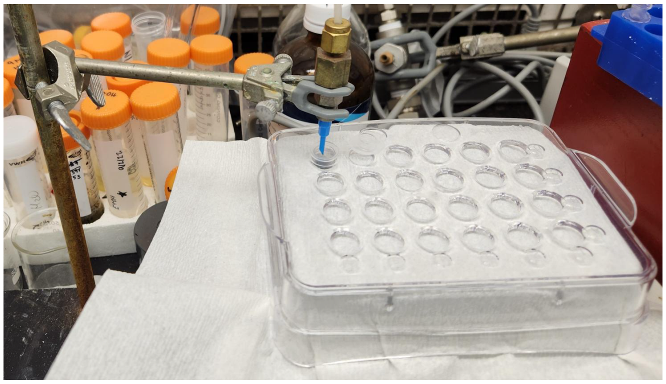

Appendix Figure D-5 The setup used for drying down the eluted fraction under argon flow and heat.

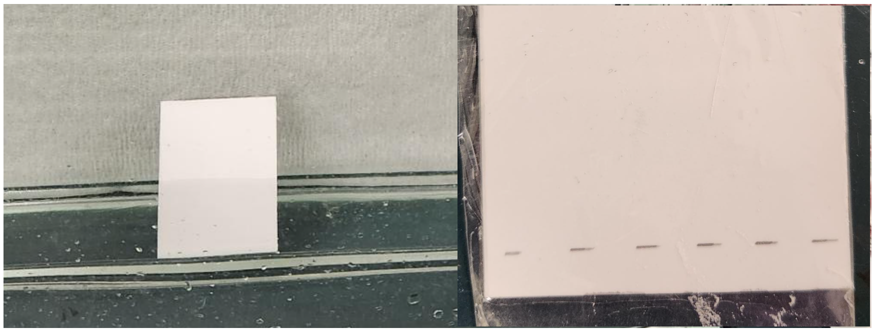

Appendix Figure D-6 The setup used for developing the radio-TLC plates (left). The radio-TLC plate is removed from the solution once the solvent front reaches a certain height (typically $\gtrsim$5 cm, depending on the retention factor of the sample), dried, then sealed with tape to prevent contamination when analyzing the sample (right).

Appendix Figure D-7 To analyze the developed radio-TLC plate, a radio-sensitive phosphor plate is exposed to the sealed radio-TLC plate (left), mounted on the holder (middle) then placed in the cyclone's insert (right) for analysis.

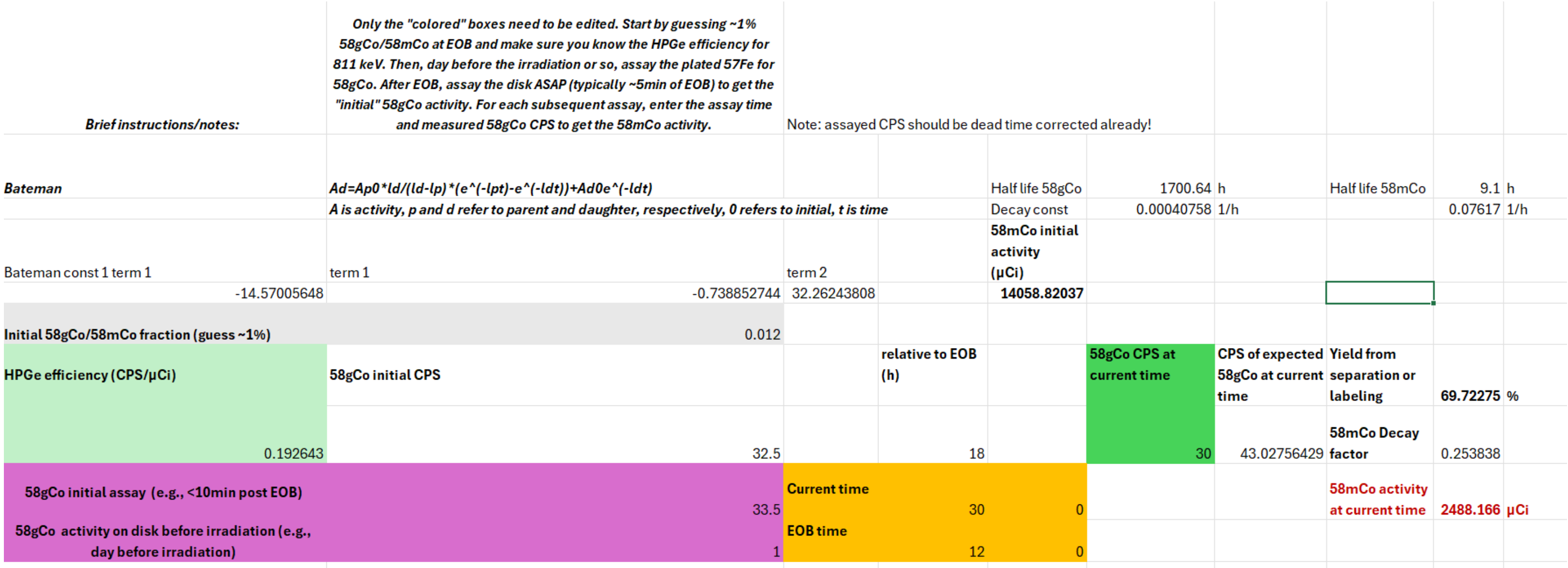

Brief instructions/notes:	*Only the "colored" boxes need to be edited. Start by guessing ~1% 58gCo/58mCo at EOB and make sure you know the HPGe efficiency for 811 keV. Then, day before the irradiation or so, assay the plated 57Fe for 58gCo. After EOB, assay the disk ASAP (typically ~5min of EOB) to get the "initial" 58gCo activity. For each subsequent assay, enter the assay time and measured 58gCo CPS to get the 58mCo activity.*	Note: assayed CPS should be dead time corrected already!							
Bateman	*Ad=Ap0*ld/(ld-lp)*(e^(-lpt)-e^(-ldt))+Ad0e^(-ldt)*			Half life 58gCo	1700.64	h	Half life 58mCo	9.1	h
	A is activity, p and d refer to parent and daughter, respectively, 0 refers to initial, t is time			Decay const	0.00040758	1/h		0.07617	1/h
Bateman const 1 term 1	term 1	term 2		**58mCo initial activity (µCi)**					
-14.57005648	-0.738852744	32.26243808		**14058.82037**					
Initial 58gCo/58mCo fraction (guess ~1%)	0.012								
HPGe efficiency (CPS/µCi)	**58gCo initial CPS**		**relative to EOB (h)**		**58gCo CPS at current time**	**CPS of expected 58gCo at current time**	**Yield from separation or labeling**	**69.72275**	%
0.192643	32.5		18		30	43.02756429	**58mCo Decay factor**	0.253838	
58gCo initial assay (e.g., <10min post EOB)	33.5	**Current time**	30	0			**58mCo activity at current time**	**2488.166**	**µCi**
58gCo activity on disk before irradiation (e.g., day before irradiation)	1	**EOB time**	12	0					

Appendix Figure D-8 Excel spreadsheet to estimate the real-time ^{58m}Co activity.

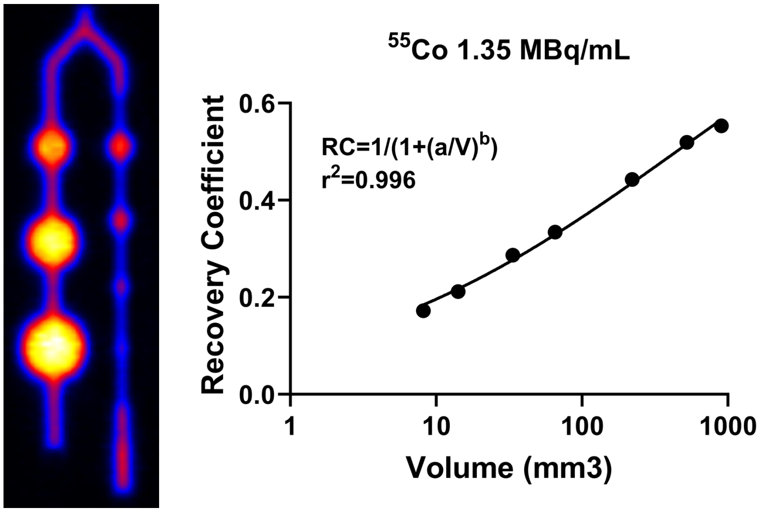

Appendix Figure D-9 Recovery coefficients for ^{55}Co obtained by adding 1.35 MBq/mL [^{55}Co]Co-NOTA in aqueous media at pH7.4 into Phantech's PVC27-GrIT phantom (left) and fit using a two-parameter logistic function [205] (right).